Measurement of the Top Quark Mass in the Muon+Jets Final State at $\sqrt{s} = 13$ TeV

Thesis in the study programme Master of Science Physik
Universität Hamburg

Christoph Garbers

Hamburg, October 11, 2016

1. Gutachter: Prof. Dr. Peter Schleper
2. Gutachter: Prof. Dr. Johannes Haller

Abstract

In this thesis the mass of the top quark is measured using a sample of $t\bar{t}$ candidate events with a muon and at least four jets in the final state, collected by CMS in pp collisions at $\sqrt{s} = 13$ TeV at the LHC. The candidate events are selected from data corresponding to an integrated luminosity of 2.2 fb^{-}1. For each event the mass of the top quark candidates is reconstructed from a kinematic fit on the decay products to a $t\bar{t}$ hypothesis. The top quark mass is determined simultaneously with a jet energy scale factor, estimated from the invariant mass of the W boson candidate. This results in a top quark mass of $m_t = 172.34 \pm 0.37$ (stat+JSF) ± 1.02 (syst) GeV.

Kurzfassung

In dieser Masterarbeit wird die Masse des Topquarks aus Ereignissen mit $t\bar{t}$ Kandidaten bestimmt, die in ein Muon und mindestens vier Jets zerfallen. Die Ereignisse wurden aus einem Datensatz mit einer integrierten Luminosität von 2.2 fb^{-1}, der am CMS Detektor aus pp-Kollision bei $\sqrt{s} = 13$ TeV im LHC, aufgenommen wurde, ausgewählt. Die Masse der Topquarks wird aus einem kinemtaischen Fit der Zerfallsprodukte rekonstruiert. Gleichzeitig zur Masse wird der Jetenergieskalierungsfaktor aus der W Bosonmassenverteilung gemessen. Die Messung ergibt eine Topquarkmasse von $m_t = 172.34$ ± 0.37 (stat+JSF) ± 1.02 (syst) GeV.

Contents

1 Introduction

In its run at a center-of-mass energy of $\sqrt{s} = 8\,\text{TeV}$ the Large Hadron Collider delivered a luminosity of about $20\,\text{fb}^{-1}$ of pp-collision data, greatly improving the understanding of physics in the high energy regime. The CMS collaboration alone published 560 papers since the start of the LHC in 2008.
While the top quark was discovered at the Tevatron, the LHC produces top quarks in a quantity, that it is rightfully called a "top quark factory". A luminosity of $2.2\,\text{fb}^{-1}$ was recorded at $\sqrt{s} = 13\,\text{TeV}$ between May and December 2015, about 1 830 000 top quark pairs are expected. At the same time new versions of the `Powheg` event generator and `Pythia` showering tool, promise a better theoretical description of the data with simulation.
The mass of top quark is one of the most precise measured quantities of the standard model of particle physics. At the same time, its exact value in global theory fits could rule out or strengthen different theory models.
In this thesis, top quark pairs that decay into one muon plus jets are selected and the mass of the top quark is determined. Here the data at $\sqrt{s} = 13\,\text{TeV}$ is used for the first time for a top mass analysis, performing a measurement statistically independent of previous determinations.
While the sample size is still lower than in the Run 1 analyses with $20\,\text{fb}^{-1}$ at $\sqrt{s} = 8\,\text{TeV}$, it is expected that the measurement is limited by systematic uncertainties and not by statistical.
The measurement will be done with a hybrid approach that combines the in-situ measurement of the jet scale factor with the jet calibration from γ/Z+jet measurements. The measurements themselves are done with a template fit method.
The method used is similar to the $\sqrt{s} = 8\,\text{TeV}$ lepton+jets analysis that yielded the most precise single measurement of the top quark mass up today. Therefore, even if not the same precision will be achieved, this analysis is a good benchmark to compare the performance of this method with the new data and simulations to the former ones.

1.1 Unit convention

In this thesis two different unit systems will be use. Macroscopic apertures will be described in SI units. Properties of elemental particles or structures of the same order of magnitude will be described in "natural" units, where the reduced Planck constant $\hbar = \frac{h}{2\pi}$, the speed of light c, and the Boltzmann constant k_B are set to 1. This results in the unit eV for masses, energy and momenta and the unit eV^{-1} for length and time. For example a mass of $1\,\mathrm{eV}$ equals in SI units $1.78 \times 10^{-36}\,\mathrm{kg}$ and a length of $1\,\mathrm{eV}^{-1}$ equals $1.97 \times 10^{-7}\,\mathrm{m}$. Also the elemental charge, which is the absolute of the charge of an electron, in SI units $\mathrm{e} = 1.602176565 \cdot 10^{-19}\,\mathrm{C}$, is used.

2 Introducing the top quark

2.1 The Standard Model of particle physics

The core of physics is the study of matter and its movement through space and time. To not only describe but predict its behavior, various theories of the composition of matter and on the basic principles have been developed.

In modern physics, all behavior of matter is described by four fundamental forces, gravitation, electromagnetic interaction, weak nuclear force, and strong nuclear force. While gravitation is the easiest to observe it is on small scales by far the weakest. Macroscopic gravitation is excellently described by Einsteins theory of general relativity, backed by the recently discovered gravitational waves [1], but it is not well described on the microscopic level we are looking at in high energy particle physics.

The basic model that describes the electromagnetic, the weak and the strong force and the composition of matter is called the standard model of particle physics (SM). In the following a short overview of the content of the standard model is given. A more mathematical approach will be given in section 2.1.1. All fundamental particles in the SM are assumed to be point-like and for every charged particle there is an anti-particle with the same attributes but opposite charge. The particles can be categorized as fermions with spin $\frac{1}{2}$ and bosons with integer spin. The light fermions, except the neutrinos, basically build the solid matter, while the bosons mediate the fundamental forces between them. All SM particle are categorized and labeled with their mass, charge and spin in figure 2.1.

For more details on the properties of the Standard Modell of particle physics refer to reference [2].

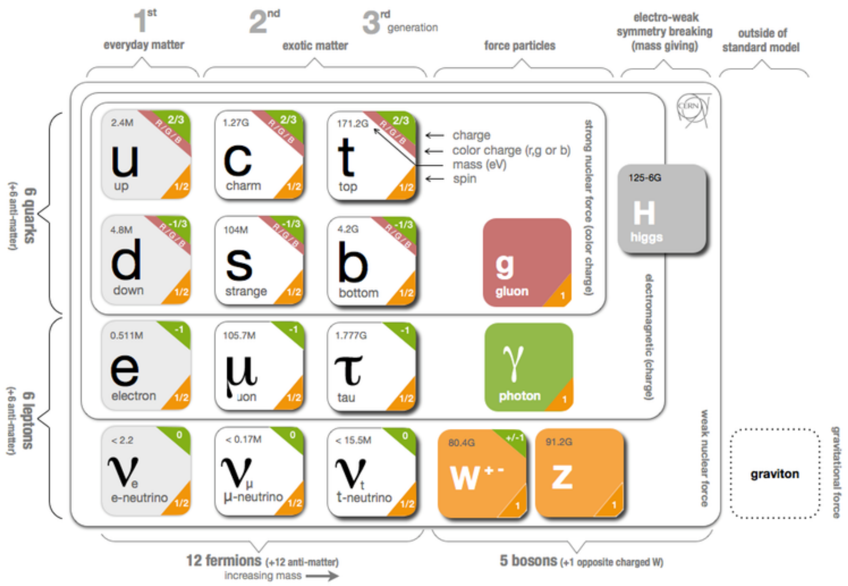

Figure 2.1: Overview of all particles of the standard model of particle physics. [3]

Fermions The fermions of the standard model are divided into six quarks that can interact through all forces and six leptons that do not interact through the strong force. Each of these groups is divided into three generations, that are pairs of the fermions that are most likely to interact which each other.

Each generation contains two quarks, one has an electric charge of $+\frac{2}{3}\,\mathrm{e}$ and the other $-\frac{1}{3}\,\mathrm{e}$. Both carry color charge. In each generation of two leptons, one has an electric charge of $-1\,\mathrm{e}$. The other one is a neutrino. Neutrinos carry no charge and have originally be considered massless, although mass limits and quadratic mass differences of the neutrinos are known and important for neutrino oscillations [4]. Neutrinos can only interact via the weak force.

Bosons In the standard model all bosons have a spin of one, except the higgs boson with a spin of 0. The higgs boson can interact with all particles that have a mass. Its own mass was found to be $m_H = 125.4\,\mathrm{GeV}$ [5]. It couples dominantly with the top quark. This makes the understanding of the top quark important for the Higgs boson and vice versa. The higgs field and its mechanism is responsible for the masses of three other bosons, the Z and the $\mathrm{W}^{\pm}$, and will be described in section 2.1.3.

The Z and $W^{\pm}$ bosons are the mediators of the weak force and couple to all SM fermions. The weak force acts only over small distances which is related to the masses of its bosons. The $W^{\pm}$ boson has a electric charge of ±1 while the Z boson has none. Because of their coupling to all fermions, the properties of this two bosons are excellent to check other parts of the SM. For example measurements of Z boson cross section confirmed the number of neutrino generations to be three [6]. For the purposes of this thesis the $W^{\pm}$ boson is important. In the SM the particle flavor cannot change via a neutral current, as mediated by a Z boson. Therefore, top quark decays are likely to be mediated by $W^{\pm}$ bosons (more details on this will follow in section 2.2). For simplicity the $W^{\pm}$ bosons will be labeled as W bosons in the following.
The boson that mediates the electromagnetic force is the photon. It couples on all particles with electric charge. It has no mass or charge and therefor the reach of the electromagnetic field is unlimited.
The last boson, the mediator of the strong force, is the gluon. It is massless like the photon but carries color and anti-color charge. Its reach is the smallest of all SM forces. This will be explained in more detail in section 2.1.2.

While the standard model is by no means a "theory of everything" it is well suited for all physics phenomena that have been observed in particle colliders so far.

2.1.1 Gauge Theory

Mathematically the Standard Model is formulated as a Quantum Field Theory. Its formulation can be found by the quantization of fields derived by Gauge theories. A Gauge theory is based on the principle that conservation laws are associated with the invariance of a system under a specific symmetry transformation. These symmetry transformations are described in the group theory framework by Lie groups. One important Lie group is the Lorentz group, known for the theory of special relativity.
If the Lagrangian density $\mathscr{L} = \mathscr{T} - \mathscr{V}$, with the kinetic energy density $\mathscr{T}$ and the potential energy density $\mathscr{V}$, of a particle field ψ is known, its classical dynamics are given by the Euler-Lagrange equation

$$\partial_\mu \left(\frac{\partial \mathscr{L}}{\partial \left(\partial_\mu \psi \right)} \right) - \frac{\partial \mathscr{L}}{\partial \psi} = 0 \,.$$

The Lagrangian density for free particles in a scalar field contains a kinematic term in the order of $\partial^\mu \psi \partial_\mu \psi$ and a mass term in the order of $m^2 \psi^2$. Further interactions can be included into the theory by adding terms on the order of ψ^3 or ψ^4 provided with coupling constants.

2.1.2 Quantum Chromodynamics

The Quantum Chromodynamics (QCD), another name of the interaction due to the strong force, describes the interaction of chromatic charged particles. The underlying group is the $SU(3)_C$, fundamentally represented by the eight 3×3 Gell-Mann matrices. The three chromatic charges are typically denoted as "red", "green", and "blue". Gluons interact because of their own charge with other gluons. This leads to an effective QCD coupling constant α_s that is large for low and small for high energies. Therefore the potential energy between separated quarks becomes large and new quark-antiquark pairs are created until all quarks are part of color neutral mesons and baryons.

2.1.3 Quantum Electrodynamics

Quantum Electrodynamics (QED) ties together the weak and the electromagnetic force into a $SU(2)_L \times U(1)_Y$ gauge group. Initially it has four massless vector boson gauge fields and one complex scalar field, the Higgs field. The Higgs field has a potential of $V_H = \mu^2 \psi^\dagger \psi - \lambda (\psi^\dagger \psi)^2$ with a ground state at 246 GeV, called vacuum expectation value. The symmetry of the Higgs field is broken spontaneously. Therefore, in the effective low-energy case mass-like terms for three of the four vector bosons, that are the $\mathrm{W}^\pm$ and Z, are provided. Its additional scalar term brings in a new massive particle, the Higgs boson.

2.2 The top quark

The top quark is an up-type quark of the third generation with a charge of $+\frac{2}{3}$e. It was predicted together with the bottom quark in 1973 by Makoto Kobayashi and Toshihide Maskawa to explain the CP-violation of the kaon decay. It was discovered in 1995 by the CDF and DØ experiments at Fermilab with a mass of $m_{\mathrm{t}} = 176 \pm 18\,\mathrm{GeV}$ [7–9]. It is still the heaviest elementary particle that is observed. Because of its high mass it couples strongly to the Higgs boson and to hypothetical particles outside the SM with high masses. Therefore, knowledge of its properties are of importance for a lot of searches for new physics and stability checks of the SM and new theory models. Due to its small lifetime of $\tau_{\mathrm{t}} = 5 \times 10^{-25}\,\mathrm{s}$ the top quark does not hadronize before its decay, unlike other quarks [10]. This provides on the one hand the opportunity to measure the properties of a "bare" quark, on the other hand it makes the theoretical definition of its mass more complicated, which will be sketched in section 2.2.2.

2.2.1 Phenomenology

In the following the top quark phenomenology, specifically in proton-proton colliders, will be described.

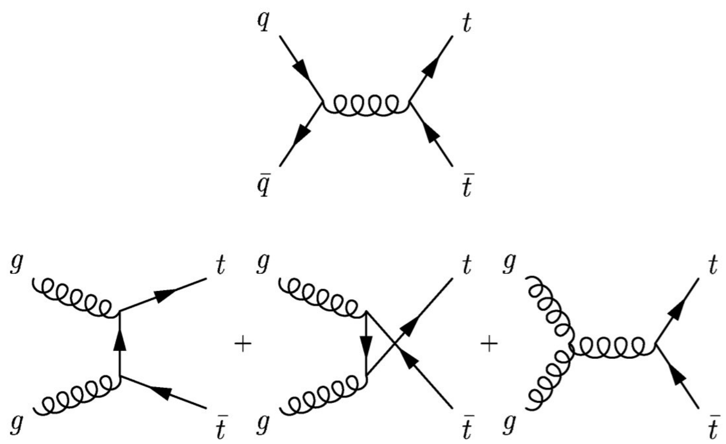

Figure 2.2: Leading order $\mathrm{t\bar{t}}$ production diagrams through quark-antiquark (top) and gluon-gluon (bottom) interaction [10].

Top quark production In high-energy hadron colliders top quarks can be produced in leading order (LO) through gluon-gluon, quark-antiquark and gluon-(anti)quark interaction. Either a top - anti-top quark pair can be produced through QCD or a single (anti-) top quark through electroweak interaction.
All possible LO top quark pair production diagrams are shown in figure 2.2.

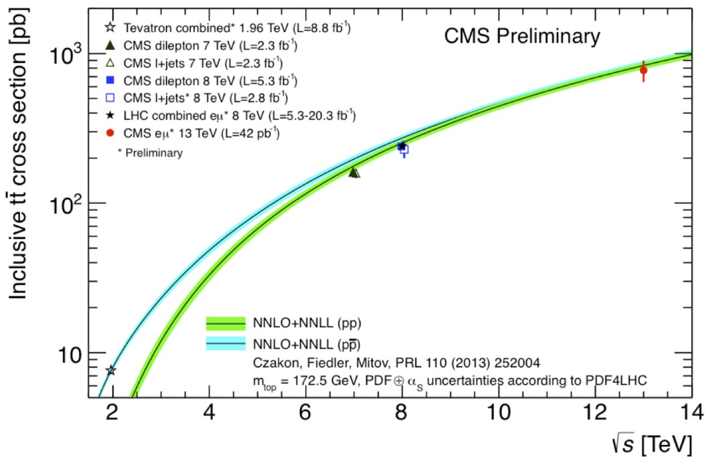

Figure 2.3: The $\mathrm{t\bar{t}}$ production cross section as function of the center-of-mass energy $\sqrt{s}$ for proton-proton (green) and proton-antiproton (blue) collisions. [11]

The predicted and measured cross section of top quark pair production at hadron colliders is shown in figure 2.3 and agree well. For a top quark mass of $m_\mathrm{t} = 172.5\,\mathrm{GeV}$ the production cross section at a proton-proton collider with a center-of-mass energy of $\sqrt{s} = 13\,\mathrm{TeV}$ is predicted at an order of NNLO+NNLL to be $\sigma_{\mathrm{t\bar{t}}}^{\mathrm{NNLO+NNLL}} = 832^{+40}_{-46}\,\mathrm{pb}$. With the CMS experiment, a cross section of $\sigma_{\mathrm{t\bar{t}}} = 835.6 \pm 32.1\,\mathrm{pb}$ has been measured at this center-of-mass energy with a data sample corresponding to a integrated luminosity of $2.3\,\mathrm{pb}^{-1}$ [12].

Top quark decay Because FCNC (flavor changing neutral currents) are absent in the standard model, a (anti-)top quark can decay only into a down-type (anti-) quark and a $\mathrm{W}^{-/+}$. The relative probabilities of the three possible decays are given by the CKM matrix. Only the decay $\mathrm{t \to bW}$ has the noticeable probability of approximately 0.998. The subsequent decay of the W boson is possible leptonically into one lepton and one neutrino or hadronically into a quark-antiquark pair, that subsequently decays into jets of hadrons. Top quark pair decays are categorized by the decay of the two W bosons. The branching ratios of possible LO top quark pair decays are listed in table 2.1

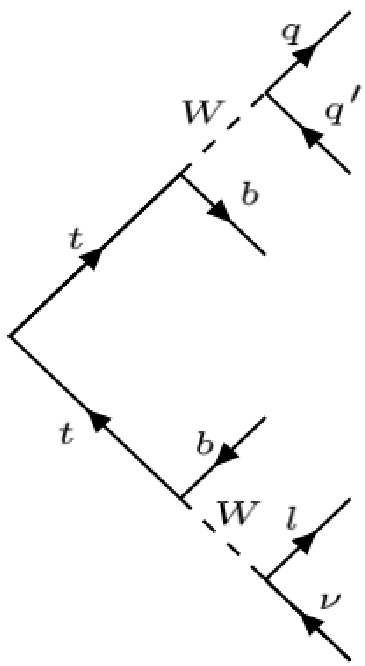

Figure 2.4: LO decay of a top quark pair in the lepton+jets channel.

The branching fraction (BR) of a $t\bar{t}$-decay with two leptons in the final state (dilepton) is approximately 1/9, the ratio of no leptons in the final (all-jets) state 4/9, and the ratio of one lepton (lepton+jets) 4/9. Each channel has its own benefits and difficulties for selecting top quark events and extracting a interesting observable. The dilepton channel provides a rather clean sample when Drell-Yan background is suppressed, but has a small branching ratio and, due to the two neutrinos in the event, a higher energy uncertainty than the other channels. The all-jets channel delivers a good branching ratio and all energy of the event can be measured, but has a multi-jet background that has to be controlled. In this thesis decays with one muon and jets in the final state will be analyzed. With b-jet identification it features a clean selection and a good constraint kinematic. A diagram of a possible LO decay in this channel is shown in figure 2.4.

2.2.2 The top quark mass

Global interest The longer particles of physics beyond the standard model can not be observed, the more interesting becomes a precise understanding of SM particle and its observables. These observables can be fitted in different combination, to test the standard model and its numerical values. This highly effects the physics interpretation of the theory. One example for

Table 2.1: Approximated branching ratios for all top quark pair decay modes in dependence of the W boson decays.

$BR(t\bar{t} \to b\bar{b} + X)$	$e^+\nu_e$	$\mu^+\nu_\mu$	$\tau^+\nu_\tau$	$q\bar{q}'$
$e^-\bar{\nu}_e$	1/81	1/81	1/81	2/27
$\mu^-\bar{\nu}_\mu$	1/81	1/81	1/81	2/27
$\tau^-\bar{\nu}_\tau$	1/81	1/81	1/81	2/27
$q\bar{q}'$	2/27	2/27	2/27	4/9

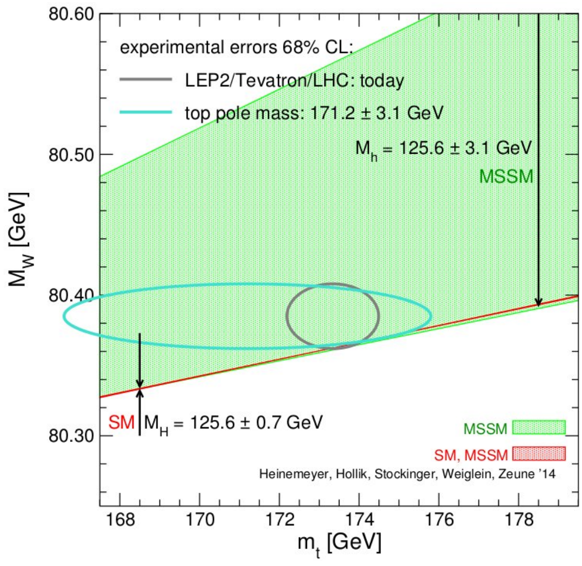

Figure 2.5: The measured top quark pole mass in relation to the W boson mass with their 1σ uncertainties in comparison to the SM prediction (red) and MSSM prediction (green). [13]

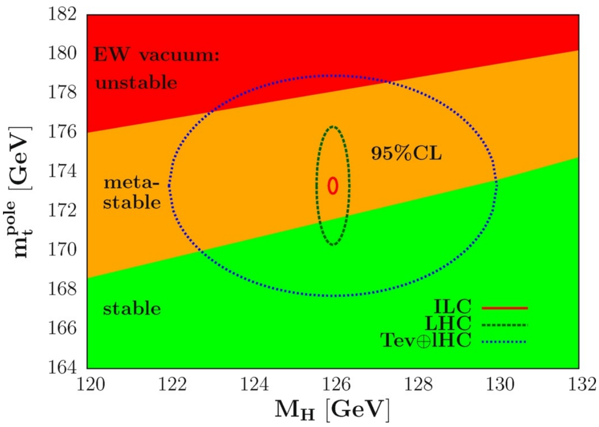

Figure 2.6: The measured top quark pole mass in relation to the Higgs boson mass with their 2σ uncertainties in caparison to the areas in which the SM vacuum is absolutely stable, meta-stable, and unstable, up to the Planck scale. The LHC top quark mass is the 2014 world average. [14]

such an observable is the mass of the top quark. In figure 2.5 the SM and Minimal Supersymmetric Standard Model (MSSM, see reference [16]) prediction of the relation of the top quark mass and W boson mass are compared with the experimental results. In figure 2.6 the relation of the measured top quark mass, the Higgs boson mass, and the vacuum stability prediction of the standard model are showcased. In both cases the measurement agreed with the SM prediction but still leave room for alternatives. In figure 2.7 the confidence level of M_W to m_t scans in respect to the SM is shown. The agreement of global fit and measurement is an important consistency demonstration of the SM.

The invariance under CPT transformation in the standard model implies equal masses for particles and antiparticles. The difference between the top quark mass and anti-top quark mass $\Delta m_\mathrm{t} = m_\mathrm{t} - m_{\bar{\mathrm{t}}}$ has been measured in the lepton+jets channel at $\sqrt{s} = 8\,\mathrm{TeV}$ at the CMS detector to be $\Delta m_\mathrm{t} = -272 \pm 231\,\mathrm{MeV}$ [17].

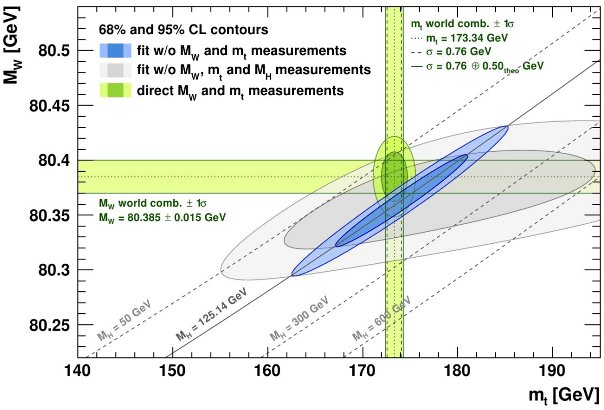

Figure 2.7: Contours of 68% and 95% CLobtained from M_W to m_t scans within the SM. [15]

Mass definition The mass of macroscopic and classical particles is easily defined by relativistic kinematics and can be calculated simply out of their energy and momentum as $m^2 = E^2 - \vec{p}^2$. It is called "invariant" mass due to its invariance under Lorentz transformation. This definition will be used technically for the studied event hypotheses. The "real" quark mass is not a physical observable. In QCD the quark mass is a parameter of the Lagrangian. If not only the LO interaction of the quark, but also possible particle loops that can appear due to quantization, are taken into account, the Lagrangian has to be renormalized. The mass definition then depends on the scheme with which the renormalization is done.

The conventional choice for many QCD applications is the pole mass. With the introduction of additional orders of perturbation, the propagator of the particle changes in following way:

$$\frac{i}{\not{p} - m_0} \Rightarrow \frac{i}{\not{p} - \underbrace{m_0(\Lambda)}_{\text{'bare' mass}} - \underbrace{\delta m_0(\Lambda)}_{\text{divergent}} - \underbrace{\Sigma' m_0(\Lambda)}_{\text{finite}}} := \frac{i}{\not{p} - m^{\text{pole}}}$$

with the renormalization scale Λ.

For heavy quarks however this definition has its shortcomings. Because of confinement, quarks in asymptotic states do not appear as free particles, and non-perturbative corrections must be added. This leads to an uncertainty of the pole mass in the order of $\Lambda_{\mathrm{QCD}} \approx 200\,\mathrm{MeV}$ [18]. Below Λ_{QCD} the strong coupling becomes large and perturbation theory is no longer applicable. Another scheme that is used instead, is the $\overline{\mathrm{MS}}$ scheme. It is a short-distance mass scheme, based on running masses, that depend on a scale μ. Typically $\mu = m_\mathrm{t}$ is chosen. The difference between the $\overline{\mathrm{MS}}$ mass $\bar{m}$ and m^{pole} can be approximated by perturbation theory. The value depends on how many loops of QCD and QED corrections are taken into account.

More generally than the $\overline{\text{MS}}$ scheme, a short-distance mass scheme can introduce an associated scale R. This MSR mass can be related to m^{pole} through the pertubative series

$$m^{\text{pole}} = m^{\text{MSR}}(R,\mu) + R\sum_{n=1}^{\infty}\sum_{k=0}^{n} a_{nk}\alpha_s^n(\mu)\ln^k\left(\frac{\mu^2}{R^2}\right) ,$$

with the correction coefficients a_{nk}.
The MSR mass is convenient, as it it directly related to the $\overline{\text{MS}}$ scheme through

$$m^{\text{MSR}}(\mu,\mu) = m^{\overline{\text{MS}}}(\mu)$$

and interpolates to the pole mass

$$\lim_{R\to 0} m^{\text{MSR}}(R,\mu) = m^{\text{pole}} .$$

Examples for the top quark mass in different schemes for up to three QCD loops were calculated by reference [19] and are given in table 2.2. The calculation including the fourth QCD loop can be found in reference [20]. The influence of QED correction in the relation between pole and running masses is analyzed in reference [21].

Table 2.2: The top quark mass in the MSR scheme at different scales, in the $\overline{\text{MS}}$ scheme at $\mathscr{O}(\alpha_s^3)$ for $\alpha_s(M_Z) = 0.1185$ converted from $m^{\text{MSR}}(3\,\text{GeV})$, and the pole mass at 1, 2, and 3 loop converted from the $\overline{\text{MS}}$ mass. All numbers are given in GeV and $m_{\text{t}}^{\text{MSR}}(R) := m_{\text{t}}^{\text{MSR}}(R,\mu = m_{\text{t}})$. [19]

$m_{\text{t}}^{\text{MSR}}(1)$	$m_{\text{t}}^{\text{MSR}}(3)$	$m_{\text{t}}^{\text{MSR}}(9)$	$m_{\text{t}}^{\overline{\text{MS}}}(m_{\text{t}})$	$m_{\text{t,1-loop}}^{\text{pole}}$	$m_{\text{t,2-loop}}^{\text{pole}}$	$m_{\text{t,3-loop}}^{\text{pole}}$
173.72	173.40	172.78	163.76	171.33	172.95	173.45

The top quark mass, that is measured by most analyses, is none of this schemes. It is derived by a fit on mass-sensitive distributions, that extract a value corresponding to the input mass, that were used in the Monte-Carlo (MC) event simulation. (see chapter 4)
The world combination (2014) of such measurements by the experiments Atlas, CDF, CMS, and DØ is $m_{\text{t}} = 173.34 \pm 0.27(\text{stat.}) \pm 0.71(\text{syst.})\,\text{GeV}$ [22]. The most precise analysis on the top quark mass, in the lepton+jets channel of the $\text{t}\bar{\text{t}}$ decay, was done with an approach, that will be explained in chapter 7. It was published in 2015 by CMS and had a result of $m_{\text{t}} = 172.38 \pm 0.16(\text{stat.}) \pm 0.49(\text{syst.})\,\text{GeV}$ [23].

There are concerns, that this Monte-Carlo mass can not be easily translated into a theoretically well motivated mass. One approach for such a translation is, to take a short-distance mass defi-

Table 2.3: Central values and uncertainties out of the calibration of $m_t^{MC} = 173\,\text{GeV}$ into theoretical mass schemes, all in GeV and $m_{t,R}^{MSR} := m_t^{MSR}(R, \mu = m_t)$. σ combines the uncertainty due to perturbation and the incompatibility. [24]

$m_t^{MC} = 173\,\text{GeV}$

mass scheme	order	central	σ
$m_{t,1\,\text{GeV}}^{MSR}$	NLL	172.80	0.29
$m_{t,1\,\text{GeV}}^{MSR}$	NNLL	172.82	0.22
m_t^{pole}	NLL	172.10	0.38
$m_{t,}^{pole}$	NNLL	172.43	0.28

nition, were the range R is adjusted to the energy threshold of pertubative shower description in the Monte-Carlo simulation. This leads to an uncertainty in the order of 1 GeV. In reference [19] the Monte-Carlo mass was translated into a MSR mass, and than through the $\overline{\text{MS}}$ scheme, into a pole mass. This resulted into a numerical difference for the world average top quark mass of $m_t^{pole} - m_t^{MC} = 0.05^{+0.32}_{-0.62} \pm 0.50\,\text{GeV}$, with the conclusion that MC mass results are expected to be close to the pole mass.

Another approach was taken by Hoang et al. in reference [24]. There the dependence of the top quark MC mass in e^+e^- collisions, out of events simulated with `Powheg 8.205`, to the theory mass schemes were evaluated out of the 2-Jettiness [25] distribution. Example results of this calibration are given in table 2.3. In figure 2.8 the MSR mass for different m_t^{MC} values is shown. While both approaches agree within their uncertainty, the question to which level they are transferable to the measurement in this thesis is under ongoing studies as is the theoretical top quark mass as a whole.

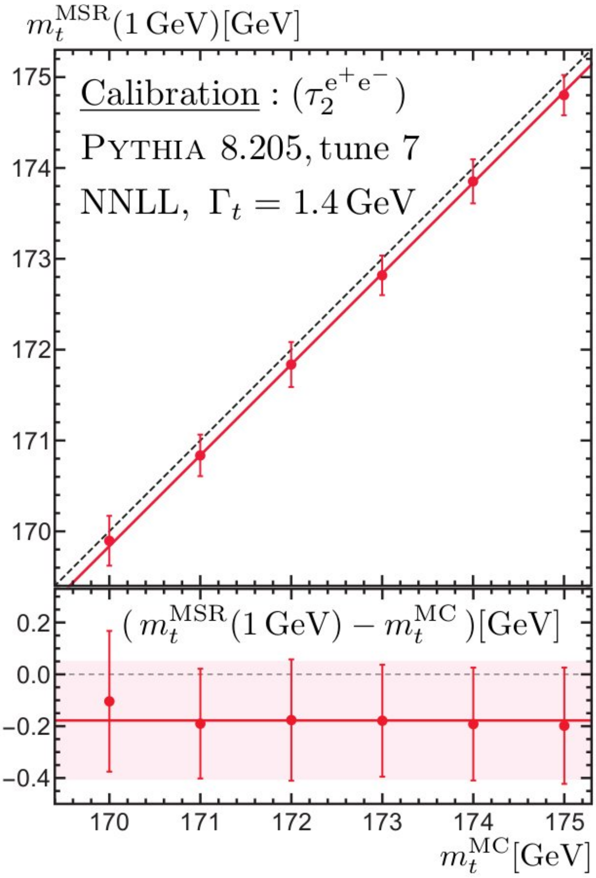

Figure 2.8: Dependence of the NNLL fit result for the MSR mass on the input m_t^{MC} value in `Pythia`. [24]

3 Experimental setup

3.1 The Large Hadron Collider

The Large Hadron Collider (LHC), at the European Organization for Nuclear Research (CERN) in Geneva, is a synchrotron and storage ring for protons and heavy ions. With a circumference of 26.7 km, it is the largest single machine ever build by mankind. The center-of-mass energy is designed to be 14 TeV in proton-proton collision operation. There are four experiments at the LHC, observing the particles out of the collisions. ALICE (A Large Ion Collider Experiment) is mainly focusing on the research of the products and observables of heavy ion collisions, while LHCb (LHC beauty experiment) observes b quarks produced in the forward direction. The two other, ATLAS and CMS (Compact Muon Solenoid), are focusing on the observation of the final states of the proton-proton collisions.

The first collisions at the LHC started in 2009 and lead to the discovery of a Higgs-like particle in 2012, with a center-of-mass energy of 8 TeV. Since 2015 the LHC is running in its second run period with a center-of-mass energy of 13 TeV.

The protons for the collision are produced by ionizing hydrogen gas with an electron beam. Before they can be injected into the LHC, they run through several pre-accelerator steps. This is necessary to get a high energy beam with an acceptable emittance.

The first step of the chain is a linear accelerator that accelerates the protons from a kinetic energy of about 100 keV to 50 MeV via radio-frequency cavities. It follows the Proton Synchrotron Booster. There, the head and tail of the beam are dumped and the middle part is separated into four bunches, each with 4 ns length. The bunches leave this step with an energy of 1.4 GeV. In the next step the bunches are injected into the Proton Synchrotron, with a bunch spacing of 25 ns or 50 ns, as required for the LHC operation. In the Proton Synchrotron, the protons are accelerated to 25 GeV and passed on to the Super Proton Synchrotron where the their energy is increased to the LHC injection energy of 450 GeV. [26] In the LHC, the beam can be stable for

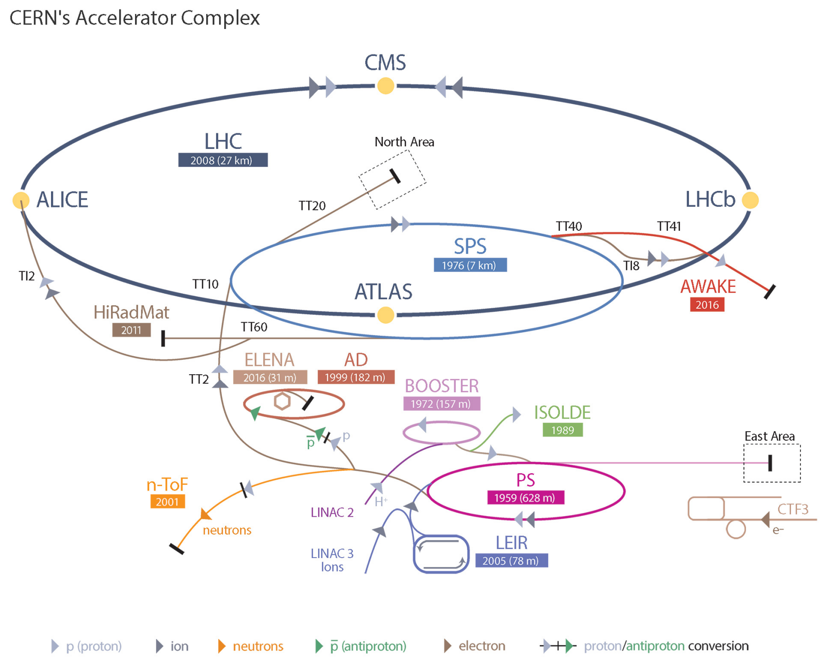

Figure 3.1: Schematic overview of the LHC preaccelerator chain. [28]

about 8 hours before the LHC has to be filled again. [27]

The characteristic property of a particle physic collider is the *instantaneous luminosity* L. It describes the collision activity. For circular colliders it can be calculated straight forward out of equation (3.1). The frequency of proton bunches colliding f, the number of protons per bunch N_i, and the bunch profile in the transverse directions $\sigma_{x/y,i}$ are taken into account.
For a given production cross-section hypotheses σ follows the expected event count out of the integrated luminosity $L_{int} = \int L dt$ as $n = \sigma L$.

$$L = \frac{f N_1 N_2}{2\pi \sqrt{\sigma_{x,1}^2 + \sigma_{x,2}^2} \sqrt{\sigma_{y,1}^2 + \sigma_{y,2}^2}} \tag{3.1}$$

The integrated Luminosity, that was recorded by CMS in 2015, is plotted in figure 3.2. The data that is analyzed in this thesis corresponds to a integrated luminosity of $2.2\,\mathrm{fb}^{-1}$.

The nominal beam parameters of the LHC at Run II in proton-proton operation are listed in table 3.1. For a detailed description, refer to the LHC design report [30].

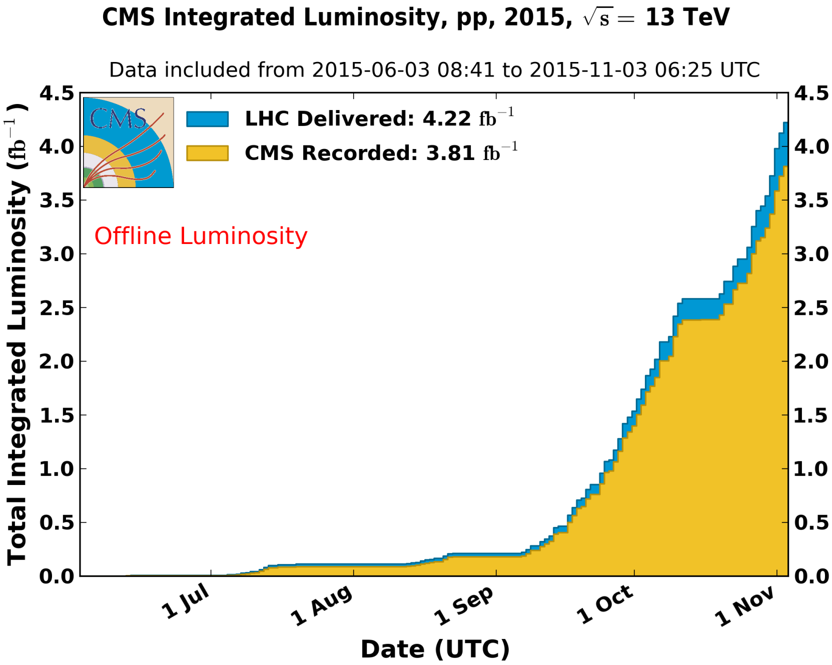

Figure 3.2: Cumulative offline luminosity versus week delivered to (blue), and recorded by CMS (orange) during stable beams and for p-p collisions at 13 TeV center-of-mass energy in 2015. [27]

3.2 The Compact Muon Solenoid detector

The Compact Muon solenoid (CMS) detector, named according to the two most massive features of its appearance, is a multi-purpose particle detector at the LHC. "Compact" describes a circumference of 15 m and length of 28.7 m, while weighting about 14 000 t. The detector has a onion-like structure, with each layer being specialized for detecting the observables of a distinct particle type and covers nearly all angles around the interaction point. The different layers are easily spotted in figure 3.3. The only particles of the standard model, that can not be detected by this detector, are neutrinos. With good transverse energy resolution and known efficiencies, a hypotheses of their kinematic properties is still calculable. A illustration of the signatures of different particle types can be found in figure 3.4. While each of the layers will be described roughly in the following, a more detailed description, including performance studies, can be found in the references [31, 32].

Table 3.1: Overview of the LHC beam properties. [29, 30]

parameter	value
proton energy	6.5 TeV
bunches per beam	2808
proton per bunch (at start)	1.2×10^{11}
RMS bunch length	7.55 cm
RMS bunch width	16.7 µm
instantaneous luminosity (design)	$10^{34}\,\mathrm{cm^{-2}s^{-1}}$
collision rate	40 MHz
energy loss per round	max. 6.71 keV
beam collision angle	285 µrad
max. magnetic dipole field	$0.535 \rightarrow 8.33$ TeV

3.2.1 Solenoid Magnet

To be able to measure the momenta of charged particles and distinguish the sign of their charge, a magnetic field is inducted in the detector. The detector is designed for a field strength of up to 4 T in the center, but for stability reasons operated with 3.8 T. The field is generated by a solenoid with a inner circumference of 295 cm and a length of 12.9 m, containing 53 km superconducting niobium-titanium cable in 2168 windings. It is operated with a current of 19.5 kA. The structure includes a iron yoke for the magnetic return flux, in which the field strength is still 2 T. To minimize its energy absorbtion from the particles we want to measure while maximizing the field strength in the tracker, the solenoid is placed between the hadronic calorimeter and the muon system.
The strong magnetic field makes it possible to measure transverse momenta with high resolution.

3.2.2 Tracker

The first part of the detector, that is passed by particles out of the collision point, is the silicon tracker, out of barrels and disks of silicon-pixel and silicon-strip sensors. It covers the whole ϕ range and a pseudorapidity up to $|\eta| < 2.5$. The material budget of this detector part has to be minimal, so that no particle tracks are altered. The radiation length of the tracker reaches from 0.4 in the barrel to two in the transition between barrel and endcaps. Closest to the beam line are three barrel layers of silicon-pixels with radii of 4.4 cm to 10.2 cm around the detectors

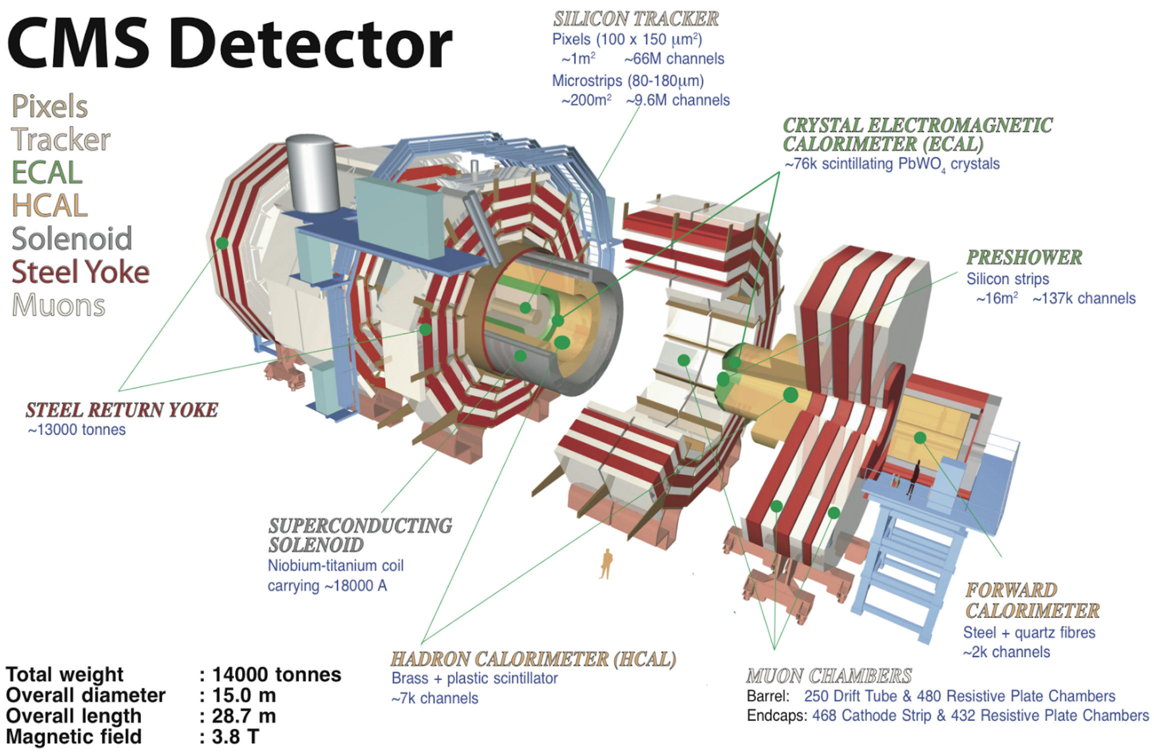

Figure 3.3: Overview of the CMS detector with all its subsystems. [33]

z-axis, with two end-caps on either side, with distances of 34.5 cm and 46.4 cm to the interaction point. Each of the 66 million hybrid-pixel-sensors has a size pf $100 \times 150\,\mu\text{m}^2$. The pixels of one layer are tiled on each other and shifted against the next layer, so that a resolution of 10 μm in r-ϕ and 20 μm in z direction is obtained.

The silicon strip tracker has a length of 5.8 m and a outer radius of 0.55 m. The 320 μm and 500 μm wide strips are arranged with a spacing of 80 μm to 180 μm between them in 6 barrels around the beam pipe and 12 caps on each side.

Due to the two-dimensional hit information, a resolution of 23 μm to 52 μm orthogonal to the stripes can be obtained.

Out of the curvature of the tracks of charged particles in the magnetic field, their transverse momenta are calculated with a relative resolution of about $\frac{\Delta p_T}{p_T} = 1.5 \cdot 10^{-4} p_T/\text{GeV} + 0.005$. The resolution is better for small $|\eta|$ and worse for high $|\eta|$.

Primary and secondary vertices of the particle decays can be identified in the tracker and are used for particle identification.

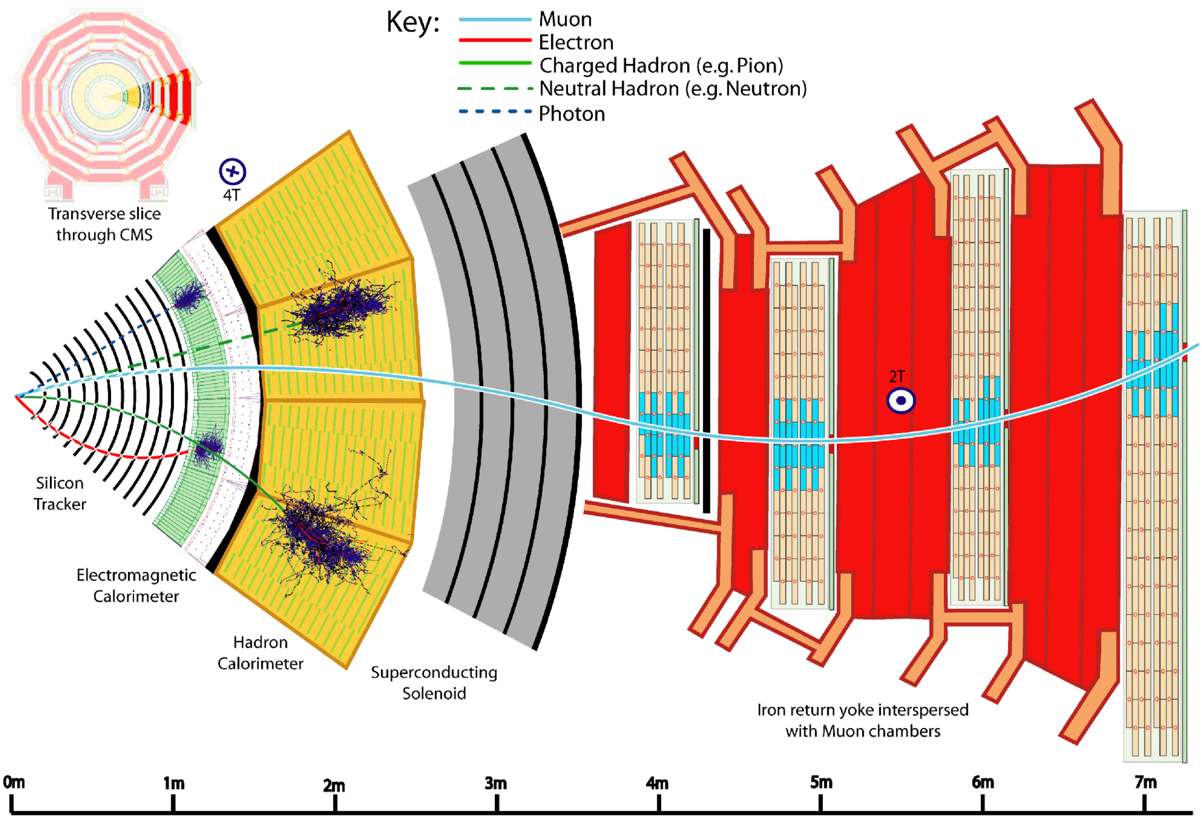

Figure 3.4: Cut through the ϕ-plane of the CMS detector were the signatures of different particle types are illustrated. [34]

3.2.3 Calorimeters

The next layers of the detector are the electromagnetic calorimeter (ECAL) and the hadronic calorimeter (HCAL).

The ECAL is designed to absorb as much energy of electrons and photons as possible. Therefore 75 848 scintillating lead tungstate crystals are arranged in a barrel with a radius of 0.65 m, covering $|\eta| < 1.5$, and caps, covering $1.5 < |\eta| < 3.0$. Each crystal is 23 cm long with a $22 \times 22\,\text{mm}^2$ face tilted 3° towards the nominal interaction point, covering a $\Delta\phi \times \delta\eta$ surface of 0.0174 at $\eta \approx 0$.

The length of the lead tungstate crystals corresponds to 25.8 radiation lengths. The scintillation light is detected by silicon avalanche photodiodes in the barrel and vacuum photodiodes in the caps.

The relative energy resolution of the ECAL was measured with a electron test beam and is

$$\left(\frac{\sigma}{E}\right)^2 = \left(\frac{3.63\%\sqrt{\mathrm{MeV}}}{\sqrt{E}}\right)^2 + \left(\frac{124\,\mathrm{MeV}}{E}\right)^2 + 0.26\%^2 \,, \tag{3.2}$$

which yields a resolution of 0.4 % for 100 GeV electrons.

The ECAL is surrounded by the HCAL for the measurement of the hadronic parts of particle jets. In the HCAL, it is crucial, the energy of all hadrons is absorbed. Therefore it is build out of 0.37 cm thick platic scintillators as active material with 5 cm thick brass plates as absorber between them. Passing particles shower in the absorber. The energy of the shower then produces scintillator light which is frequency shifted and channeled into hybrid photodiodes. In the barrel region ($|\eta| < 1.4$) each HCAL segment covers a region of $\Delta\phi \times \delta\eta = 0.087$. In the endcaps the segmentation varies in $\Delta\phi$ from 5° to 10° and in $|\eta|$ from 0.087 to 0.35. Additionally there are in $|\eta| < 1.26$ scintillator layers behind the solenoid, and forward HCALs in $3 < |\eta| < 5$ at a distance of 11.2 m in z from the nominal interaction point.
In the barrel region, the HCAL is about 10 hadronic interaction length thick. The relative energy resolution in dependence of the transverse energy E_T^{MC} simulated with Pythia [35, 36], results in

$$\frac{\sigma\left(\frac{E_T^{rec}}{E_T^{MC}}\right)}{\left\langle\frac{E_T^{rec}}{E_T^{MC}}\right\rangle} = \frac{5.6\,\mathrm{GeV}}{E_T^{MC}} + \frac{1.25\sqrt{\mathrm{GeV}}}{\sqrt{E_T^{MC}}} + 0.033 \,. \tag{3.3}$$

3.2.4 Muon system

Around the HCAL is the solenoid and around the solenoid the muon system. Because of the density of HCAL and solenoid, the muon system has a high muon identification purity.
The $|\eta| < 1.2$ barrel region of the system consists of aluminum drift tubes that provide a resolution of 100 µm and resistive plate chambers that provides a fast response time. In the endcaps, cathode strip tubes are installed instead of drift tubes. The cathode strip tubes provide a resolution of 100 µm×100 µm and are optimized for neutral background.
The time resolution of the whole system is around 3 ns, which provides excellent trigger capabilities. The momentum resolution for muons is enhanced by combining information out of the tracker and the muon system to $\frac{\Delta p_T}{p_T}|_{p_T=1\,\mathrm{TeV}} = 5\%$ and $\frac{\Delta p_T}{p_T}|_{p_T=100\,\mathrm{GeV}} = 1\%$.

3.2.5 Trigger

The LHC is operating with a 25 ns bunch spacing. This translates to a bunch crossing rate of 40 MHz, with approximately 20 simultaneous pp collisions per crossing at design luminosity. Because only 1000 events per second can be written in permanent storage a very elaborated trigger system is needed. At CMS, the trigger system is divided in two parts.

The first part is the Level-1 trigger, built out of custom hardware with local, regional and global components, partially built directly onto the detector components and partially located in a underground control room about 90 m away from the detector. It uses reduced granularity of the detector components and scans for events with high-energetic particles and calculates the total transverse energy. The L1 trigger is designed for a continuous output rate of 30 kHz. and has an latency of 3.2 µs. For this time processing is be pipelined. Therefore a quasi deadtime free operation is accomplished.

The second trigger stage, the high-level-trigger, is using a farm of standard processors where the information of all detector subsystems are entered and analysis-like calculations can be done. The total rate of events that passed both triggers is 920 Hz. Prescales are applied to keep the rate constant for different luminosities. The data is fully reconstructed available for analysis within 48 hours.

3.2.6 CMS coordinate system

All described particles in this thesis will be characterized by their kinematic variables. Out of this variables the observables of different questions of interest can be derived. The Lorentz vector, one time and three space coordinates or equivalent one energy and three momentum coordinates, describe the kinematics of a particle fully.

The transverse momenta of the colliding particles with respect to the beam is negligible and the resolution of the detector depends highly on the angle to the beam. Therefore typically no Cartesian coordinates are used. Used are the azimuthal angle in the x-y plane ϕ, were x points radial into the center of the LHC and y away from the earth, and the pseudo-rapidity $\eta = -\ln\tan(\Theta/2)$. The polar angle Θ is defined with respect to the z-axis, that points counter-clockwise to the direction of the beam. $\Delta\eta$ is invariant under Lorentz transformations.

Another often used observable in this thesis is the transverse momentum, defined as $p_T = \sqrt{p_x^2 + p_y^2}$. This coordinate system of the CMS detector is described in reference [31].

4 Event generation and simulation

One vital part of all physical experiments is the prediction of their outcome. In high energy particle physics predictions are even more important, because they can be used to get a hold on not directly observable parameters and estimate signal acceptances and efficiencies.
In principal, these can be calculated, but integrals in high-dimensional phase space have to be carried out. The method of choice for this is the Monte-Carlo (MC) method, where ideally such calculations converge with $1/\sqrt{n}$ with n randomly sampled phase space points. The steps that are taken to get from the mathematical formula to data-like predictions will be described in the following. In more detail they can be found in [37].

4.1 Parton distribution functions

The starting point of the simulation is the initial state of the process under consideration. In the case of high energy pp-collision this is not trivial. While for low momentum transfer ($Q^2 \approx 10\,\text{GeV}^2$) large portion of the momentum is carried by the three valence quarks, at higher momentum transfer the contribution of sea (anti-)quarks and gluons increases. The momentum fraction x of the different parts of the proton are described by the parton distribution function (PDF). The PDF can be measured through proton-X scattering angles at experiments like HERA [38]. Usually, PDFs are evaluated at a factorization scale μ_F, the characteristic hard scattering scale of the investigated process, which ensures that all relevant fluctuations are contained. Extrapolations to higher Q^2 in different parametrizations are available from multiple collaborations. One example for two different values of Q^2 is shown in figure 4.1. The use of a different PDF set should have minimal impact on the kinematic of the final state of a process.
The minimal average momentum fraction to produce a top-quark pair at $\sqrt{s} = 13\,\text{TeV}$ is $x = \sqrt{x_1 x_2} \geq 2m_\text{t}/\sqrt{s} \approx 0.027$.

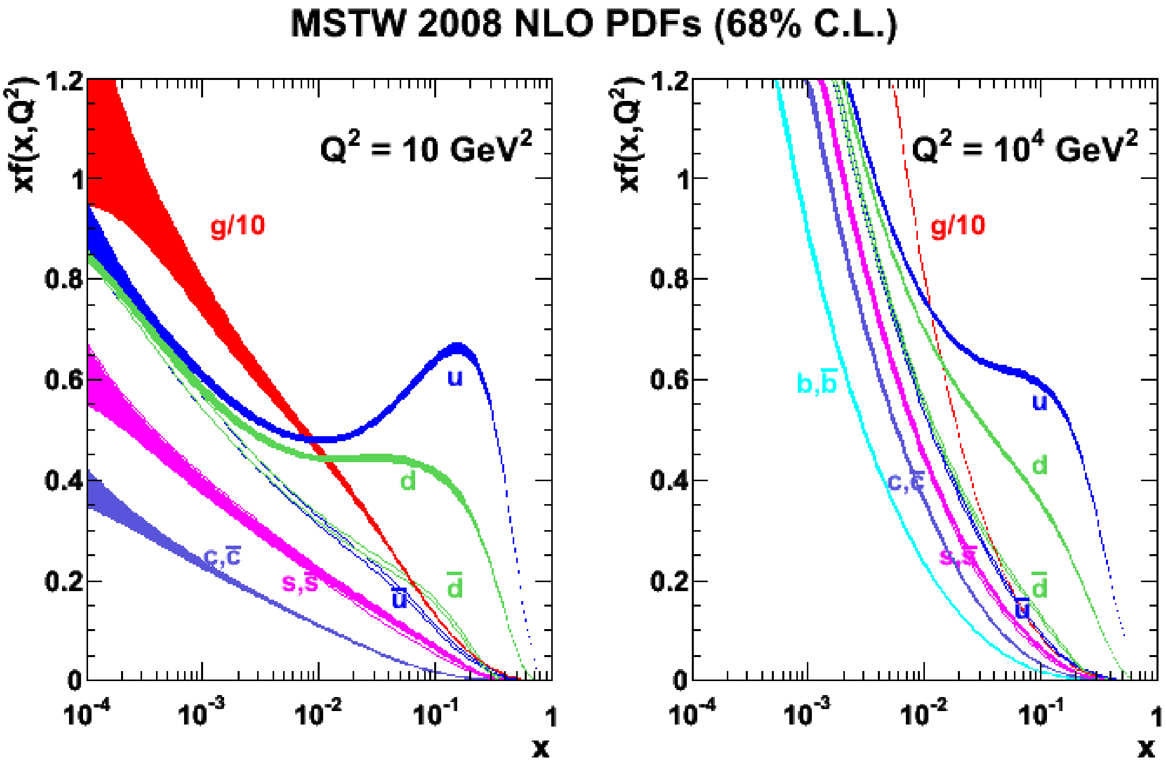

Figure 4.1: The MSTW2008NLO parton distribution function for different values of Q^2. [39]

4.2 Hard scattering and parton showering

The hard scattering differential cross-section in pertubation theory, for a final state *fin*, is given by

$$d\sigma_{\text{fin}} = \sum_{k=0}^{\text{legs}} d\Phi_{\text{fin}+k} \Big| \sum_{l=0}^{\text{loops}} \mathscr{M}^{(l)}_{\text{fin}+k} \Big|^2 ,$$

where $\Phi_{\text{fin}+k}$ is the momentum configuration and $\mathscr{M}^{(l)}_{\text{fin}+k}$ the matrix element with k additional outgoing particles (legs) and l additional loops. The matrix elements are calculated by generators like `Powheg` [40]. In the samples that are used in this thesis, the events were calculated with up to 5 additional outgoing particles and one internal loop. The result suffers from cuts on momenta and angles that are required for the calculation. The infrared divergence from soft and collinear partons are no problem. Due to unitary they cancel each other out, as is stated in the Kinoshita-Lee-Nauenberg theorem [41].

The quark and gluon transformation into jets is simulated by a parton showering algorithm. A shower is characterized by its width. In the `Pythia 8` tool, the width is defined by the p_t of the shower particle in regard to the emitting parton. The showering is done step by step until a cutoff scale Q_0 is reached. The Sudokov factor [42] is used, that gives the probability of no emission between two Q scales. A typical cutoff scale is $Q_0 = 1\,\text{GeV}$.

4.3 Hadronization

Below the cutoff scale, hadrons are formed out of the quarks and gluons. The method with which this is done in `Pythia` is the Lund string model [43]. There, color strings are spanned between quark-antiquark pairs. Gluons are treated as "kinks" in these strings. The potential energy between the quarks is lowered by the production of new quark-antiquark pairs. Heavy quarks are suppressed and the transverse momentum to the string direction is smeared with a Gaussian distribution. In addition, Hadron decay tables are included in the model and it is tuned, e.g. to e^+e^- data. The tune can have a big impact on the prediction of events in the LHC [44].

Interaction of further partons in the protons, the underlying event, can also have an effect on the hard scattering process. This is enhanced by the geometrical overlap of the two colliding protons and is adjusted for, by the tuning of the simulation to collision data.

With color reconnection models, non-pertubative changes to the color configuration of an event are possible before the hadronization stage. This can improve the mean transverse momentum and multiplicity in minimum bias events for charged particles with the use of data information. A color reconnection model is implemented in `Pythia 8`.

5 Event reconstruction

Before the analysis dependent selections and evaluations, the data from the detector is reconstructed. An intermediate state are the track candidates and clusters that were recorded and combined from different detector components into into physics object.

5.1 Primary vertex identification

At the high luminosities of the LHC operation an average of 21 interactions per bunch crossing is expected. To identify the interaction that triggered the data taking and to exclude particles from other interactions, its primary vertex is identified. For the reconstruction of the primary vertex, charged particle tracks with the least distance to the beam line, that cross at the same point, are selected. Each of the tracks has to be fitted from at least five hits in the inner tracker, including at least two hits in the pixel component with $\chi^2_{\text{(normalized)}} < 20$. [45]
The tracks are then clustered by the `adaptive vertex fitter` [45], which checks the compatibility of the tracks with all possible vertices. For each event, the vertex with the highest $\sum p_T^2$ of its associated tracks is considered the primary vertex, if it is within 2 cm transverse and 24 cm longitudinal distance of the nominal interaction point and its fit has at least four degrees of freedom. Using CMS data at $\sqrt{s} = 7\,\text{TeV}$, the primary vertex resolution was found to be $< 50\,\mu\text{m}$ in all directions. [45]

5.2 Particle flow

All CMS sub-detector systems are combined to identify particles in a particle-flow (PF) algorithm [46]. First, all tracks associated with muons, easily identified by the muon detector, are removed. The remaining tracks are connected with calorimeter energy deposits. If the energy is significantly larger than the track energy, a overlapping neutral hadron or photon is identified, as is for colorimeter deposits without a track leading to them. Energies in the HCAL are corrected for deposits in the ECAL and non-linear response. On average, a jet consists of 65% charged hadrons, 25% photons, and 10% neutral hadrons.

5.3 Leptons

In the final state, that is observed in this thesis, exactly one lepton is required. Therefore, their identification is crucial. Because of the special challenges in identifying the short living taus, only muons and electrons will be considered.

5.3.1 Muons

With the CMS detector, muons are reconstructed using the inner tracking system and the muon detector outside of the solenoid. To be tagged as *global muon*, a track must have at least 5 hits in the inner tracker, including one in the pixel detector, one hit in the muon chamber, and a $\chi^2/\mathrm{ndf} < 10$ of the track fit. The muon track has to have an impact parameter with respect to the beam spot of $|\Delta d_0| < 0.02\,\mathrm{cm}$ and a maximal distance to the primary vertex of 0.5 cm in beam line direction.
The PF isolation I of a lepton, within a radius R, is defined as

$$I(R) = \left(\sum_{\mathrm{ch}(R)} p_T + \max\left[\sum_{\mathrm{nh}(R)} p_T + \sum_{\gamma(R)} p_T - \frac{1}{2} \sum_{\mathrm{chPU}(R)} p_T, 0 \right] \right) / p_T^{\mathrm{lep}} ,$$

with charged hadrons ch(R), neutal hadron nh(R), photons $\gamma(R)$, and charged hadrons out of pile up chPU(R) within the radius R, in respect to the leptons direction. Muons are selected with $I(\Delta R < 0.4) < 0.15$ as possible signal lepton and with $I(\Delta R < 0.4) < 0.25$ to veto events

with more than one signal lepton.
The muon momentum scale is calibrated with a precision of 2% and has a relative resolution $\sigma(p_T)/p_T$ between 1.5% and 5%. The performance of the CMS muon reconstruction is described in reference [47].

5.3.2 Electrons

Because of their energy loss by bremsstrahlung, electrons are more complicated to identify than muons. The electrons are identified using a multi-variant method, as is described in detail in reference [48]. The efficiency of this identification is 80%. By looking for missing hits in the inner tracking system, electrons from photon conversion are rejected.
Selected electrons are required to have a PF isolation of $I(\Delta R < 0.3) < 0.15$, an impact parameter, with respect to the beam spot, of $|\Delta d_0| < 0.02\,\text{cm}$, and a maximal distance to the primary vertex of 0.5 cm in beam line direction. The energy resolution of PF electrons is better than 4%.

5.4 Jets

Jets are the most complex physics object out of the particle flow. Due to the confinement in QCD, one particle in leading order transforms into jets of multiple particles. Their sum is susceptible to detector effects and additional particles out of pile up. Therefore their energies have to be corrected in value and resolution. Jets that stem from bottom quark decays are idetified using a b-tag algorithm.

5.4.1 Jet clustering

The particles found by the PF algorithm are clustered into jets. A sequential algorithm is used, that is defined by

$$\mathrm{d}_{ij} = \min(p_{T,i}^{2k}, p_{T,j}^{2k}) \frac{(\eta_i - \eta_j)^2 + (\phi_i - \phi_j)^2}{R^2}$$

$$\text{and } \mathrm{d}_i = p_{T,i}^{2k} \,,$$

with the pseudorapidity η and the radius of the characteristic cluster scale R. If the d_i of a particle is smaller than the d_{ij} to every other particle, it is declared a jet and removed from the list of particles. If this is not the case, the two particles with the smallest d_{ij} are clustered together. This is repeated until no particles are left over. This algorithm is collinear and infrared safe and results in different jet shapes for different k's. With $k = -1$ it is called anti-k_T algorithm [49] and results in cone shaped jets with a maximum radius of R. A anti-k_T algorithm with $R = 0.4$ is used for this analysis .
Charged particles that are not associated with the selected primary vertex are not used in the clustering. To suppress fake jets an event is rejected if the charged hadron, neutral hadron, or photon fraction is equal to exactly 0 or 1.

5.4.2 Jet energy

An important property of a jet is its energy or more exactly its transverse momentum. This energy has to be calibrated, which is done in several steps as explained in the following. A more detailed description can be found in reference [50].
For simulation, the "true" energy of the particles, before the interaction with the detector, is known. This information level is called *gen*-level and the jets in it *GenJets*. The recombination level, including all detector effects, is called *reco*-level and tuned to match the "true" energy.
In the first calibration step the offset of additional energy in the jet cone through electronic noise and pile-up is estimated [51].
The second step balances the relative jet response for different η regions of the detector in relation to its central region ($|\eta| < 1.3$). One way of achieving this, is using GenJets. Another possibility is to look at two-jet-events in the recorded data, that include jets in different η regions with the same transverse momentum. In addition to the η-correction, a p_T-depended correction is added, that again can be derived from GenJets or data-driven methods.[1] The relative jet energy response and correction for the 2015 LHC are shown in figure 5.1. They can be found with more details in reference [52]. The uncertainty on the jet energy and the jet energy resolution will be described in section 8 and their effect on the measurement evaluated.

[1] In this thesis the jet energy correction labeled `76X_dataRun2_16Dec2015_v0` is used for data and `76X_mcRun2_asymptotic_RunIIFall15DR76_v1` for simulation.

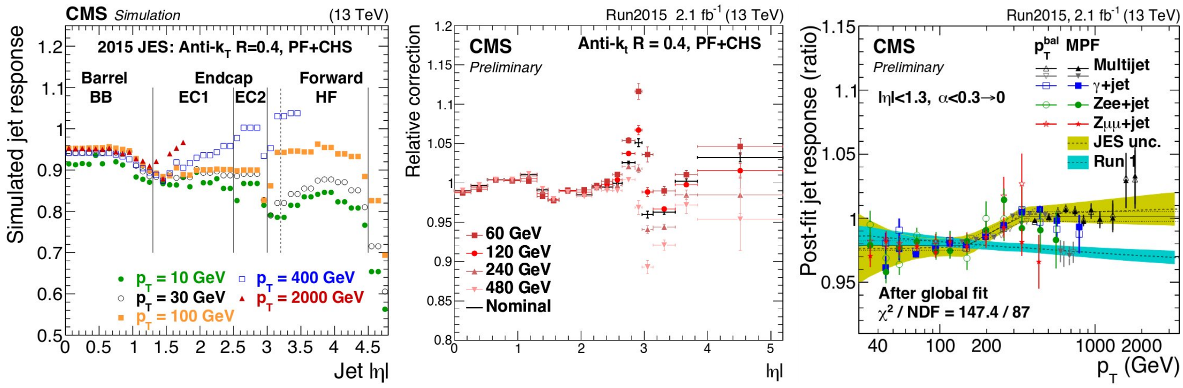

Figure 5.1: Properties of the jet performance at $\sqrt{s} = 13\,\text{TeV}$. The response of jets in simulation (left), the relative correction for simulation to match the data (middle), and the relative response after the jet clustering (right). [52].

5.4.3 B tagging

The final state, that is observed in this analysis, contains two jets originating from bottom quark decays. Therefore an identification of these jets is very helpful. Algorithms for b-jet identification (b-tagging) use unique properties of the bottom quark, such as its mass of about 4.5 GeV and its lifetime in the order of 10^{-12} s, which results in a flight distance of about 7 mm on average when coming out of a top quark decay. In the CMS software, several b-tagging algorithms are implemented, typically with a working point with which the efficiency/mistag -ratio, can be adjusted. Fixed working points are defined as loose, medium, and tight corresponding to 10%, 1%, and 0.1% mistag rate. For this thesis the `Combined Secondary Vertex tracker version 2`(CSVv2) was used, with a medium working point (CSVv2M), that results in an efficiency of about 70%. A comparison to its older version, other tagging algorithms, and its scale factors for simulation/data adjustment, are shown in figure 5.2. Detailed information about b-tagging at CMS can be found in [53–55].

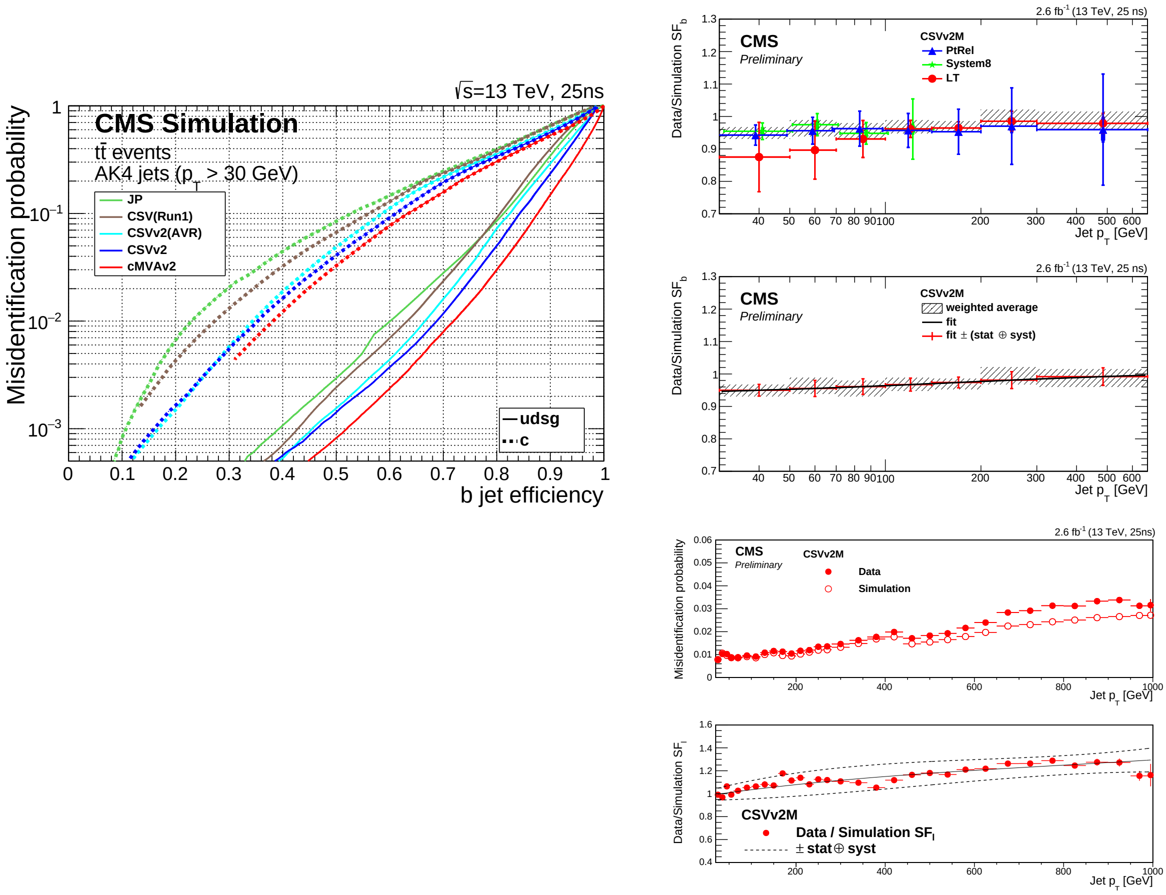

Figure 5.2: The performance of the b jet identification efficiency algorithms demonstrating the probability for non-b jets to be misidentified as b jet as a function of the efficiency to correctly identify b jet for different algorithms/versions (left), the Data-to-simulation scale factor of the b tagging efficiency (SF_b) for CSVv2M as measured with three different methods (right top), the same combined SF_b value with the result of a fit function superimposed (right second from top) and the misidentification probability in data and simulation (right third from top) and data-to-simulation scale factor of the misidenfication probability (right bottom) for the CSVv2M tagging requirement as afunction of the jet-p_T. [55].

5.5 Missing transverse energy

The missing transverse momentum or energy (MET) is defined as

$$\vec{E}_T^{\text{miss}} = - \sum_{i \in \text{PF-particles}} \vec{p}_{T,i} \ ,$$

as the imbalance of all observed particles in an event. All calibrations on jets with $p_T > 15\,\text{GeV}$ are propagated into $\vec{E}_T^{\text{miss}}$. In the standard model the neutrino is the only particle that corresponds to missing energy and one neutrino is expected in the decay channel of this analysis. Outside the standard model other particles are postulated , that can cause a significant amount of missing energy. Therefore, the MET performance of the CMS detector has been carefully validated in reference [56].

6 Event selection

To enrich the fraction of real $t\bar{t} \rightarrow$ l+jets events in the data various phase-space selections and a fit to a $t\bar{t} \rightarrow$ l+jets hypothesis is done. Both have been chosen carefully to avoid correlation to the top quark mass. [1]

6.1 Samples

6.1.1 Data sample

In this thesis the data sample taken in 2015, the first period of the Run 2 of the LHC, is analyzed. Events are required to pass a single-muon trigger, so the analysis is performed on the single muon dataset[2]. The dataset is filtered, to contain only runs were all detector subsystems were working. [3]. This selection corresponds to a integrated luminosity of $2.2\,\mathrm{fb}^{-1}$ at $\sqrt{s} = 13\,\mathrm{TeV}$.

6.1.2 Simulation sample

Various Monte-Carlo simulation samples were used for the development and validation of this analysis. Simulated $t\bar{t}$ signal events were generated with the `Powheg V2` matrix element generator [40], `Pythia 8.205` parton showering [57] using the `CUETP8M1` tune [58,59], and a full simulation of the CMS detector based on `Geant 4` [60]. The $t\bar{t}$ signal events have been generated

[1] The event selection and reconstruction is performed in CMSSW 7.6.3. patch 2. For detector conditions and object calibrations the global tags `76X_dataRun2_16Dec2015_v0` (data) and `76X_mcRun2_asymptotic_RunIIFall15DR76_v1` (simulation) are used.

[2] /SingleMuon/Run2015D-16Dec2015-v1/MINIAOD

[3] with the `JSON` file Cert_13TeV_16Dec2015ReReco_Collisions15_25ns_JSON_Silver.txt

for seven different top-quark mass values ranging from 166.5 GeV to 178.5 GeV. For the background prediction, simulation samples with W/Z+jets, single-top, Diboson and QCD-multijet states have been processed. In addition, several samples were simulated for the estimation of systematic uncertainties. They are listed here as well, but will be explained in more detail in chapter 8. All samples are normalized to their theoretical predicted cross-section described in references [61–69]. The cross-section of the $\mathrm{t\bar{t}}$ signal with the default top-quark mass of m_{t} is $\sigma = 831.76^{+19.77}_{-29.20}(\text{scale uncert.})\,^{+35.06}_{-35.06}(\text{PDF+}\alpha_{\mathrm{S}}\text{ uncert.})\,^{+23.18}_{-22.45}(\text{mass uncert.})\,\mathrm{pb}$. The complete list of used MC samples is given in table 6.1, including their cross-sections predictions σ and their order. Events in samples that were generated with `amc@NLO` can have negative weights, that were accounted for in their normalization.

The simulation includes effects of additional overlapping minimum-bias events (pileup). These are weighted, to match their distribution in data, as is shown in figure 6.1. The different labels of the $\mathrm{t\bar{t}}$ signal will be explained later. Furthermore, the jet energy resolution in simulation is scaled to match the resolution observed in data [70].

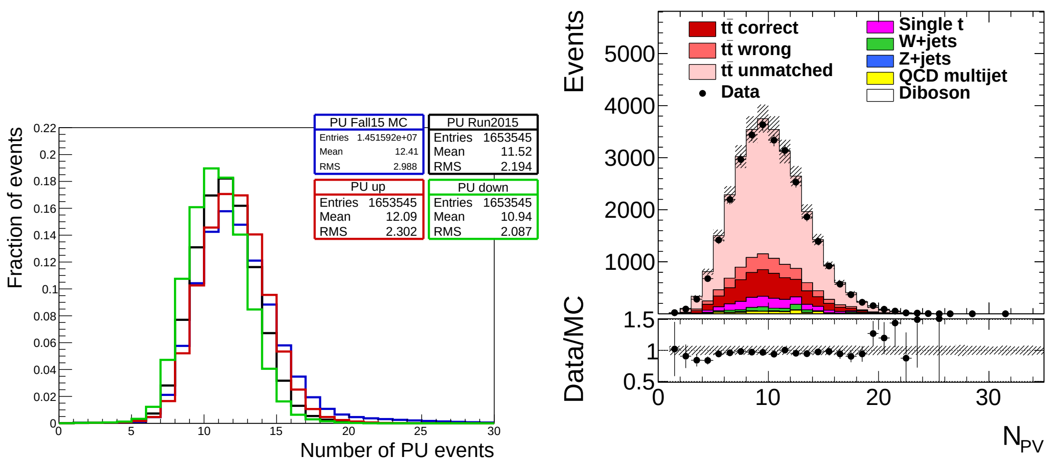

Figure 6.1: Number of pileup events in Fall simulation and data with up/down uncertainties (left) and number of reconstructed primary vertices after baseline selection. The hatched area indicates the uncertainties from signal/background normalization (right).

Table 6.1: Simulated samples used for analysis.

Dataset name	σ [pb]	σ-calculation
$t\bar{t}$ signal (`Powheg` + `Pythia 8`)		
`TTJets inclusive`	831.76	NNLO+NNLL
`TTJets inclusive mtop1665`	982	NNLO+NNLL
`TTJets inclusive mtop1695`	903	NNLO+NNLL
`TTJets inclusive mtop1715`	855	NNLO+NNLL
`TTJets inclusive mtop1735`	809	NNLO+NNLL
`TTJets inclusive mtop1755`	767	NNLO+NNLL
`TTJets inclusive mtop1785`	708	NNLO+NNLL
$t\bar{t}$ systematic variations (`Powheg` + `Pythia 8`)		
`TTJets inclusive scaleup`	832	NNLO+NNLL
`TTJets inclusive scaledown`	832	NNLO+NNLL
$t\bar{t}$ systematic variations (`Powheg` + `Pythia 8`)		
`TTJets inclusive noCR`	832	NNLO+NNLL
`TTJets inclusive mpiOFF`	832	NNLO+NNLL
$t\bar{t}$ systematic variations (X+`Pythia 8`)		
`TTJets inclusive amc@nlo`	832	NNLO+NNLL
`TTJets inclusive amc@nloFXFX`	832	NNLO+NNLL
`TTJets inclusive madgraphMLM`	832	NNLO+NNLL

Continued on next page

Table 6.1 – continued from previous page

Dataset name	σ [pb]	σ-calculation
W/Z+jets background		
DYJetsToLL_M-10to50_amc@nloFXFX-pythia8	22635.09	NNLO
DYJetsToLL_M-50_madgraphMLM-pythia8	6025.2	NNLO
WJetsToLNu_amc@nloFXFX-pythia8	61526.7	NNLO
Single top background		
ST_tW_top_5f_inclusiveDecays_13TeV-powheg-pythia8	35.6	NNLO
ST_tW_antitop_5f_inclusiveDecays_13TeV-powheg-pythia8	35.6	NNLO
ST_t-channel_4f_leptonDecays_13TeV-amc@nlo-pythia8	70.69	approx. NNLO
ST_s-channel_4f_leptonDecays_13TeV-amc@nlo-pythia8	3.32	approx. NNLO
Diboson background (Pythia 8)		
WW	63.21	NLO
WZ	22.82	NLO
ZZ	10.32	NLO

Continued on next page

Table 6.1 – continued from previous page

Dataset name	σ [pb]	σ-calculation
QCD multijet background (madgraphMLM + Pythia 8)		
QCD_HT100to200	27540000	LO
QCD_HT200to300	1735000	LO
QCD_HT300to500	366800	LO
QCD_HT500to700	29370	LO
QCD_HT700to1000	6524	LO
QCD_HT1000to1500	103.0	LO
QCD_HT1500to2000	121.5	LO
QCD_HT2000toInf	25.42	LO
QCD_Pt-20to30_MuEnrichedPt5	2960198	LO
QCD_Pt-30to50_MuEnrichedPt5	1652471	LO
QCD_Pt-50to80_MuEnrichedPt5	437504	LO
QCD_Pt-80to120_MuEnrichedPt5	106034	LO
QCD_Pt-120to170_MuEnrichedPt5	25191	LO
QCD_Pt-170to300_MuEnrichedPt5	8655	LO
QCD_Pt-300to470_MuEnrichedPt5	797	LO
QCD_Pt-470to600_MuEnrichedPt5	79.0	LO
QCD_Pt-600to800_MuEnrichedPt5	25.1	LO
QCD_Pt-800to1000_MuEnrichedPt5	4.7	LO
QCD_Pt-1000toInf_MuEnrichedPt5	1.6	LO
QCD_Pt-15to20_EMEnriched	254600	LO
QCD_Pt-20to30_EMEnriched	5352960	LO

Continued on next page

Table 6.1 – continued from previous page

Dataset name	σ [pb]	σ-calculation
QCD_Pt-50to80_EMEnriched	2890800	LO
QCD_Pt-80to120_EMEnriched	350000	LO
QCD_Pt-120to170_EMEnriched	62964	LO
QCD_Pt-170to300_EMEnriched	18810	LO
QCD_Pt-300toInf_EMEnriched	1350	LO

6.2 Semi-leptonic selection

6.2.1 Trigger

The first step of the selection is to check if the event passed a high level trigger that roughly pre-identifies leptons. For muons the minimum trigger threshold on the transverse momentum of a muon is 20 GeV and the muon has to be isolated. .[4] Scale factors for the trigger, reconstruction, and selection efficiencies are applied. They were determined via the tag-and-probe method in $Z \to \ell^+\ell^-$. One of the leptons is required to fire the trigger with tight selection criteria and the invariant mass of the lepton pair has to be within a window of 15 GeV around the Z-boson mass. The efficiencies are determined by applying the selection and trigger criteria to the probe leptons and normalizing to their total number. The data-to-MC scale factors are the ratios of the efficiencies and depend on the lepton p_T and η. For muons they are shown in figure 6.2 and 6.3. The combined average scale-factor is 0.970 ± 0.001 stat. Details on this method can be found in CMS AN 2013/267 and reference [71].

6.2.2 Preselection

The following selection steps ensure that each event includes exactly one high energy lepton and at least four high energy jets, that do not overlap with the lepton. Selected muons have to fulfill the following conditions to be taken as signal muon:

- $p_T > 25$ GeV and $|\eta| < 2.1$
- PFMuon ID `tight`, that means:
  - reconstructed in both tracker and muon system (*global* muons)
  - valid hits in at least 5 tracker layers, at least 1 pixel layer, and in the muon system
  - $\chi^2/\text{ndf} < 10$ for global track fit
  - impact parameter with respect to beam spot $|dB| < 0.02$ cm
  - distance to the primary vertex in z direction smaller than 0.5 cm
- relative isolation $I(\Delta R = 0.4) < 0.15$

[4] The used trigger path is `HLT_IsoMu20_v*`

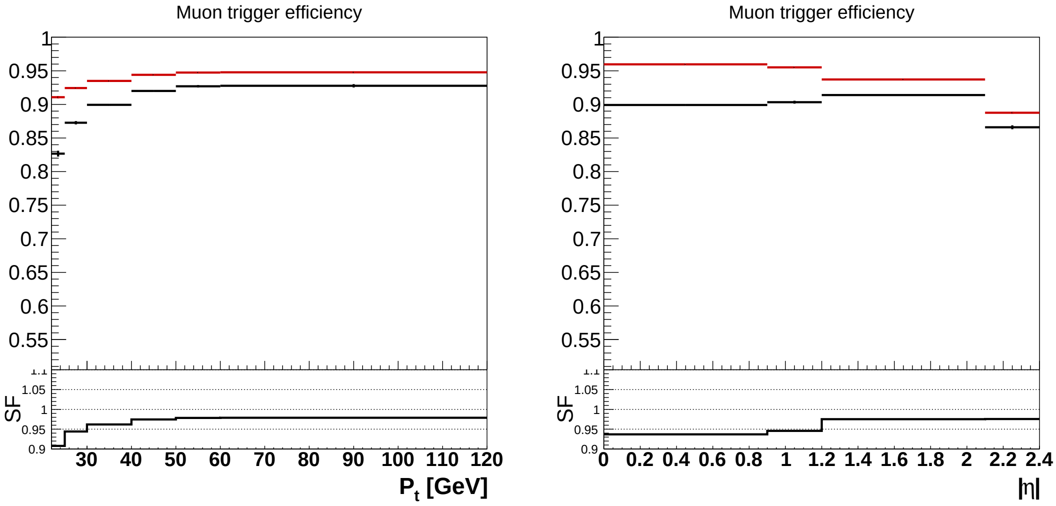

Figure 6.2: The single-muon trigger efficiencies for MC and data (upper part) and the corresponding scale factor (lower part) as a function of p_T (left) and η (right) of the lepton.more information can be found in

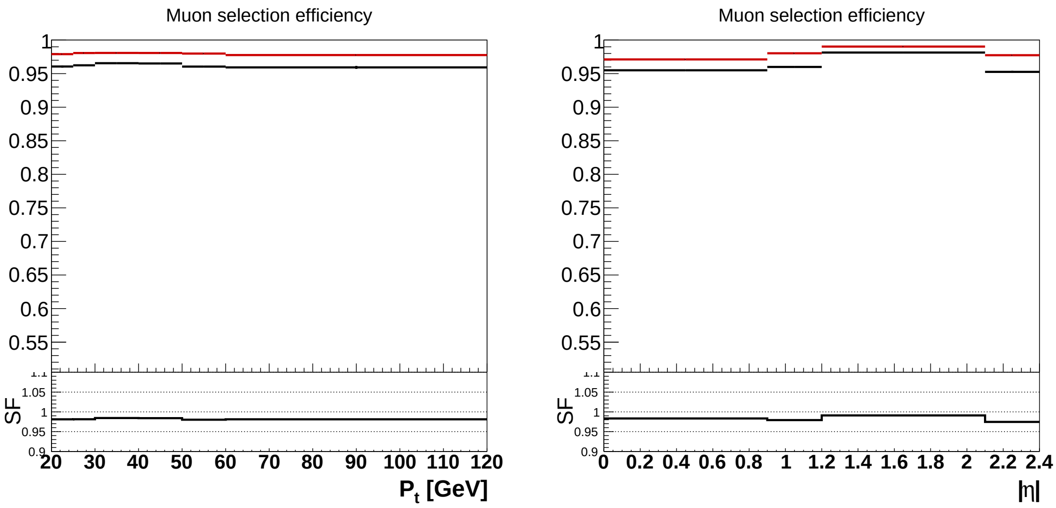

Figure 6.3: The muon selection efficiencies for MC and data (upper part) and the corresponding scale factor (lower part) as a function of p_T (left) and η (right) of the lepton.

Figure 6.2 and 6.3: Red markers denote MC and black markers denote data. The shown uncertainties are statistical only. The data was taken from `cmsdoc.cern.ch/cms/Physics/muon/ReferenceEfficiencies/Run2015/25ns/SingleMuonTrigger_Z_RunCD_Reco76X_Feb15.root`, more information can be found in `https://twiki.cern.ch/twiki/bin/viewauth/CMS/MuonReferenceEffsRun2`.

In order to suppress background contributions, events are not selected, if additional isolated leptons with the following properties are detected:

- *Global* muons with $p_T > 15\,\mathrm{GeV}$, $|\eta| < 2.4$, $I(\Delta R = 0.4) < 0.25$
- Electrons[5] with $p_T > 15\,\mathrm{GeV}$, $|\eta| < 2.4$, $I(\Delta R = 0.4) < 0.15$

Jets are clustered and calibrated as described in section 5.4. At least four jets with $p_T > 30\,\mathrm{GeV}$ and $|\eta| < 2.4$ are required. All selected jets are required to have a distance of $\Delta R > 0.3$ to the signal lepton.

The event yields of this selections can be found in table 6.2 in the column "pre". Out of the $2.2\,\mathrm{fb}^{-1}$ single muon data 112 732 events are selected. The $t\bar{t}$ signal fraction is expected to be above 60%. The p_T, η, and ϕ distributions of the muon and the muon/ anti-muon numbers are shown in figure 6.5. They are described by the simulation. The distribution of the MET and η-ϕ distance between selected muon and jets is shown in figure 6.4, again in agreement with the simulation. The plots include the uncertainties from the signal/background normalization and statistic limitations of the simulation samples.
The normalization uncertainties shown stem from theoretical uncertainties on the cross-sections. They are rounded up to 6.0% for $t\bar{t}$ signal, 10% for single top, 100% for QCD multijet, and 5% for diboson and W/Z+jets background.

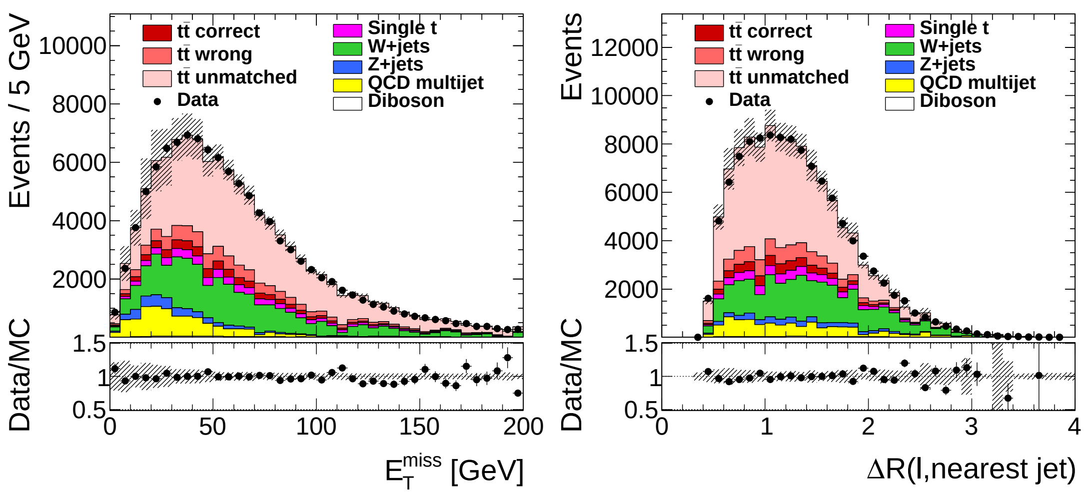

Figure 6.4: Preselection: Missing transverse momentum (left), and minimum distance between selected lepton and a jet with $p_T > 30\,\mathrm{GeV}$ (right).

[5] electronID = `mvaEleID-Spring15-25ns-Trig-V1-wp80`

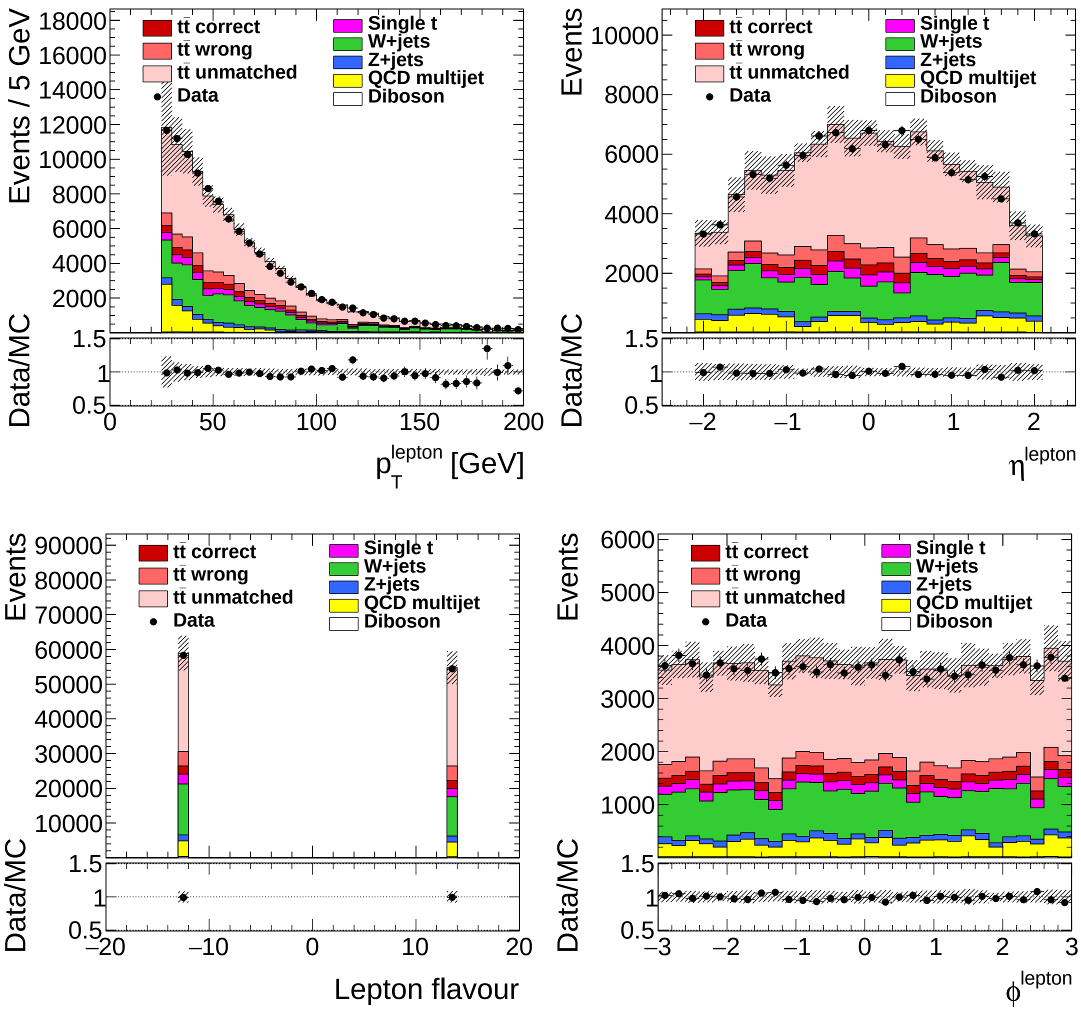

Figure 6.5: Preselection: Upper row: reconstructed lepton p_T (left) and η (right). Lower row: lepton flavour (left; $-13 = \mu^+, 13 = \mu^-$) and ϕ (right). The plots are normalized to luminosity. The hatched area indicates uncertainties from MC statistics and cross-sections.

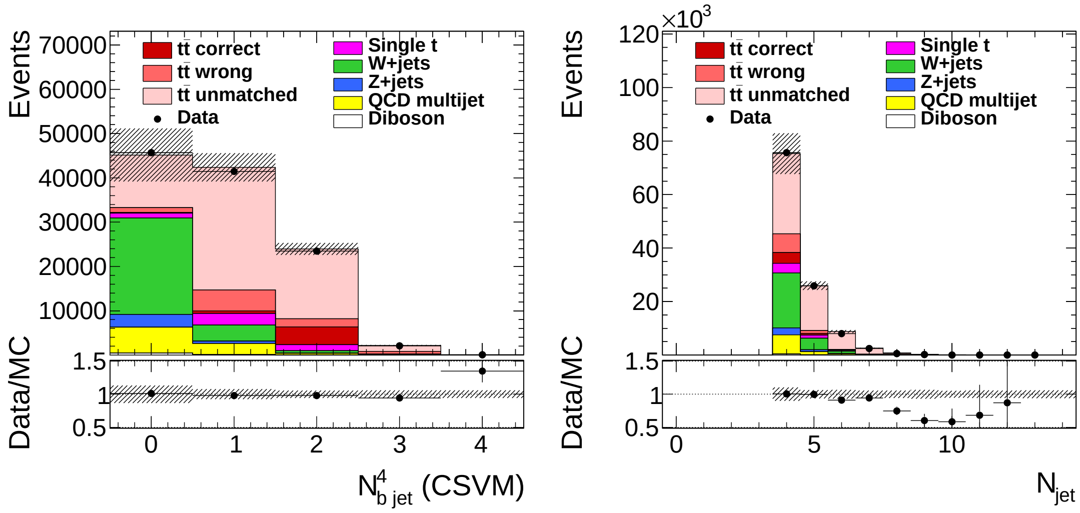

Figure 6.6: Preselection: Number of b-tags among four leading jets, $p_T > 30\,\text{GeV}$, (left), and number of jets with $p_T > 30\,\text{GeV}$.

6.2.3 Baseline Selection

The next selection step is based on the `CSVv2M` b-tagging algorithm, that has been introduced in section 5.4.3. It identifies jets originating from a b quark with a mis-tag rate of 1% and a efficiency of approximately 70%. Figure 6.6 shows the b-tagged jets among the four leading jets and the number of jets with $p_T > 30\,\text{GeV}$ before the b-tag selection. The discrepancies at very high jet multiplicities are expected due to the limitation of the theoretical method used and covered by shape uncertainties of the $t\bar{t}$ signal, as will be seen in figure 6.8.

At least two b-tagged jet with $p_T > 30\,\text{GeV}$ are required for the event to pass the selection. In the following kinematic fit, the number of b-tagged jets will be further constrained, to be exactly two among the four leading jets. For the b-tag efficiency correction a weight is derived and applied to the simulated events. It is $w = P(\text{DATA})/P(\text{MC})$ with

$$P(\text{MC}) = \prod_{i=\text{tagged}} \varepsilon_i \prod_{j=\text{not tagged}} (1-\varepsilon_j)$$

$$\text{and} \qquad P(\text{DATA}) = \prod_{i=\text{tagged}} \text{SF}_i\varepsilon_i \prod_{j=\text{not tagged}} (1-\text{SF}_j\varepsilon_j)\,,$$

where ε_i is the MC b-tagging efficiency and SF_i the data-to-simulation scale factor of the b-tagging efficiency, that can be found in figure 5.2 as SF_b. ε_i and SF_i are both functions of the jet flavor, p_{T}, and η. The indices i and j run over the four leading jets. [6]

Including the b-tag requirement, 29 406 $\mathrm{t\bar{t}}$ candidate events are selected in data. The estimated selection efficiency is 2.2%. From simulation, the event composition is expected to be $> 88\%$ $\mathrm{t\bar{t}}$ -signal, as shown in tabular 6.2 in the column "base".

The same control distributions, as for the preselection, are shown in figures 6.7 – 6.9. The transverse momenta of the four leading jets are shown in figure 6.10. with an uncertainty band that takes into account simulation statistics, cross-section normalization, pile-up, jet energy scale and resolution, renormalization and factorization scale of the event generation $\mu_{R,F}$, and top-p_T re-weighting uncertainties. Data and simulation agree well. The discrepancies in the number of jets for high number of jets and the jet-p_T distribution are within the uncertainties. The slope in the p_T distributions is expected from to observations in previous analysis. It is caused by the handling of additional jets in the MC generation.

[6] All weights in the context of b-tagging were given through personal correspondence by Nataliia Kovalchuk (nataliia.kovalchuk@desy.de).

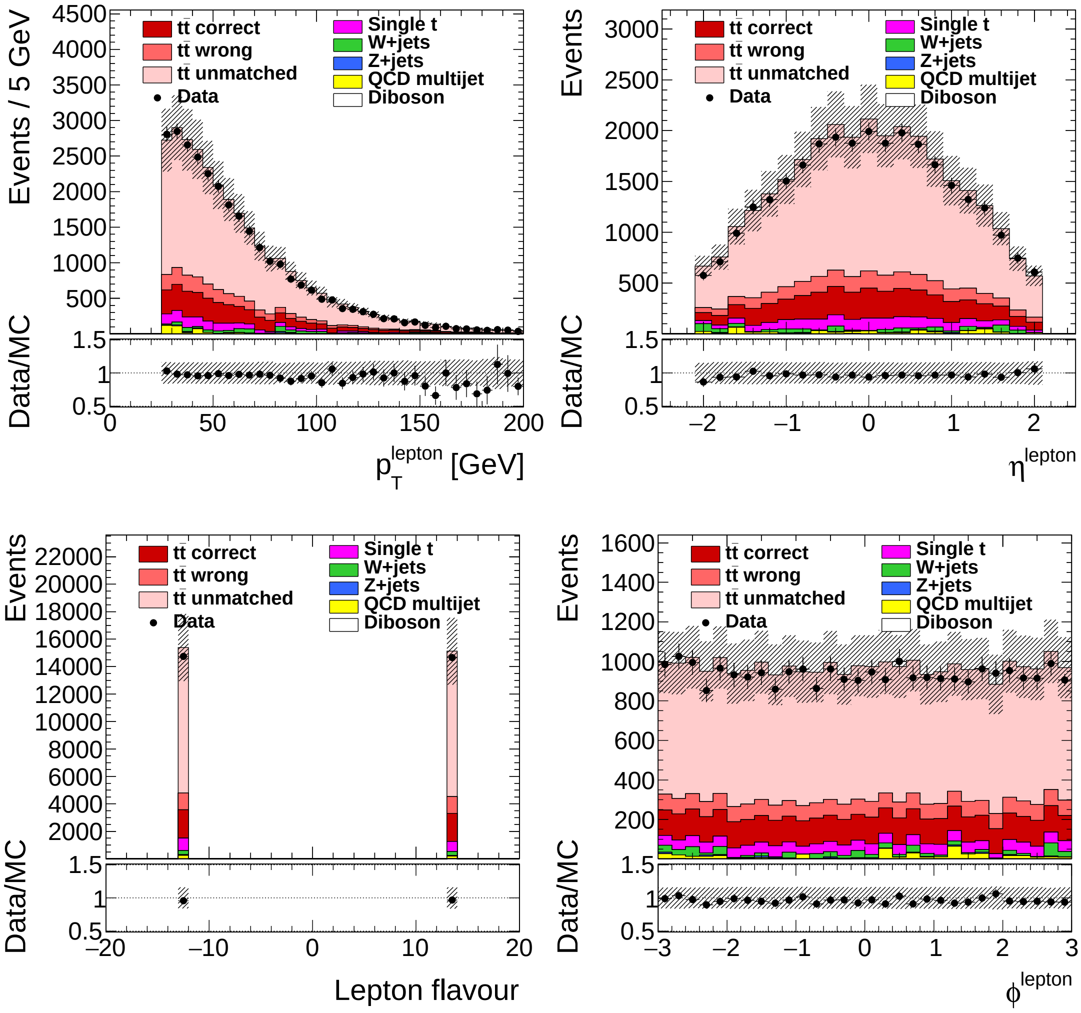

Figure 6.7: Baseline selection: Upper row: reconstructed lepton p_T (left) and η (right). Lower row: lepton flavour (left; $-13 = \mu^+, 13 = \mu^-$) and ϕ (right). The MC simulations are normalized to luminosity. The hatched area indicates uncertainties from MC statistics and cross-section.

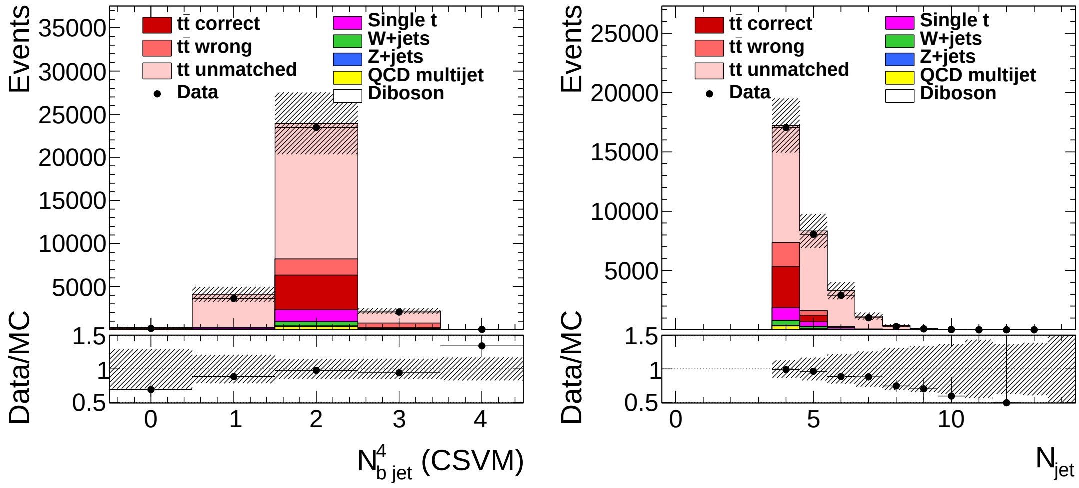

Figure 6.8: Baseline selection: Number of b-tags among four leading jets, $p_T > 30\,\text{GeV}$, (left), and number of jets with $p_T > 30\,\text{GeV}$.

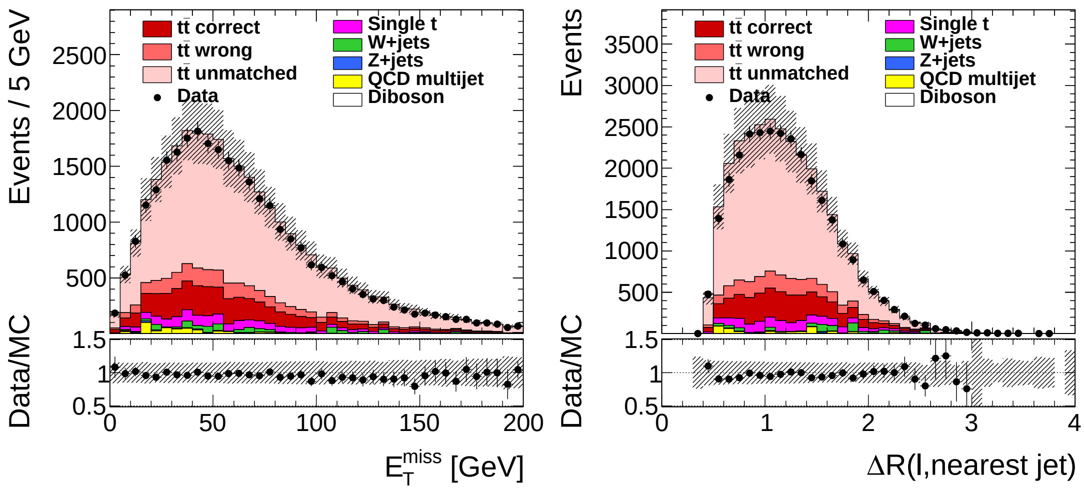

Figure 6.9: Baseline selection: Missing transverse momentum (left), and minimum distance between selected lepton and a jet with $p_T > 30\,\text{GeV}$ (right).

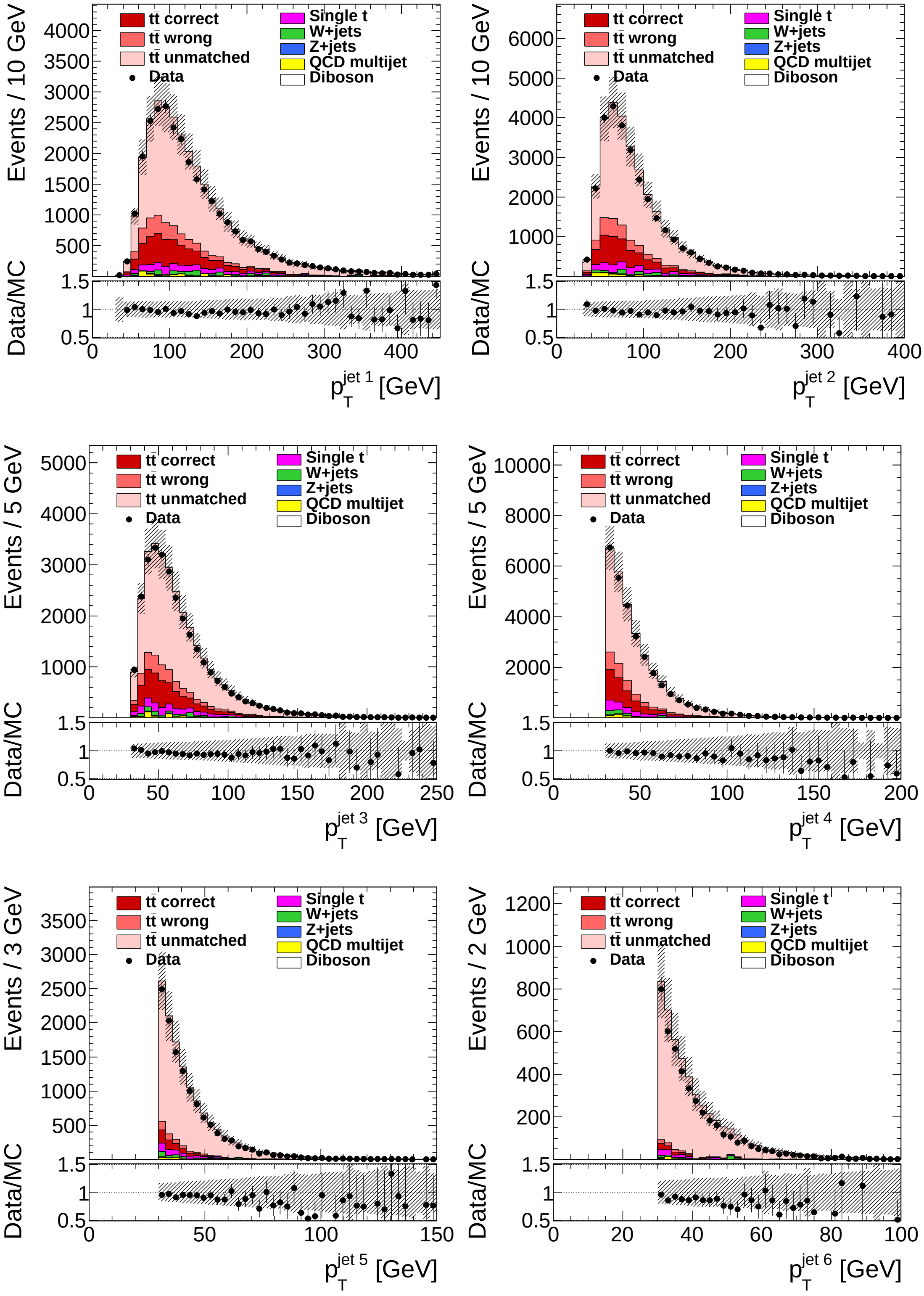

Figure 6.10: Baseline selection: Reconstructed transverse momenta of the six leading jets.

Table 6.2: Event yields and fractions for signal and background processes. The uncertainties arise from MC statistics and cross-section.

	pre (1 ℓ, 4 jets)			base (+ 2b, $\Delta R(\ell,\text{jet})$)			final (+ P_{gof})		
	events	$\pm$	[%]	events	$\pm$	[%]	events	$\pm$	[%]
$t\bar{t}$ +jets	69 742.5	3 047.6	61.4	27 749.7	1 303.8	90.9	5 709.1	212.7	95.9
Z+jets	3 487.1	210.5	3.1	96.5	21.1	0.3	11.2	6.1	0.2
W+jets	25 954.2	1 725.4	22.8	571.3	159.9	1.9	0.0	40.6	0.0
Single top	5 166.6	518.5	4.5	1 646.7	166.2	5.4	178.3	18.9	3.0
QCD multijet	8 712.6	8 734.4	7.7	429.8	444.9	1.4	53.5	75.2	0.9
Diboson	602.7	34.4	0.5	22.4	3.1	0.1	3.2	1.2	0.1
MC total	113 665.8	9 427.1	100	30 516.5	1 396.9	100	5 955.2	226.5	100
Data	112 732			29 406		–	5 798		

6.3 Mass reconstruction

The invariant mass of the top quarks in each event can be calculated out of the four-vectors, the energy and momentum, of their decay products. A $t\bar{t}$ hypothesis is built by taking two b-tagged jets as candidates for the bottom quarks and the other two of the leading four jets as candidates for one of the W bosons. This leads to two possible jet-parton assignments per event. Both are considered. The other W boson can be reconstructed out of the signal lepton and the MET, that is corresponding to the neutrino. The invariant mass of the systems of one W boson and its associated bottom quark is considered to be the invariant mass of the top quarks. In addition, the z-component of the neutrino momentum has to be estimated. There is a sign ambiguity for this, which doubles the number of possible permutations.
For simulated $t\bar{t}$ events the "true" jet-parton assignment is known, so the assignment of the reconstruction algorithm can be classified as

- *correct permutation* (cp): The four decay quarks have been matched to the four leading jets and the correct W-boson to bottom quark assignment to one of the top quarks were made.
- *wrong permutation* (wp): The correct jets are selected but the assignment to the partons is wrong, e.g. by flipped bottom jet assignment, not-tagging, or mis-tagging.
- *unmatched permutation* (up): At least one of the four leading jets can not be matched to a parton. This can be the case when jets are in the matching radius from each other or the parton decay was not within the detector acceptance.

The mass distributions for all permutations of the hadronic W boson and the associated top quark are shown in the upper plots of figure 6.12. It can be seen, that the shape of the correct permutations is approximately Gaussian around the true mass. The wrong and unmatched permutations have more contributions at higher masses.
Of course this classification is not possible for detector data. An optimization of the selection for correct permutation is helpful nonetheless. For the reconstructed mass the correct permutation hypothesis is expected to be closest to LO parton-level configuration.
In table 6.3 the fraction of the different permutations without further improvements is listed in the column "baseline".

6.4 Kinematic fit

For further improvement of the resolution of the observables and as an additional selection possibility for enhancing correct permutations, a kinematic fit is done. The fit is the same that was applied in the $\sqrt{s} = 7\,\text{TeV}$ and $\sqrt{s} = 8\,\text{TeV}$ analysis and at the DØ experiment [72–75]. It applies 26 constraints for 24 observables. The observables are the four-vectors of the four leading jets, the signal lepton, and the MET, interpreted as the neutrino. Technically only the part of the MET is used, that is not correlated to the other four-vectors. The resolution of these observables are taken into account.
The constrains of the fit are

- measured momentum of the four leading jets
- measured momentum of the signal lepton
- transverse momentum components of the neutrino as given by MET
- equal masses of top and anti-top quark, this neglects the top quark decay width and is correct for the average
- invariant W-boson mass exactly $m_\text{W} = 80.4\,\text{GeV}$. The uncertainty on this mass of 0.02% [76] is negligible.
- two massless light quarks (massless compared to the top quark)
- one massless signal lepton (massless compared to the top quark)
- invariant bottom quark mass exactly $m_\text{b} = 4.7\,\text{GeV}$
- invariant mass of the neutrino is zero,

which results in 2 degrees of freedom (ndf) for the fit.
The fit is executed by the `HitFit` [9] program. It minimizes $\chi^2 = (\mathbf{x} - \mathbf{x}^m)^T\, G\,(\mathbf{x} - \mathbf{x}^m)$ with the vector of measured observables $\mathbf{x}^m$, the vector of fitted observables $\mathbf{x}$, and the inverse error matrix G given by the resolutions of the observables. We define the goodness-of-fit (gof) probability for the fit as $P_\text{gof} = \exp\left(-\frac{1}{\text{ndf}}\chi^2\right) = \exp\left(-\frac{1}{2}\chi^2\right)$.

In figure 6.11 the χ^2 and P_gof of the kinematic fit, the fraction of combination types, and the signal-to-background performance for a cut on P_gof is shown. Most of the background events that are still left have low P_gof values. The peak of QCD-multijet background at $P_\text{gof} = 0.45$ is due to low statistics of this sample. The signal-to-background performance plot in the lower right displays the signal fraction $S/(S+B)$ and the signal significance $S/\sqrt{B}$, in dependence of a cut on P_{gof}, and the same weighted with P_{gof}. S is the number of correct permutations and B the number of wrong or unmatched permutations. As a compromise of suppression of background and not-correct permutations and keeping as much significance as possible

- $P_{\text{gof}} > 0.2$

is chosen as additional selection criteria to the baseline selection. In data this *final* selection yields 5 798 events with 14 327 permutations. The fraction of correct permutations observed in simulation is increased drastically from 12.8% to 43.8%. For the mass extraction, this will be improved further to 46%, by weighting the permutations with their goodness-of-fit probability. The three different permutation fractions for the baseline, final, and effective selection are listed in table 6.3. The estimated background and event yields for the final selection can be found in table 6.2. The non-$\text{t}\bar{\text{t}}$ background is reduced to 4%.
After this selection the W+Jets background yield is negative. This is possible because of the negative weights out of the `amc@NLO` generator. Therefore the W+Jets background in the final selection is assumed to be negligible. It is left out of all plots including this cut and the mass extraction.

Table 6.3: Permutation fractions for different signal classes.

	baseline	final $P_{\text{gof}} > 0.2$	effective $\times P_{\text{gof}}$
$\text{t}\bar{\text{t}}$ correct	14.8 %	43.8 %	46.1 %
$\text{t}\bar{\text{t}}$ wrong	8.9 %	22.3 %	22.1 %
$\text{t}\bar{\text{t}}$ unmatched	76.4 %	33.9 %	31.8 %

In the upper row of figure 6.12 the distributions in the reconstructed mass $m_{\text{W}^{\text{had}}}^{\text{reco}}$ and the mass $m_{\text{t}}^{\text{reco}}$ of the corresponding top quark are shown for all possible permutations before the kinematic fit. In the lower row of figure 6.12 the reconstructed W-boson mass $m_{\text{W}^{\text{had}}}^{\text{reco}}$ and the top-quark mass from the kinematic fit $m_{\text{t}}^{\text{fit}}$, after the P_{gof} selection, are shown. These two quantities will be the input for the top quark mass and jet scale factor extraction, that will be described in the following chapter. Here they are shown without the P_{gof} weight.

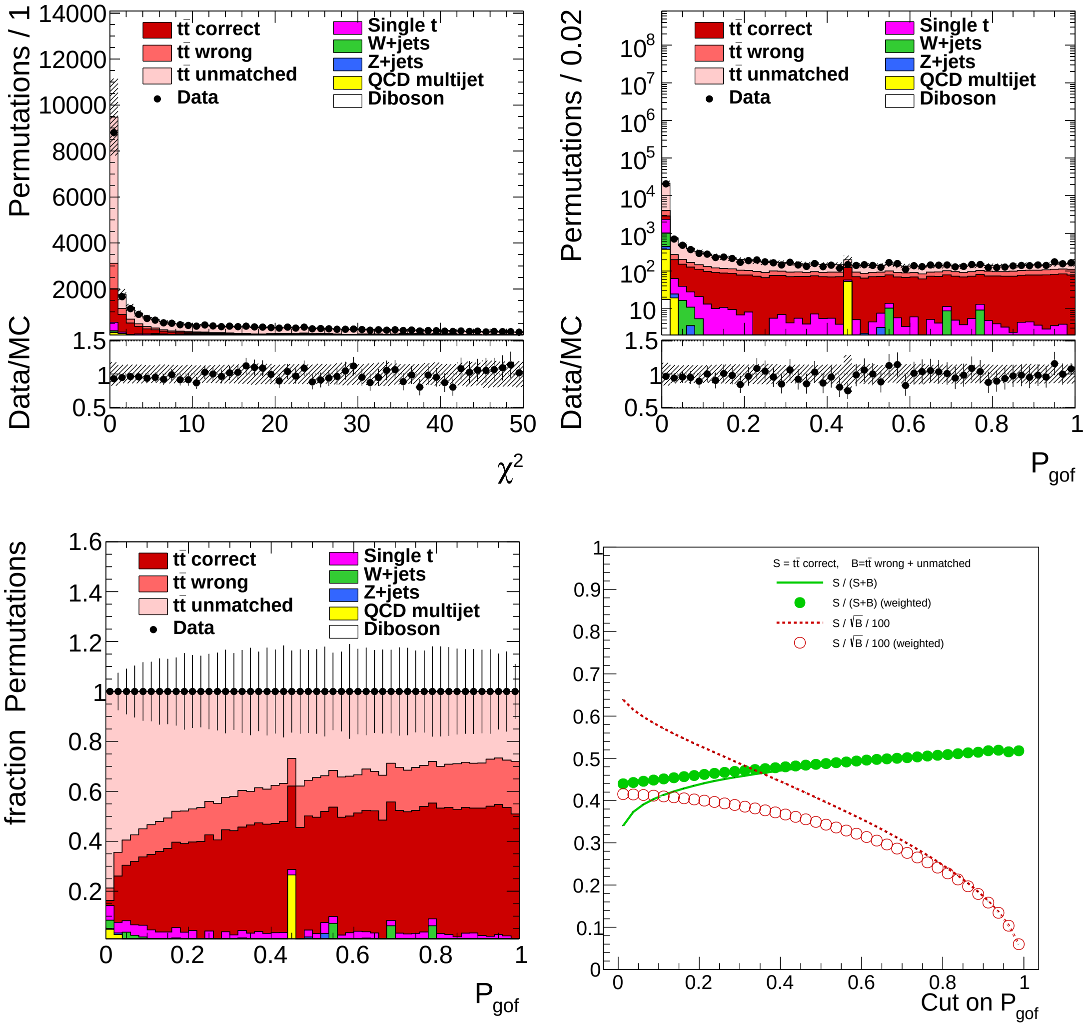

Figure 6.11: Baseline selection: χ^2 of the kinematic fit (upper left), goodness-of-fit probability P_{gof} (upper right), fraction of permutation types in dependency of P_{gof} (lower left), and signal-to-background performance for a cut on P_{gof} (lower right). The hatched area indicates uncertainties from MC statistics, cross-section, pile-up, jet energy scale and resolution, $\mu_{R,F}$, and top-p_T reweighting.

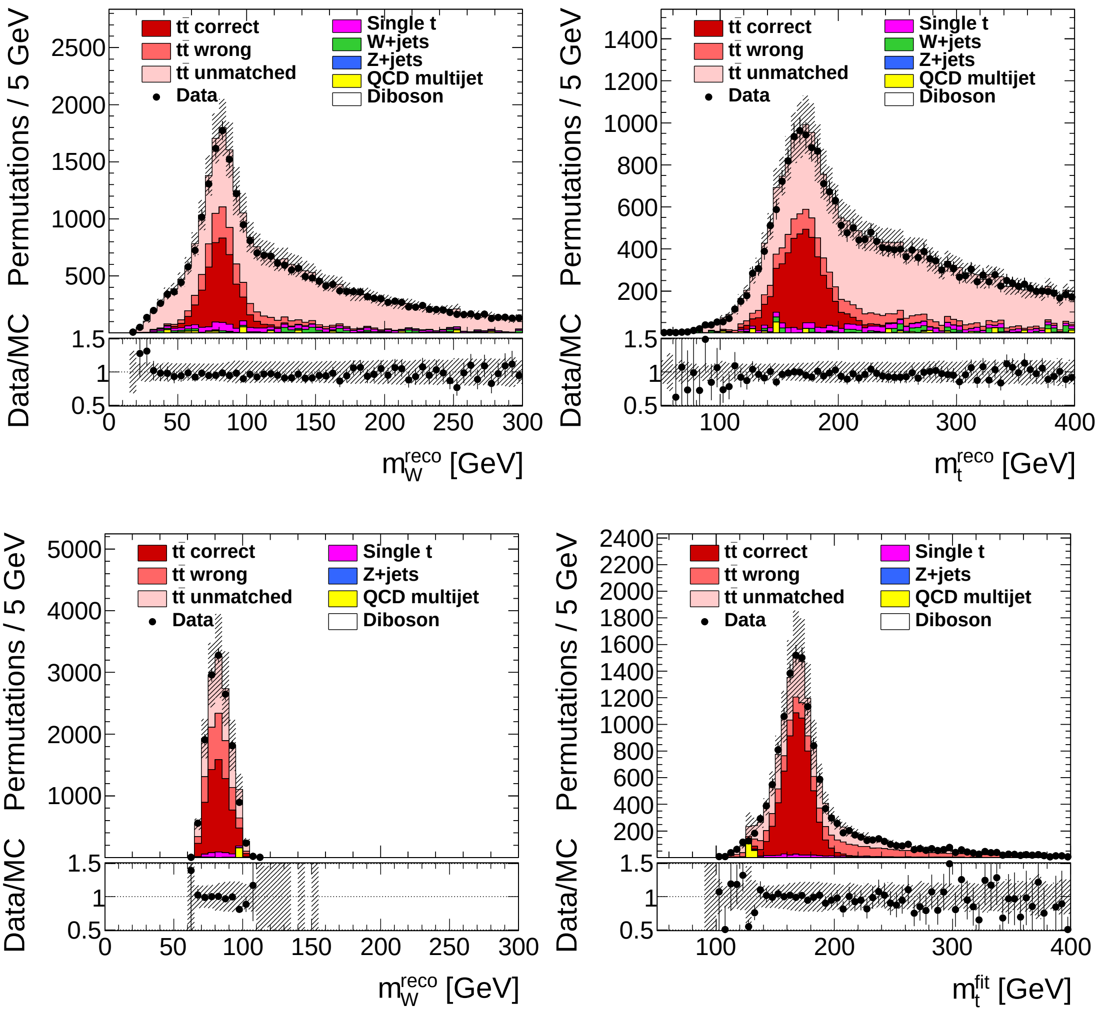

Figure 6.12: Final selection: Reconstructed masses of the W bosons decaying to quark-antiquark pairs (upper left) and the corresponding top quarks (upper right), prior to the kinematic fitting to the $t\bar{t}$ hypothesis. The lower plots show, respectively, the reconstructed W-boson masses and the fitted top-quark masses after the goodness-of-fit selection.

7 Methodology

In this analysis, the top quark mass will be determined from observables, that are highly correlated to it. The observable of choice is the invariant mass of the top quark products. With their distributions in simulated events with different generator top quark masses, templates are constructed. On these templates the data is fitted.
Previous analyses showed, that the top quark mass measurement is sensitive to the jet energy calibration. If the jet energy scale is known with an uncertainty of 2%, this translates to an uncertainty of about 2% on the top quark mass measurement. Due to the inclusion of the known W boson mass through the kinematic fit, $\pm 2\%$ on the jet energy scale will only result in $\pm 1.55\,\mathrm{GeV}$, that is $\pm 0.9\%$, uncertainty on the top quark mass measurement.
The way around this uncertainty is to determine a additional jet scale factor (JSF) simultaneously with the top quark mass in a joint likelihood fit. The JSF is extracted from the invariant W boson mass before the kinematic fit ($m_{\mathrm{W}}^{\mathrm{reco}}$). This method will be called "*2D approach*". A "*1D approach*" ,that determines m_{t} without use of the $m_{\mathrm{W}}^{\mathrm{reco}}$, is also done. Both measurements can be combined to a "*hybrid approach*". The $\sqrt{s} = 8\,\mathrm{TeV}$ measurement has shown that in the hybrid approach some of the systematic uncertainties can cancel each other out and a very precise result can be achieved [23].

7.1 Template fit method

The ideogram method, a specialized template fit method, has been used by the DELPHI Collaboration to measure the W-boson mass at the CERN LEP collider [77], at the Fermilab Tevatron collider, by the DØ Collaboration to measure the top quark mass in the lepton+jets channel [78], by the CDF Collaboration to measure the top-quark mass in the all-jet channel [79] and by the CMS Collaboration the measurement of the top-quark mass in the lepton+jets and all-jet channel [23,75,80].

A likelihood, in this context an unnormalized probability, is evaluated from analytic expressions. These expressions are derived from, and calibrated with, simulated events. With Bayes theorem the probability of the top-quark mass m_t and JSF in a data sample can be calculated as

$$P\left(m_\mathrm{t},\mathrm{JSF}|\mathrm{sample}\right) = P\left(\mathrm{sample}|m_\mathrm{t}\mathrm{JSF}\right) \times \frac{P\left(m_\mathrm{t}\right)P\left(\mathrm{JSF}\right)}{P\left(\mathrm{sample}\right)}\ , \tag{7.1}$$

where the second factor is just constant for the 2D approach, because no prior knowledge of m_t and JSF is included. For the 1D approach, the JSF is fixed to unity and $P\left(\mathrm{JSF}\right)$ becomes simple $\delta(1)$. In the hybrid approach, prior knowledge of the JSF is included by assuming $P\left(\mathrm{JSF}\right)$ to be Gaussian around 1 with a width of σ^c_JSF. The relative weight, with which the 1D result is combined with the 2D result, is then

$$w^\mathrm{1D}_\mathrm{hyb} = \left(\sigma^\mathrm{2D}_\mathrm{JSF}\right)^2 / \left\{\left(\sigma^\mathrm{2D}_\mathrm{JSF}\right)^2 + \left(\sigma^\mathrm{c}_\mathrm{JSF}\right)^2\right\}\ ,$$

with the statistical uncertainty of the JSF measurement in the 2D approach $\sigma^\mathrm{2D}_\mathrm{JSF}$. For the hybrid approach in this thesis $w^\mathrm{1D}_\mathrm{hyb} = 0.5$ will be used.

The right hand side of equation (7.1) becomes the likelihood

$$\mathscr{L}\left(\mathrm{sample}|m_\mathrm{t},\mathrm{JSF}\right) = \prod_\mathrm{events} \mathscr{L}\left(\mathrm{event}|m_\mathrm{t},\mathrm{JSF}\right)^{w_\mathrm{event}} \tag{7.2a}$$

$$= \prod_\mathrm{events} \left(\sum_{i=1}^{n} c\,P_\mathrm{gof}\left(i\right) P\left(m^\mathrm{fit}_{\mathrm{t},i}, m^\mathrm{reco}_{\mathrm{W},i}|m_\mathrm{t},\mathrm{JSF}\right)\right)^{w_\mathrm{event}}\ , \tag{7.2b}$$

where m_t and JSF are the parameters to be determined, n denotes to the number of permutations in each event, and c is the normalization constant. The contributions from background are not included in this expression, as the impact of background is found to be negligible after implementing the final selections, described in section 6.4. The ad hoc event weight $w_\mathrm{event} = \sum_{i=1}^{n} c\,P_\mathrm{gof}\left(i\right)$ reduces the impact of events without correct permutations. The sum of all event weights is normalized to the total number of events with

$$c = N_\mathrm{events} / \sum_\mathrm{events}\sum_{i=1}^{n} P_\mathrm{gof}(i),\ P_\mathrm{gof}(i) > 0.2\ .$$

The product of event likelihoods in equation (7.2a) is illustrated in figure 7.1. Likelihood planes

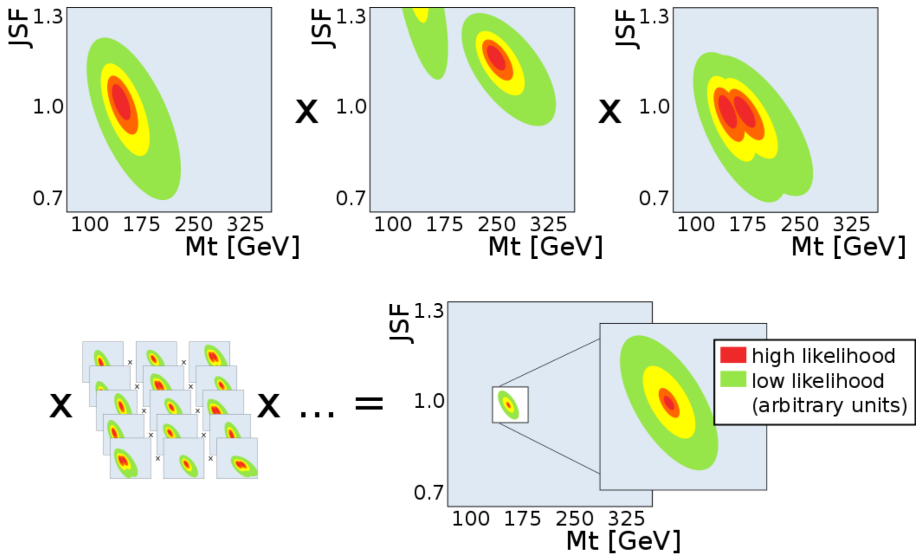

Figure 7.1: Illustration of the multiplication of the event likelihoods $\mathscr{L}(\text{event}|m_\text{t},\text{JSF})$ for several events to a sample likelihood $\mathscr{L}(\text{sample}|m_\text{t},\text{JSF})$. The z-axis has arbitrary units. Illustration by [23].

in (m_t,JSF) for a single event can include multiple solutions and have a relatively wide distribution. The multiplication of many of such likelihoods leads to a sample likelihood with one very distinct extremum.

The event likelihoods $\mathscr{L}(\text{event}|m_\text{t},\text{JSF})$ are given by the sum of the permutation probability densities $P\left(m_{\text{t},i}^{\text{fit}}, m_{\text{W},i}^{\text{reco}}|m_\text{t},\text{JSF}\right)$, weighted by the goodness-of-fit probability P_gof, as shown in equation (7.2b). When m_t^fit and m_W^reco can be treated as uncorrelated, the permutation probability densities can be factorized for the three different permutation types into

$$P\left(m_{\text{t},i}^{\text{fit}}, m_{\text{W},i}^{\text{reco}}|m_\text{t},\text{JSF}\right) = \sum_j f_j P_j\left(m_{\text{t},i}^{\text{fit}}|m_\text{t},\text{JSF}\right) \times P_j\left(m_{\text{W},i}^{\text{reco}}|m_\text{t},\text{JSF}\right), \quad (7.3)$$

with j representing *cp*, *wp* or *un* and their relative fractions f_j. f_j is taken from the simulated $\text{t}\bar{\text{t}}$ signal sample with the default top quark mass $m_\text{t}^\text{gen} = 172.5\,\text{GeV}$ and JSF=1. The correlation between m_t^fit and m_W^reco in the simulation samples that were used is $|\rho| < 1.5\%$.
The probability density functions P_j are derived from the simulated $\text{t}\bar{\text{t}}$ signal sample generated for the seven top quark generator mass m_t^gen values 166.5 GeV, 169.5 GeV, 171.5 GeV, 172.5 Gev, 173.5 GeV, 175.5 GeV, and 178.5 GeV that were stated in table 6.1 and the five JSF values 0.96, 0.98, 1.00, 1.02, and 1.04. For every (m_t^gen, JSF, permutation type) combination the weighted m_t^fit and m_W^reco distributions are fitted.

The distributions of the W boson mass are shown in figure 7.2 for different permutations, m_t^{gen}, and JSF values. The distributions are distorted by the P_{gof} selection and weight, they are not fitted with a Gaussian, but with a asymmetric Gaussian function

$$AG(x,\mu,\sigma_l,\sigma_r) = \begin{cases} \frac{1}{\sigma_l\sqrt{2\pi}} \cdot \exp\left(\frac{(x-\mu)^2}{2\sigma_l^2}\right) & \text{, for } (x-\mu) < 0 \\ \frac{1}{\sigma_r\sqrt{2\pi}} \cdot \exp\left(\frac{(x-\mu)^2}{2\sigma_r^2}\right) & \text{, for } (x-\mu) > 0 \end{cases}$$

with the mean μ and the left/right resolution $\sigma_{l,r}$.

In figure 7.4, μ and σ_l are shown for all seven m_t^{gen} and five JSF values for the correct permutations in dependence of the JSF. For every generator mass, the parameters of the AG fits are then fitted with linear functions of (JSF-1), that is drawn into the diagrams in figure 7.4. The fit results for $m_t^{gen} = 166.5\,\text{GeV}$ and $m_t^{gen} = 117.5\,\text{GeV}$ show an offset compared to the five other samples. This is even more visible on the left side of figure 7.3. There the offset of the linear (JSF-1) fit of μ (upper row) and σ_l (lower row) for the seven m_t^{gen} samples are displayed for correct permutations. The red lines are linear fits of ($m_t^{gen} - 172.5\,\text{GeV}$).
A dependence of the JSF on the top quark mass is not expected and the factorization of $P\left(m_{t,i}^{fit}, m_{W,i}^{reco}|m_t,\text{JSF}\right)$ would not work in this case. This offset could not be reproduced in the electron channel and not with the simulated events for 2016 data in `CMSSW 8.0.x` [1]. Therefore the $m_t^{gen} = 166.5\,\text{GeV}$ and $m_t^{gen} = 117.5\,\text{GeV}$ samples will not be used. This changes the linear ($m_t^{gen} - 172.5\,\text{GeV}$) fits of the JSF templates, as is shown in figure 7.3.

The parameters from the linear ($m_t^{gen} - 172.5\,\text{GeV}$) and (JSF-1) fits, on the parameters of the fit of AG on the m_W^{reco} distributions, can be identified with the $P_{cp}\left(m_{W,i}^{reco}|m_t,\text{JSF}\right)$ term in equation (7.3). The m_W^{reco} distribution for wrong and unmatched permutations are handled in the same way.

[1] The statement about the `CMSSW 8` samples were given through personal correspondence by Nataliia Kovalchuk (`nataliia.kovalchuk@desy.de`).

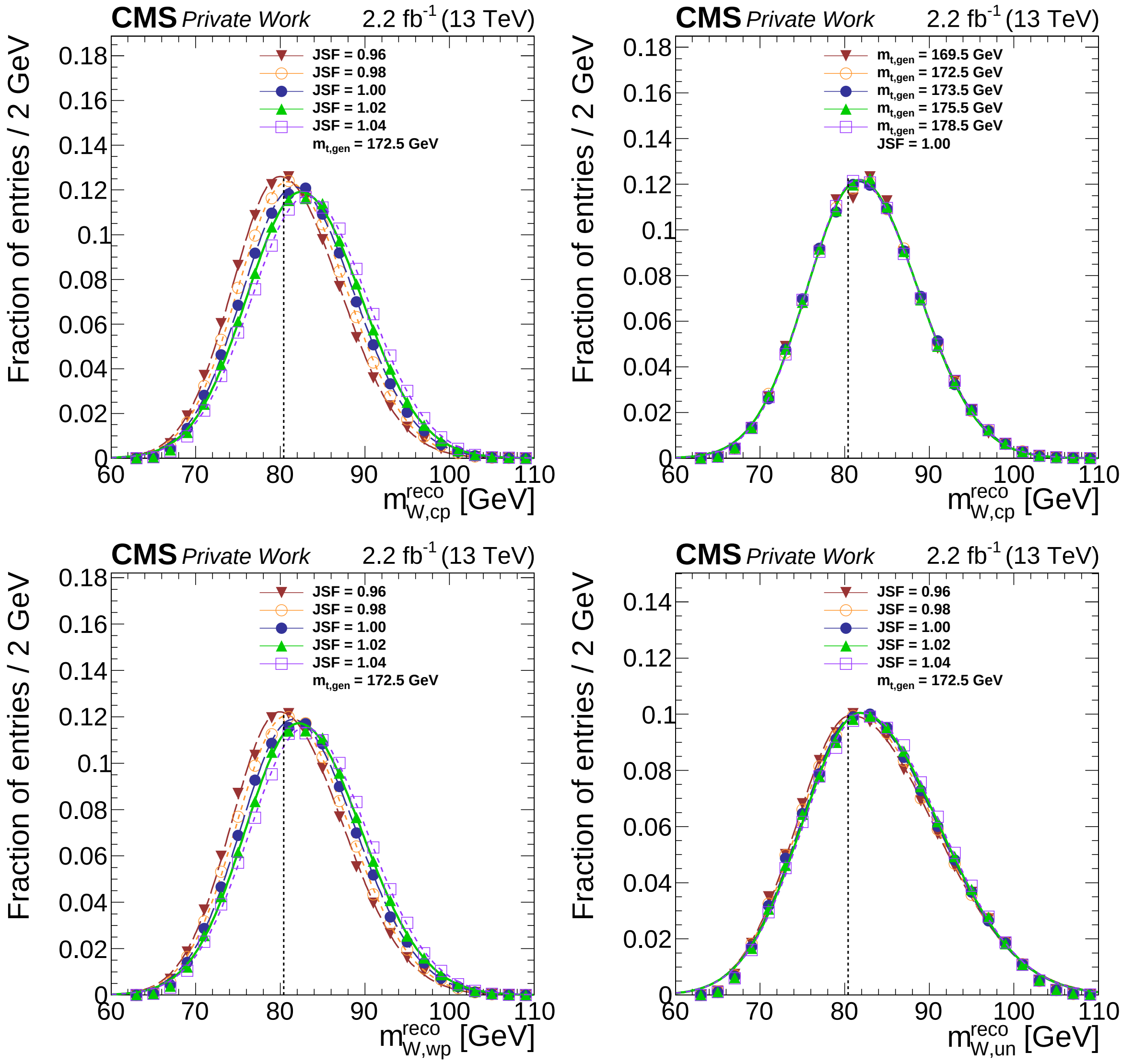

Figure 7.2: The $m_{\mathrm{W}}^{\mathrm{reco}}$ distributions are shown for correct (upper row), wrong (lower left), and unmatched (lower right) $\mathrm{t\bar{t}}$ permutations for five $m_{\mathrm{t}}^{\mathrm{gen}}$ values with JSF=1 (upper right) and for five jet scale factors with $m_{\mathrm{t}}^{\mathrm{gen}} = 172.5\,\mathrm{GeV}$ (other). The vertical dashed lines indicate the accepted value of the W-boson mass of 80.4 GeV . All distributions are shown for the muon+jets channel.

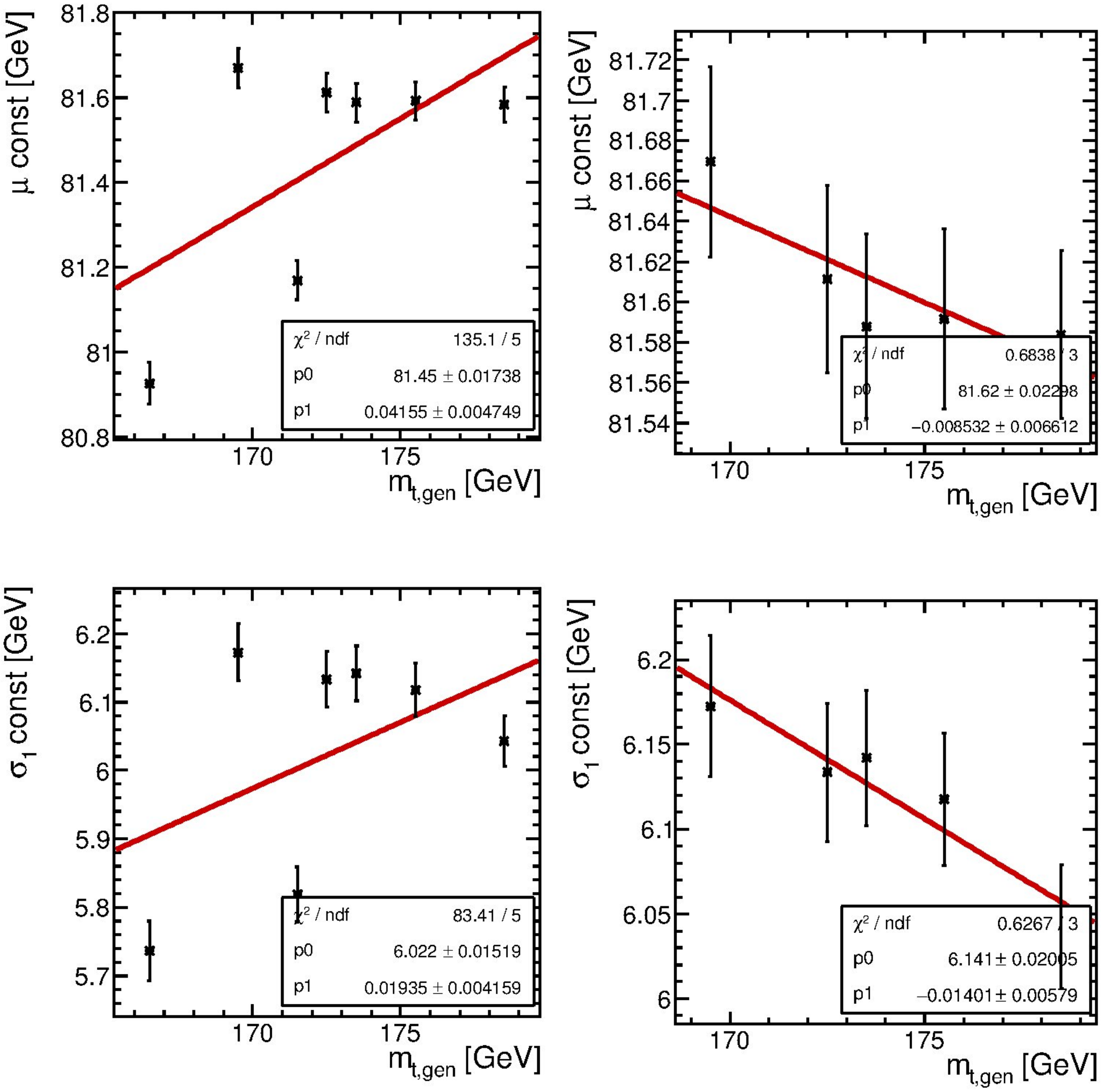

Figure 7.3: The offsets of the linear fit of (JSF-1) on the mean (upper row) and Gaussian resolution (lower row) of the asymmetric Gaussian fit of the $m_{\mathrm{W}}^{\mathrm{reco}}$ distributions for five $m_{\mathrm{t}}^{\mathrm{gen}}$ values for correct permutations. For all seven available $m_{\mathrm{t}}^{\mathrm{gen}}$ samples (left) and only the five samples that are used (right).

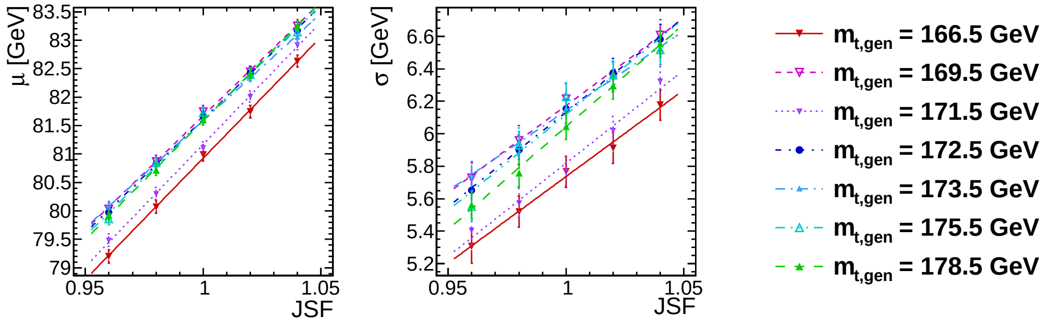

Figure 7.4: The mean and left resolution of the fit of the $m_{\mathrm{W}}^{\mathrm{reco}}$ distributions for seven $m_{\mathrm{t}}^{\mathrm{gen}}$ and five JSF values in dependence of the JSF for correct permutations.

The $m_{\mathrm{t}}^{\mathrm{fit}}$ distributions for correct permutations are fitted by a Voigt distribution

$$\begin{aligned} V(x,\mu,\sigma,\Gamma) &= \int dx' BW(x',\mu,\Gamma) \times G(x,x',\sigma) \,, \\ \text{with } BW(x,\mu,\Gamma) &= \frac{1}{2\pi} \cdot \frac{\Gamma}{\left((x-\mu)^2 + \frac{\Gamma^2}{4}\right)} \\ \text{and } G(x,\mu,\sigma) &= \frac{1}{\sigma\sqrt{2\pi}} \cdot \exp\left(\frac{(x-\mu)^2}{2\sigma^2}\right) \,, \end{aligned}$$

which is a Breit-Wigner distribution convolved with a Gaussian function, in dependence of the mean μ, the Gaussian resolution σ, and the width Γ, that is fixed to 2 GeV.
In figure 7.5 the fitted distributions for the five used generated masses $m_{\mathrm{t}}^{\mathrm{gen}}$ with $\mathrm{JSF} = 1$ and for the five used jet scale factor values with $m_{\mathrm{t}}^{\mathrm{gen}} = 172.5\,\mathrm{GeV}$ are shown.

The same linear fits as for the $m_{\mathrm{W}}^{\mathrm{reco}}$ templates are done. All parameters of the Voigt function are fitted first linearly in (JSF-1), which is shown is figure 7.6. The two parameters of the JSF are then fitted linearly in ($m_{\mathrm{t}}^{\mathrm{gen}} - 172.5$). This is displayed in figure 7.7. Again the result can be identified with the $P_{cp}\left(m_{\mathrm{t},i}^{\mathrm{fit}}|m_{\mathrm{t}},\mathrm{JSF}\right)$ term in equation (7.3).

For the wrong and unmatched permutations the $m_{\mathrm{t}}^{\mathrm{fit}}$ distributions are parametrized as crystal-ball functions

$$C(x,\mu,\sigma,\alpha,n) = N \cdot \begin{cases} \exp\left(-\frac{(x-\mu)^2}{2\sigma^2}\right) & ,\text{ for } \frac{x-\mu}{\sigma} > -\alpha \\ \left(\frac{n}{|\alpha|}\right)^n \cdot \exp\left(-\frac{|\alpha|^2}{2}\right) \cdot \left(\frac{n}{|\alpha|} - |\alpha| - \frac{x-\mu}{\sigma}\right)^{-n} & ,\text{ for } \frac{x-\mu}{\sigma} \leqq -\alpha \end{cases}$$

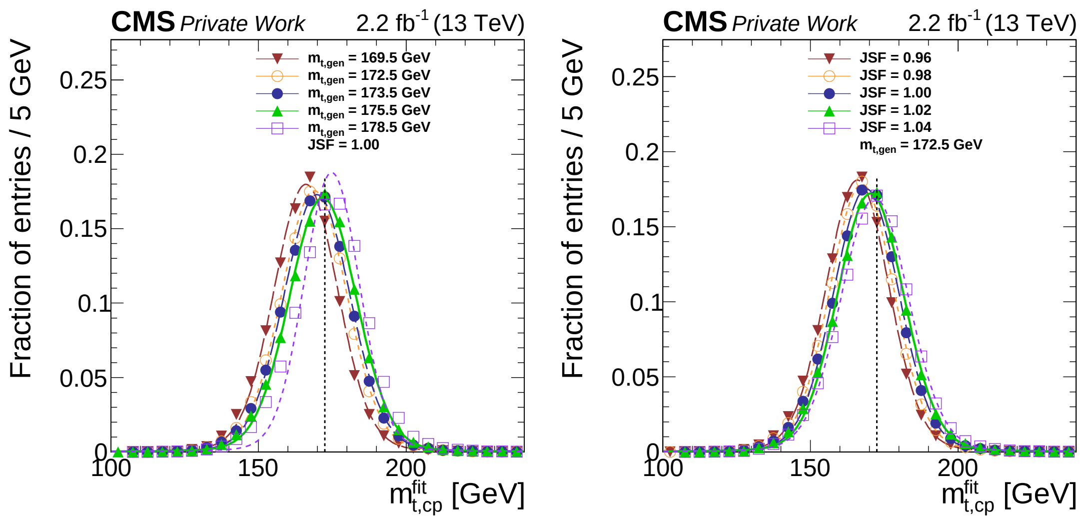

Figure 7.5: Simulated $m_{\mathrm{t}}^{\mathrm{fit}}$ distributions of correct $\mathrm{t\bar{t}}$ permutations, for five generator masses $m_{\mathrm{t}}^{\mathrm{gen}}$ with JSF $= 1$ (left) and for five jet scale factors with $m_{\mathrm{t}}^{\mathrm{gen}} = 172.5\,\mathrm{GeV}$ (right). The vertical dashed line corresponds to $m_{\mathrm{t}}^{\mathrm{fit}} = 172.5\,\mathrm{GeV}$.

with Gaussian mean μ and resolution σ and the exponential threshold α. The exponent n is fixed to 15 for wrong permutations and to 3 for unmatched permutations.

Some example distribution for wrong permutation are shown in figure 7.8 and for unmatched permutations in figure 7.9. The two linear fits in (JSF-1) and $(m_{\mathrm{t}}^{\mathrm{gen}} - 172.5)$ are done as before.

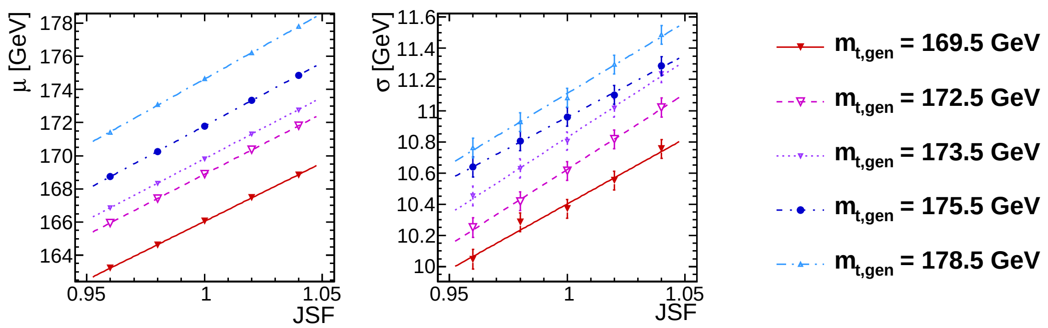

Figure 7.6: The mean and Gaussian resolution of the fit of the $m_{\mathrm{t}}^{\mathrm{fit}}$ distributions for five $m_{\mathrm{t}}^{\mathrm{gen}}$ and five JSF values in dependence of the JSF for correct permutations.

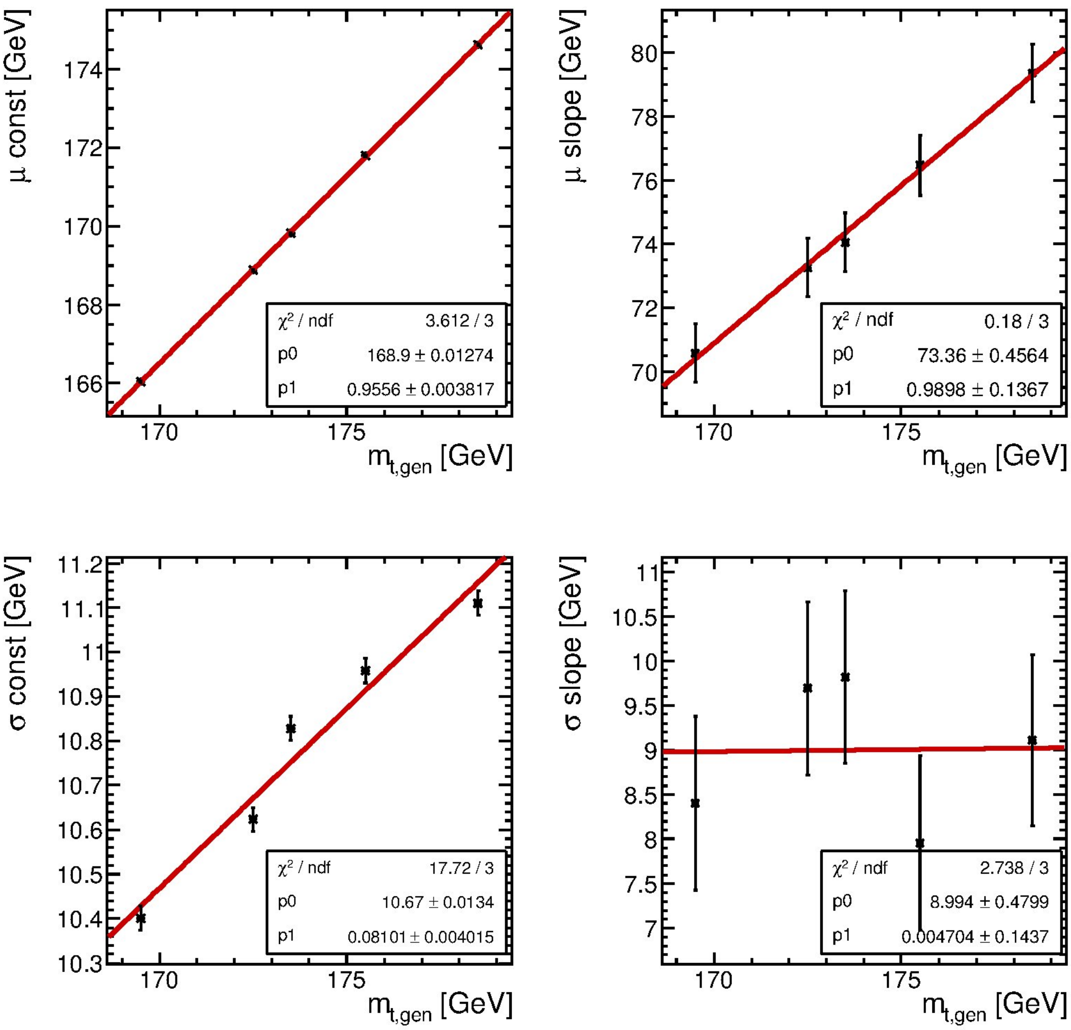

Figure 7.7: The offsets (right) and slopes (left) of the linear fit of (JSF-1) on the mean (upper row) and Gaussian resolution (lower row) of the Voigt fit of the $m_{\mathrm{t}}^{\mathrm{fit}}$ distributions for five $m_{\mathrm{t}}^{\mathrm{gen}}$ values for correct permutations.

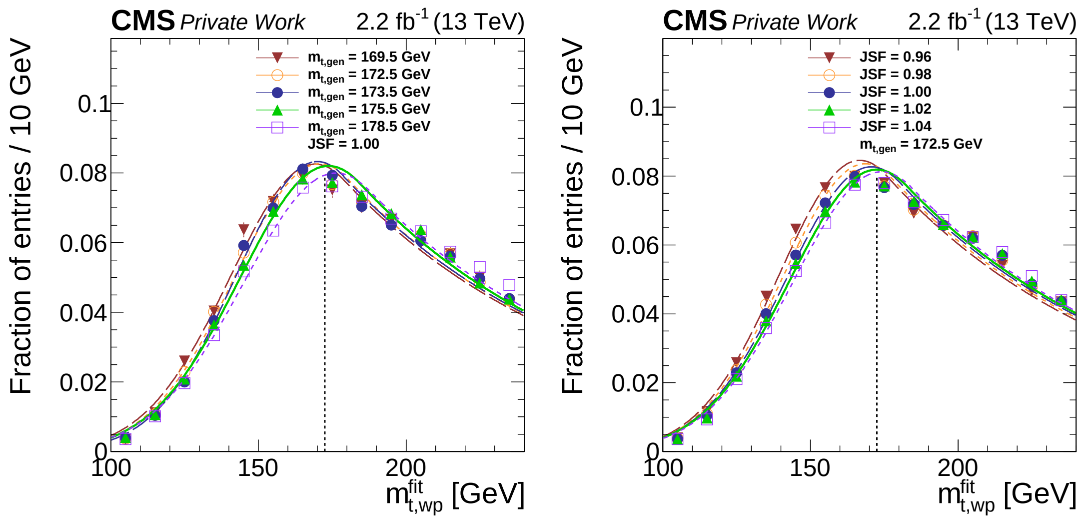

Figure 7.8: Simulated m_t^{fit} distributions of wrong $t\bar{t}$ permutations, for five generator masses m_t^{gen} with JSF = 1 (left) and for five jet scale factors with $m_t^{gen} = 172.5$ GeV (right). The vertical dashed line corresponds to $m_t^{fit} = 172.5$ GeV .

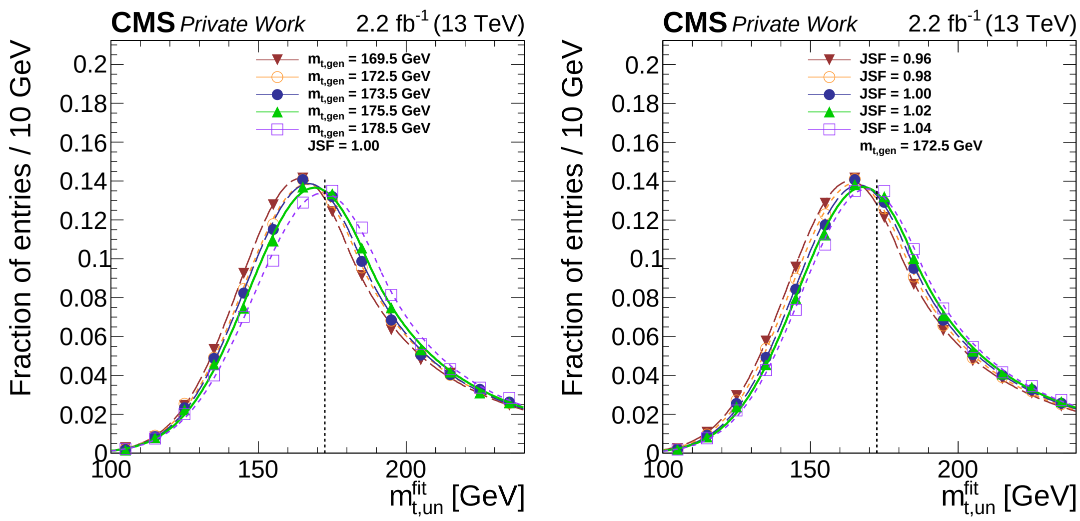

Figure 7.9: Simulated m_t^{fit} distributions of unmatched $t\bar{t}$ permutations, for five generator masses m_t^{gen} with JSF = 1 (left) and for five jet scale factors with $m_t^{gen} = 172.5$ GeV (right). The vertical dashed line corresponds to $m_t^{fit} = 172.5$ GeV .

7.2 Calibration

Some simplifications had to be made in the template method, for example, the fixed permutation fraction and neglection of possible background. Therefor the templates will be checked for biases and the correct estimation of the statistical uncertainty.
The calibration is done for the 2D approach and is also valid for the 1D and hybrid approach, as they are just special cases. For the calibration, for each of the 5×5 (m_t, JSF) phase-space points over 30 000 pseudo-experiments are done. Each pseudo-experiment is corresponding to one hypothetical data set of this analysis on $2.2\,\mathrm{fb}^{-1}$ of uncorrelated data.
The pseudo-experiments are done with unweighted sub-samples of randomized drawn events, out of the merged sample of N signal and background events. The events are normalized to luminosity and have the maximum MC event-weight w_{MCmax}. The following steps are repeated until the required number of event for one pseudo-experiment is reached:

- Select a random event out of the N events.
- Draw a random (floating point) number between the minimal MC event-weight (typically zero) and w_{MCmax}. Keep the selected event if its MC event-weight is larger than the drawn number.
- Increase the counter of drawn events, if the MC event-weight of the selected event is positive, decrease the counter if the event is negative. (possible for i.g. `amc@NLO` samples)

This sub-sample is then fitted to the templates derived in the last section. This results in one extracted value for the top quark mass $m_{\mathrm{t,extr}}$ and one for the jet scale factor $\mathrm{JSF}_{\mathrm{extr}}$ for each pseudo-experiment. $m_{\mathrm{t,extr}}$ and $\mathrm{JSF}_{\mathrm{extr}}$ follow Gaussian distributions, with the generator value as mean and the expected statistical uncertainty of the method as width. This distribution can be seen in figure 7.10. The different numbers of pseudo-experiments for different input values stem from the limit on the processing time, that was used instead of a limit on the number of pseudo-experiments. Expected statistical uncertainties of 0.45 GeV for m_t and 0.004 or JSF in the 2D approach and 0.28 GeV for m_t in the 1D approach are found.

For the calibration, background samples are not included.

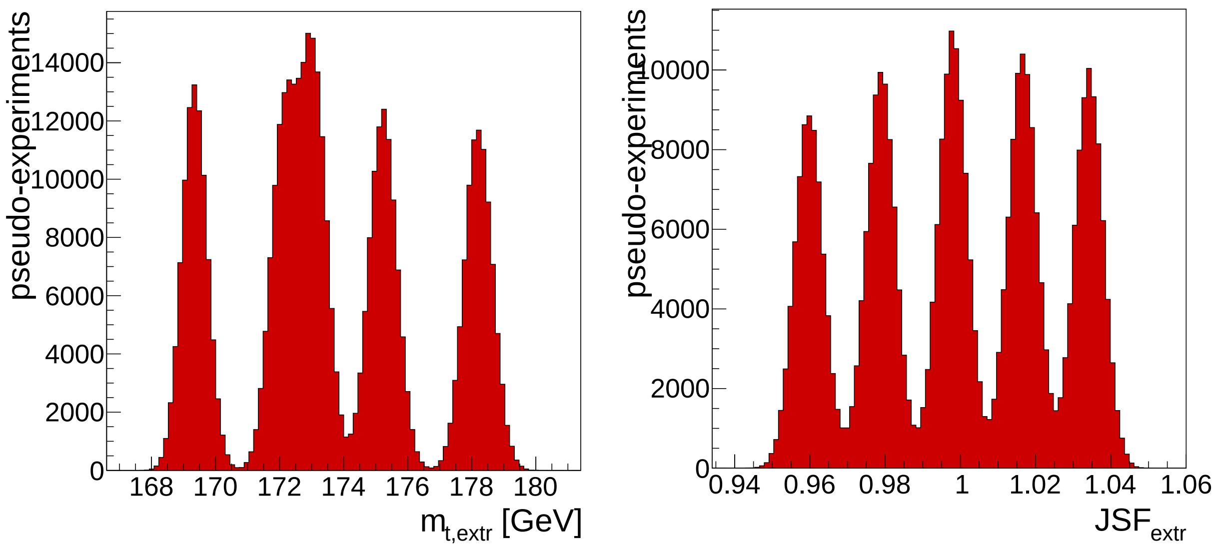

Figure 7.10: The extracted values out of the pseudo-experiments: $m_{t,\text{extr}}$ for different $m_{t,\text{gen}}$ and JSF=1 (left) and JSF_{extr} for different JSF and $m_{t,\text{gen}} = 172.5\,\text{GeV}$ (right).

For the calibration biases are defined as

$$\begin{aligned} \text{mass bias} &= \left\langle m_{\text{t,extr}} - m_{\text{t,gen}} \right\rangle , \\ \text{JSF bias} &= \left\langle \text{JSF}_{\text{extr}} - \text{JSF} \right\rangle . \end{aligned}$$

They are shown in the left part of figure 7.12 for the mass and the JSF, as a function of $m_{\text{t,gen}}$, for the five values of JSF with a linear fit for each JSF value and a constant fit to all points (black line), serving as a quality estimator. The biases are found to be up to 0.5 GeV around the generator mass and up to 7% around the input JSF value. The biases show a dependency on the JSF, but are nearly independent of the generator mass. All calibration point are fitted by the 2-dimensional function

$$\begin{aligned} f(m_{\text{t,extr}}, \text{JSF}_{\text{extr}}) = p_0 + p_1 \times (m_{\text{t,extr}} - 172.5) + p_2 \times (\text{JSF}_{\text{extr}} - 1) \\ + p_3 \times (m_{\text{t,extr}} - 172.5) \times (\text{JSF}_{\text{extr}} - 1) \, , \end{aligned}$$

with calibration parameters p_i. The remaining biases of the calibrated top quark mass $m_{\text{t,cal}}$ and calibrated jet scale factor JSF_{cal} of the pseudo-experiments, are depicted in the right part of figure 7.12 and are basically zero.

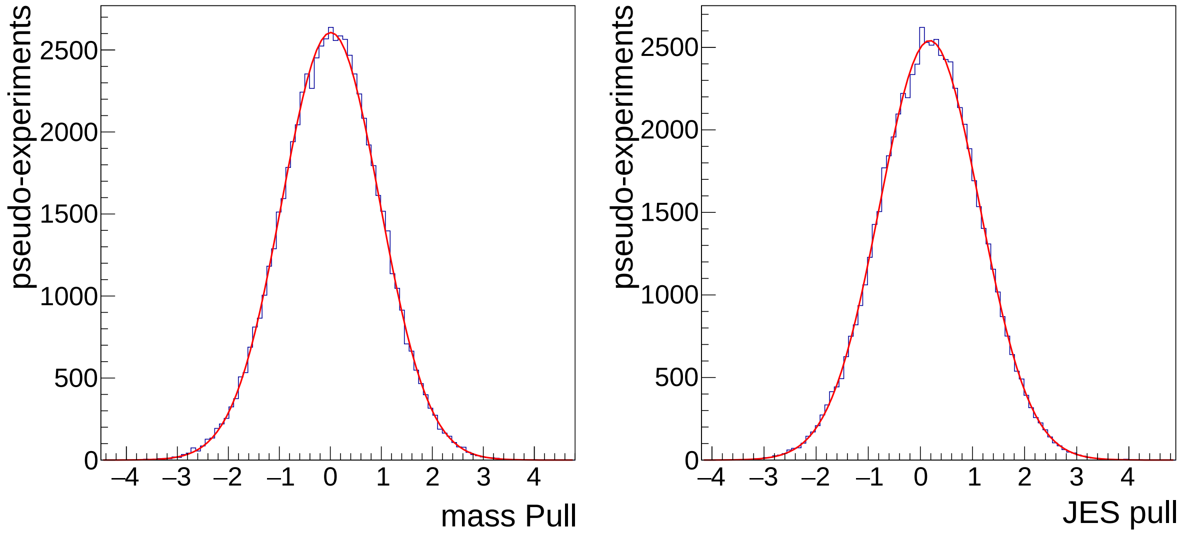

Figure 7.11: The pull distributions for the mass (left) and JSF (right) of the pseudo experiments for $m_{t,\mathrm{gen}} = 172.5\,\mathrm{GeV}$ and JSF=1 and their Gaussian fits.

The pull distribution is defined as

$$\text{pull} = \frac{x_{\text{calc}} - x_{\text{gen}}}{\sigma\left(x_{\text{calc}}\right)} ,$$

where x can in this context be m_{t} or JSF in one pseudo-experiment and $\sigma\left(x_{\text{calc}}\right)$ is the corresponding statistical uncertainty. The mass and JSF pull distribution for $m_{t,\mathrm{gen}} = 172.5\,\mathrm{GeV}$ and JSF=1 and their Gaussian fits are shown in figure 7.11. The pull distributions for each point are fit with Gaussian distributions, their width are displayed in figure 7.13. The pull width is expected to be unity. A larger/smaller width indicates that the statistical uncertainty reported by the extraction method is smaller/larger than the true statistical uncertainty. In average a pull widths of 0.99% is found but with different values ranging from 0.96% to 1.01% for the different JSF points. That means that for most samples and in average the statistical uncertainties are overestimated, while for JSF=0.96 it is slightly underestimate. As we will see later this will be no problem, because the analysis in this thesis will clearly be limited by systematic uncertainties and not by statistical.

No pull corrections were incorporated into the likelihood.

No further corrections are needed.

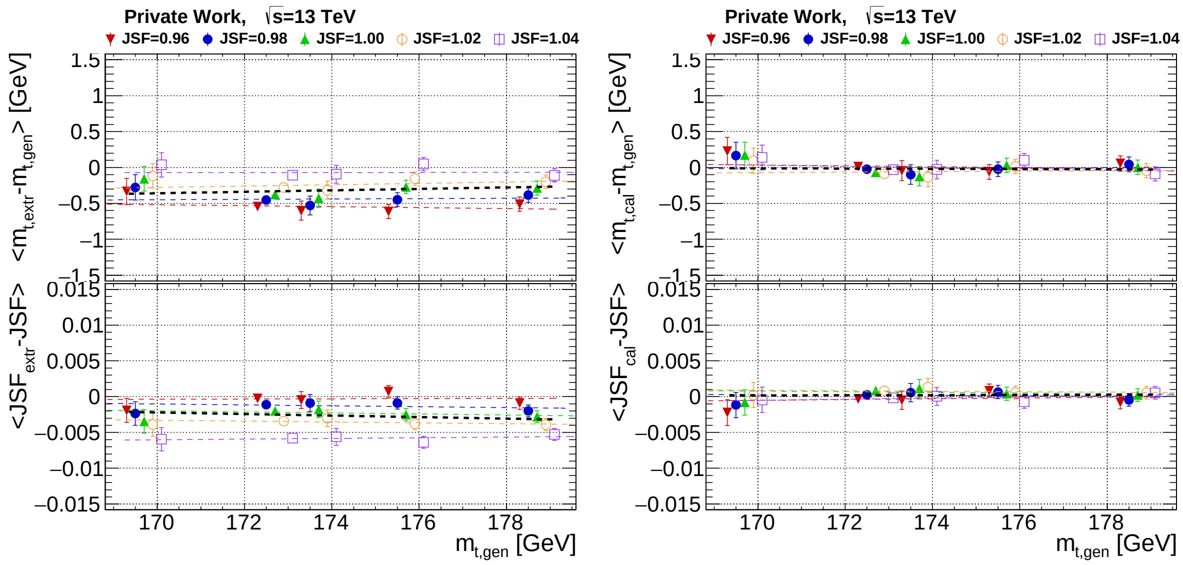

Figure 7.12: Mean difference between the extracted $m_{\mathrm{t,extr}}$ and each generated $m_{\mathrm{t,gen}}$ and between $\mathrm{JSF_{extr}}$ and $\mathrm{JSF_{gen}}$ for the muon channel before the calibration (left) and after the calibration (right), as a function of different generated $m_{\mathrm{t,gen}}$ and five values of JSF. The colored dashed lines correspond to straight line fits, which are used to correct the final likelihoods. The black solid line corresponds to the assumption of a constant calibration for all mass and JSF points in each channel.

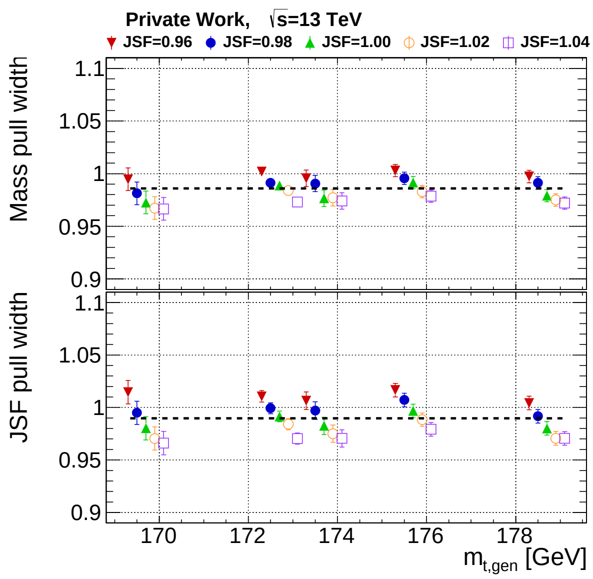

Figure 7.13: Width of the pull distribution for the calibrated measurement of m_{t} and JSF as a function of different generated $m_{\mathrm{t},gen}$ and five values of JSF for the muon channel. The black solid lines correspond to fits of constants to all calibration points, assuming no dependence on m_{t} or JSF.

8 Systematic Uncertainties

The top quark and its mass are well known and its observation in the $\sqrt{s} = 13\,\text{TeV}$ LHC is run expected. Interesting is the exact value of its mass. Therefore the certainty with which we can point on one value is most important. While the statistical uncertainty follows directly from the number of available top quark pairs in the measured data and the the mass resolution, the systematic uncertainties stem from shortcomings in, i.e., method, simulation, and applied corrections. These shortcomings and their impact on the measurement in this thesis will be described in this chapter.
Typically, the parameters that cause the uncertainty are changed by ± 1 standard deviation and the largest of the two observed shifts on m_{t} and JSF are taken as systematic uncertainty. Variations on the energy of the signal lepton or the jets are forwarded to the MET and the MET is recalculated. If the statistic uncertainty on a shift, due to a small variation sample, is larger than the shift itself, it is taken as uncertainty instead.

In table 8.1 the contributions from different sources to the systematic uncertainty are listed. The signs of the shifts are negative if a variation to a higher value led to a lower extracted top quark mass in the simulation. This would lead to a higher measured top quark mass in data. Shifts in brackets are not summed into the total uncertainty and are stated simply as overview over different uncertainty categories.

The dedicated samples that are used to evaluate some of the uncertainties are listed in table 6.1. They are fitted on the templates that were derived out of the `Powheg-Pythia 8` Monte Carlo simulation.

Table 8.1: List of systematic uncertainties for the fit to the muon+jets data set.

	2D approach		1D approach	Hybrid
	δm_t^{2D}	δJSF	δm_t^{1D}	δm_t^{hyb}
Experimental uncertainties				
Method calibration	0.07	<0.001	0.06	0.07
Jet energy corrections (quad. sum)	(–0.23)	(0.012)	(0.78)	(0.30)
– JEC: InterCalibration	<0.01	(0.001)	0.06	0.03
– JEC: MPFInSitu	0.01	(0.003)	0.23	0.12
– JEC: Uncorrelated non-pileup	<0.01	(0.009)	0.61	0.26
– JEC: Uncorrelated pileup	–0.23	(0.008)	0.42	0.11
Muon energy scale	0.03	<0.001	0.02	0.03
MET	<0.01	<0.001	<0.01	<0.01
Jet energy resolution	–0.12	0.002	0.04	–0.04
b tagging	0.07	<0.001	0.03	0.05
Pileup	–0.05	0.001	0.02	–0.02
Non-$t\bar{t}$ background	–0.24	0.001	–0.13	–0.19
Modeling of hadronization				
JEC: Flavor (linear sum)	(–0.46)	(0.001)	(–0.36)	(–0.41)
– light quarks (uds)	0.10	–0.001	–0.02	0.04
– charm	0.02	<0.001	–0.01	0.01
– bottom	–0.32	<0.001	–0.31	–0.32
– gluon	–0.27	0.003	–0.02	–0.15
b-jet modeling (quad. sum)	(–0.18)	(–0.001)	(–0.18)	(–0.18)
– b fragmentation	–0.02	–0.001	–0.08	–0.05
– Semi-leptonic B hadron decays	–0.18	<0.001	–0.16	–0.16
Modeling of perturbative QCD				
PDF	-0.03	<0.001	-0.02	-0.03
Ren. and fact. scale	<0.01	<0.001	–0.02	–0.01
Q^2 scale	0.27	0.002	0.19	0.23
ME generator	0.66	0.003	0.87	0.76
Top quark transverse momentum	0.03	–0.002	–0.16	–0.06
Modeling of soft QCD				
Underlying event	0.75	–0.014	–0.41	0.17
Color reconnection modeling	–0.27	0.001	–0.16	–0.22
Total systematic	**1.24**	**0.015**	**1.34**	**1.02**
with soft QCD modeling and ME generator Run 1 uncert. [23]	(0.69)	(0.005)	(0.93)	(0.63)
Statistical (expected)	0.45	0.004	0.28	0.33
Total (expected)	**1.32**	**0.015**	**1.37**	**1.07**

8.1 Experimental Uncertainties

The uncertainties due to the experimental setup, the pp-collision, the detector, and the high level trigger are following:

Fit calibration: The quadratic sum of statistical uncertainty and residual biases after the calibration is taken as systematic uncertainty of the method.

p_T- and η-dependent JEC: The p_T- and η-dependence of the jet energy correction (JEC) uncertainties is taken into account, by scaling the energies of all jets up and down. This is done according to their individual data/MC uncertainties [70]. These uncertainties are splitted into 23 individual sources that can be merged to TOPLHCWG correlation groups. This is documented at
`https://twiki.cern.ch/twiki/bin/viewauth/CMS/JECUncertaintySources`.
These uncertainties are flavor independent. Some of the JEC uncertainties, "Intercalibration" and "MPFInSitu", stem from modeling uncertainties in the residual corrections and are therefore correlated between different experiments. The "Uncorrelated" group is independent of models and other experiments and is split into two parts. One part is related to the pileup JEC uncertainties and the other to statistical uncertainties on the residual corrections and further detector effects. The JSF is measured for the specific flavor and p_T spectrum of the selected data samples. The shift in JSF of the flavor independent JEC uncertainties is given for information only and does not go into the total systematic uncertainty.

Lepton energy scale: The energy of the signal muon in simulated events is shifted up and down by one standard deviation. The values of the deviation are taken from reference [81].

Missing transverse momentum: The missing transverse momentum is scaled up and down by 10% [82].

Jet energy resolution: The jet energy resolution (JER) in the simulation was calibrated to match the resolution measured in data in reference. [70]. The calibration is done η dependent and results in smaller resolutions, varying from 9% up to 56%, of the simulation. The jet energy resolution in the simulation is varied by ± 1 standard deviations with respect to the degraded resolution.

b tagging: The events are weighted to account for the p_T dependent uncertainty of the b-tag efficiencies and mis-identification rates of the CSVv2M tagger [53]. The uncertainty is estimated with weight variations, reported and studied in AN-16-036, that correspond to ± 1 standard variation. [1]

Pileup: The pileup distributions for a $\pm 5\%$ variation of the minimum bias event cross-section, shown in figure 6.1, were used for the calculation of the simulation pileup weight to match the pileup observed in data. The effect on the extracted top quark mass is taken as systematic uncertainty.

Non-$t\bar{t}$ background: The main uncertainty on the non-$t\bar{t}$ background is the uncertainty on the theory cross-section prediction, resulting in a uncertainty of the normalization. Therefore the normalization of the background samples is varied by $\pm 4\%$ for the W+jets samples, $\pm 10\%$ for the Z+jets samples, $\pm 7\%$ for the di-boson samples, and $\pm 100\%$ for the QCD-multijet samples. The cross-section uncertainties were rounded up and should therefore result in a slight overestimation of the uncertainty. At the same time the modeling uncertainties in the simulation of these samples were not incorporated which should, because of the small background fraction of 4%, not have a reasonable effect .

8.2 Modelling Uncertainties

The uncertainty in the modeling, approximating, and simulating of the processes in a $t\bar{t}$ decay are categorized in three parts. The modeling of the hadronization of the jets after the $t\bar{t}$ decay, QCD effects in the pertubative regime, and the modeling of soft QCD, where pertubation theory does not apply.

8.2.1 Modeling of hadronization

Flavor-dependent JEC: The Lund string fragmentation that is implemented in the `PYTHIA 8` generator was compared to the cluster fragmentation in `Herwig++`. The relative difference

[1] The implementation of the b-tagging weights were given through personal correspondence by Nataliia Kovalchuk (`nataliia.kovalchuk@desy.de`).

in jet energy response between this two generators was determined for each jet flavor by the references [83, 84] and taken as systematic uncertainties. The uncertainties are evaluated for each flavor separately and added linearly.

b fragmentation: A retuning of the Bowler-Lund fragmentation function for B hadrons to agree with the x_B data measured by the ALEPH [85] and DELPHI [86] collaborations were done. The difference of "soft" and "hard" retuning is taken as uncertainty. The parameters of the retuning were evaluated by reference [23].

Semi-leptonic B hadron decays: The semi-leptonic branching ratio of B hadrons corresponds directly to the abundance of undetected neutrinos inside of b jets. The neutrinos lower the response with respect to the original bottom quark. The BR $(B \to \ell \nu X)$ is varied by -0.45% and $+0.77\%$ to give an envelope of the measurements from B^0/B^+ decays and their uncertainties. The envelope were evaluated by reference [23]. [2]

8.2.2 Modeling of hard scattering process

Parton distribution functions: The simulated events are generated using the NNPDF30 [87] PDF extrapolation with $\alpha_s = 0.118$. To estimate the uncertainty due to choice of PDF extrapolation, the events are weighted to match events generated with CT10 [88] and MMHT2014 [39]. In addition α_s is scaled to 0.117 and 0.119 for the NNPDF30 extrapolation. The quadratic sum of these three uncertainties is stated in table 8.1.

Renormalization and factorization scales: Effects of a change of the renormalization and factorization scales on the result were tested. Therefore, the simulated events were weighted to match the shapes of events generated with nominal renormalization and factorization scales, that were scaled simultaneously and independent from each other by the factors of 0.5 and 2. This uncertainty is combined linear with the uncertainty out of the Q^2 scale variation.

Q^2 scale: The Q^2 used in the parton shower was scaled up by 4 and down by 0.25 in dedicated simulation samples. In these samples a not expected difference of the jet response of the

[2] The implementation of the b fragmentation weights and weights that were used to evaluate the uncertainties due to semi-leptonic B hadron decays were given through personal correspondence by Nataliia Kovalchuk (`nataliia.kovalchuk@desy.de`).

Table 8.2: The shifts observed for different ME-generator setups compared to Powheg. All samples were showered with Pythia 8 and tuned with tune CUEP8M1 except the particle level comparison at $\sqrt{s} = 8\,\text{TeV}$ that were showered with preliminary Pythia 8. The amc@NLO(FXFX) samples were done with and without additional matrix element corrections (ME corr.) in Pythia. All mass shifts are given in GeV. The ME generator uncertainty of the $\sqrt{s} = 8\,\text{TeV}$ lepton+jets top quark mass measurement is stated in the last line. It is Powheg-Pythia6 Z2* compared to MadGraph-Pythia6 Z2*.

ME generator	δm_t^{2D}	δJSF	δm_t^{1D}
madgraphMLM	0.66	0.003	0.87
amc@NLO, no ME corr.	–1.84	0.001	–1.74
amc@NLOFXFX, no ME corr.	–1.52	0.005	–1.12
amc@NLO $f_{\text{perm.}}$ adjusted, no ME corr.	–1.31	–0.003	–1.57
comparison on kinematic fit level:			
amc@NLO $t\bar{t}$-correct			–1.18
comparison on particle level as given in reference [23]:			
madgraphMLM, 8 TeV	<0.01	0.001	0.19
amc@NLO, ME corr., 8 TeV	0.20	–0.001	0.11
amc@NLO, no ME corr., 8 TeV	–0.68	<0.001	–0.65
amc@NLOFXFX, ME corr., 8 TeV	0.02	–0.001	0.15
amc@NLOFXFX, no ME corr., 8 TeV	–0.72	0.003	–0.38
Run 1 ME generator uncertainty [23]	0.11	0.001	0.16

light quarks to the jet response of the default sample was observed. Therefore the jet response $\frac{p_t^{\text{reco}}}{p_t^{\text{gen}}}(p_t^{\text{gen}})$ of the light quarks in the variated samples were scaled to match the default sample. This shift stated in table 8.1 is the shift of the corrected sample.

ME generator The influence of the matrix element generator is estimated by using a sample with the madgraphMLM [89] matrix element generator instead of the Powheg generator, that is used as default. This comparison may have its short-comings due to the fact, that the matrix element in Powheg is calculated up to next-to-leading order (NLO), but in madgraphMLM in leading order.

In addition the shifts of amc@NLO [90] and amc@NLOFXFX [91] generators instead of the Powheg generator are evaluated. To exclude effects from jet multiplicity the shift was checked also for events with exactly four jets with $p_T > 30\,\text{GeV}$. This leads to the same result. The invariant mass of the top quark after the kinematic fit, the W-boson before the kinematic fit and the p_T of the four leading jets for samples with $m_{\text{t,gen}} = 172.5\,\text{GeV}$ are compared to data in figure 8.1. The p_T distributions differ and tend to a higher p_T than the data. This was not observed for events simulated with the Powheg generator

(compare to figure 6.12 and 6.10). The event yield with the amc@NLO or amc@NLOFXFX generator is lower than with Powheg and does not match the event yield in collision data well. If the template fits are adjusted for the permutation fraction from the kinematic fit of the amc@NLO sample, instead of the Powheg sample, the shift decreases approximately 530 MeV for the 2D and 130 MeV for the 1D approach. A shift in the same order of magnitude is observable if only the correct permutated events out of the kinematic fit are considered.
While the shifts are clearly larger than in the 8 TeV analysis, a large shift in the same direction is observed in the generator studies in reference [23].
The observed shifts are summarized in table 8.2. The shift compared to madgraphMLM was taken as final uncertainty on m_t.

Top p_T: The top p_T spectrum is affected by NNLO effects [63]. Therefore the top quark p_T in simulation is varied to match the distribution measured by CMS [84, 92–94].

8.2.3 Modeling of non-pertubative QCD

Underlying event: Non-pertubative QCD effects are taken into account by tuning Pythia to measurements of the underlying event [95]. The uncertainties are estimated by comparing a simulated sample that has decreased underlying event activity (mpiOFF, see reference [96]) relative the default sample.

Color reconnection modeling: There are some ambiguities in the modeling of color reconnection effects [97]. The uncertainties are estimated by comparing a simulated sample where the color reconnection was turned off to the default simulation sample.

Both of these non-perturbative QCD samples were not tuned correctly. Therefore the uncertainty due to the modeling of non-perturbative QCD is higher than expected. To get a better comparison to other analysis until the recalculated samples are available, the total systematic uncertainties with the non-perturbative QCD and ME-generator uncertainties of the Run 1 analysis in the same channel, out of reference [23], is also given in table 8.1.

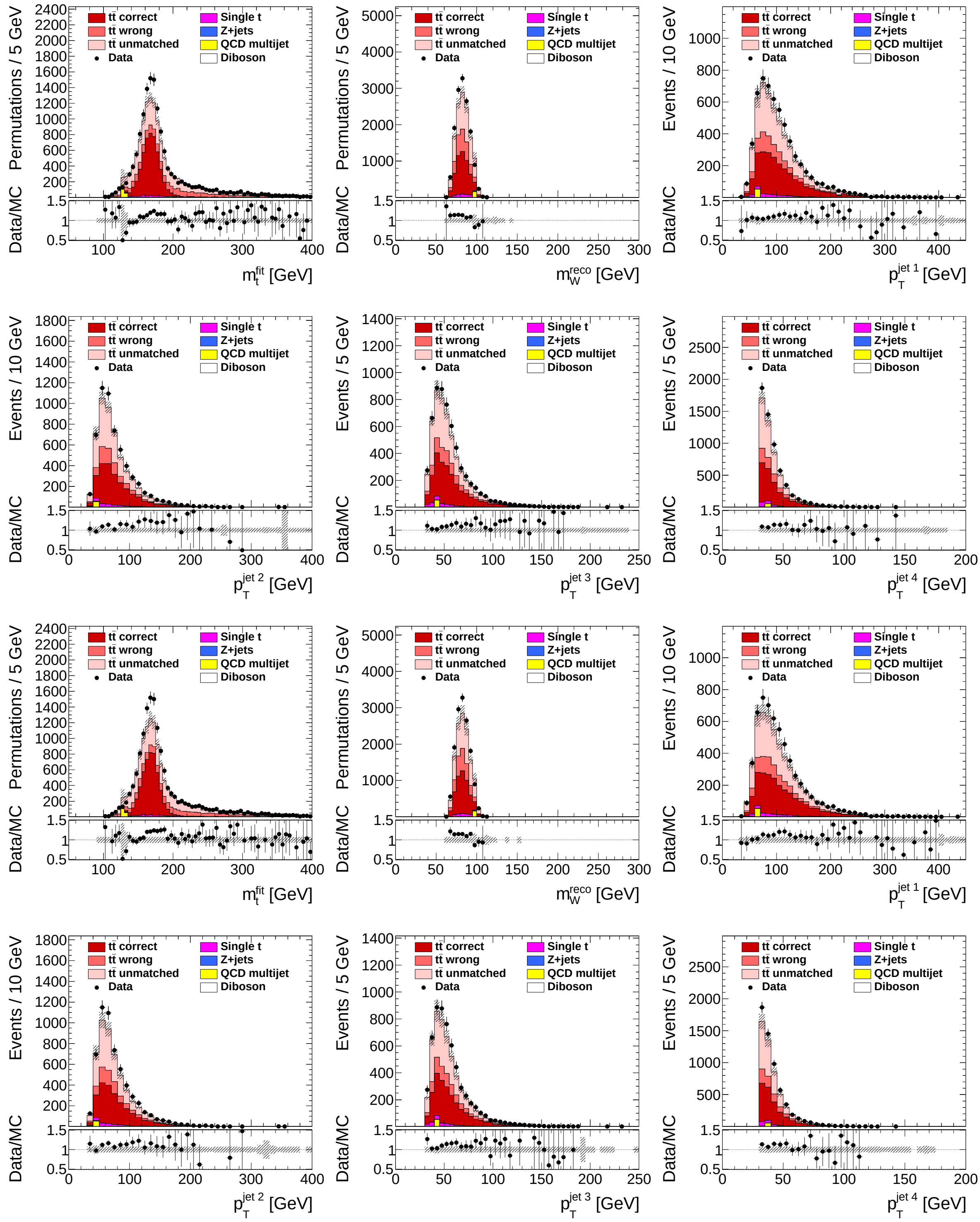

Figure 8.1: The invariant mass of the top quark after the kinematic fit (upper left),the W-boson before the kinematic fit (lower right), and the p_T of the leading four jets with simulated signal events using the `amc@NLOFXFX` generator (upper rows) or the `amc@NLO` generator (lower rows). The grey band is the cross-section and MC-statistics uncertainty.

8.3 Discussion of the uncertainties

Although only 2.2 fb^{-1} of data and only the muon final state are used in this thesis, the uncertainty of the result will not be limited by statistics, but by systematic uncertainties. The 2D and 1D approach have comparable uncertainties. If for the problematic soft QCD, Q^2-scale, and ME-generator uncertainty samples the Run 1 uncertainties would be taken, the 2D approach has a clearly better uncertainty of 0.69 GeV compared to 0.93 GeV. If the new samples are used, the advantage of the 2D method vanishes, and the uncertainties out of both approaches are approximately equal.
The dominant, not sample dependent, contributions to the uncertainties are the uncertainties on the jet energy correction (JEC). The flavor dependent part of this uncertainty is dominated by the bottom quark and gluon contribution. A part of it cancels against the variation of the light quark and charm jet energy. The not-flavor-dependent part of the JEC is dominated by the uncorrelated group. This group can not be improved by information of other experiments, but must be improved by jet energy studies of the CMS experiment in the same data sample.
The 2D approach systematic uncertainties are of comparable magnitude as for results in former analysis, but the 1D approach uncertainties are worse, mainly due to uncorrelated JEC.
The systematic uncertainty on the JSF is mainly driven by the underlying event Monte Carlo sample. Without this sample the uncertainty would be 0.005 instead of 0.015. Therefore it would be better than in former analysis and near its statistical limitation.
For the hybrid approach some of the uncertainties of the 2D and 1D approach cancel each other out, as intended. The highest cancellation is observed for the underlying event sample, were a uncertainty of 0.75 GeV for the 2D approach and 0.41 GeV for the 1D approach cancel to just 0.17 GeV. The biggest uncertainty comes from the comparison of different matrix element generators and is larger than all other uncertainties combined. The comparison of a NLO with a LO generator is not ideal and a better evaluation of this uncertainty is needed for future analysis. If this uncertainty is not taken into account, the biggest uncertainty in the hybrid approach stems again from JEC uncertainties, where only minor parts cancel out. The total hybrid uncertainty, including the expected statistical, the soft QCD, and ME-generator uncertainties, is with 1.07 GeV about 20% smaller than the uncertainty of the 2D approach.

9 Results of the measurement

The 2D approach on the 5 798 selected $t\bar{t} \rightarrow \mu + \text{jets}$ events, containing 14 327 permutations, results in a top quark mass and jet energy scale factor of

$$\begin{aligned} m_t^{2D} &= 172.50 \pm 0.45\ (\text{stat+JSF}) \pm 1.24\ (\text{syst})\ \text{GeV}\ , \\ \text{JSF} &= 0.996 \pm 0.004\ (\text{stat}) \pm 0.015\ (\text{syst})\ . \end{aligned}$$

The total uncertainty on the top quark mass in the 2D approach is 1.32 GeV. The JSF has a larger uncertainty than in previous measurements, as was discussed in section 8.3. Even with just the statistical uncertainties the JSF is compatible with unity and with former $\sqrt{s} = 8\,\text{TeV}$ analyses.
The likelihood plane of the 2D fit of the data is shown in the left side of figure 9.1. On the right side, the expected statistical uncertainty of the 2D top quark measurement is compared to the uncertainty in data. They agree well with each other. Because the JSF is measured simultaneously, its statistical uncertainty is included in this distribution.

Constraining the JSF to unity leads to the result of the 1D approach of

$$m_t^{1D} = 172.17 \pm 0.28\ (\text{stat}) \pm 1.34\ (\text{syst})\ \text{GeV}\ ,$$

where δ_{JSF} is included in the systematic uncertainty. This is, within the statistical uncertainty, compatible with the 2D result.

The combination of this two approaches is basically the combination of the top quark mass determination with in-situ JSF measurement with the γ/Z+jet jet energy correction out of reference [83]. It results in a top quark mass of

$$m_t^{\text{hyb}} = 172.34 \pm 0.37\ (\text{stat+JSF}) \pm 1.02\ (\text{syst})\ \text{GeV}\ .$$

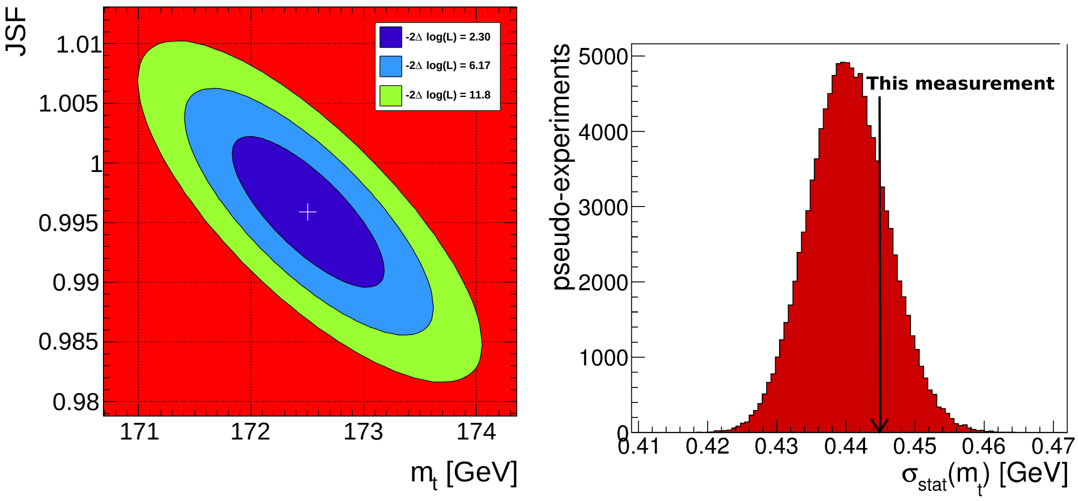

Figure 9.1: The 2D likelihood ($-2\Delta\log(\mathscr{L})$), with the ellipses corresponding to the statistical uncertainties on m_{t} and JSF of one, two, and three standard deviations in the plane (left). The statistical uncertainty distribution obtained from pseudo-experiments compared to the uncertainty of the fit in data for the 2D approach (right).

The total uncertainty is 1.07 GeV. This is a precision of 0.62%.
With the ME-generator uncertainty, taken from the Run 1 analysis in the same channel, the total uncertainty would be 0.77 GeV. The 2D likelihood of the hybrid approach with its statistical uncertainties is displayed in the left part of figure 9.2.

9.1 Translation to other mass schemes

The measured Monte Carlo mass $m_{\mathrm{t}}^{\mathrm{MC}}$ can be translated to mass schemes, that are theoretically better motivated. Following reference [24] (which is only valid for $\mathrm{e}^+\mathrm{e}^-$-collisions, for details see section 2.2.2), the measured mass $m_{\mathrm{t}}^{\mathrm{MC}} = m_{\mathrm{t}}^{\mathrm{hyb}} = 172.34 \pm 1.07\,\mathrm{GeV}$ is translated into a running short-distance mass of $m_{\mathrm{t}}^{\mathrm{MSR}}(R = 1\,\mathrm{GeV}) = 172.16 \pm 1.07 \pm 0.19\,\mathrm{GeV}$, introducing an additional theoretical uncertainty ($\pm 0.19\,\mathrm{GeV}$), that is small compared to the total uncertainty of this measurement.
Following the same reference, the pole mass of the top quark out of the hybrid measurement is found to be $m_{\mathrm{t}}^{\mathrm{pole}} = 171.77 \pm 1.07 \pm 0.28\,\mathrm{GeV}$. Again the uncertainty is still dominated by the experiment and not by theoretical uncertainties from the translation.
However, these calibration is only derived for $\mathrm{e}^+\mathrm{e}^-$ using 2-Jettiness and needs to be rederived

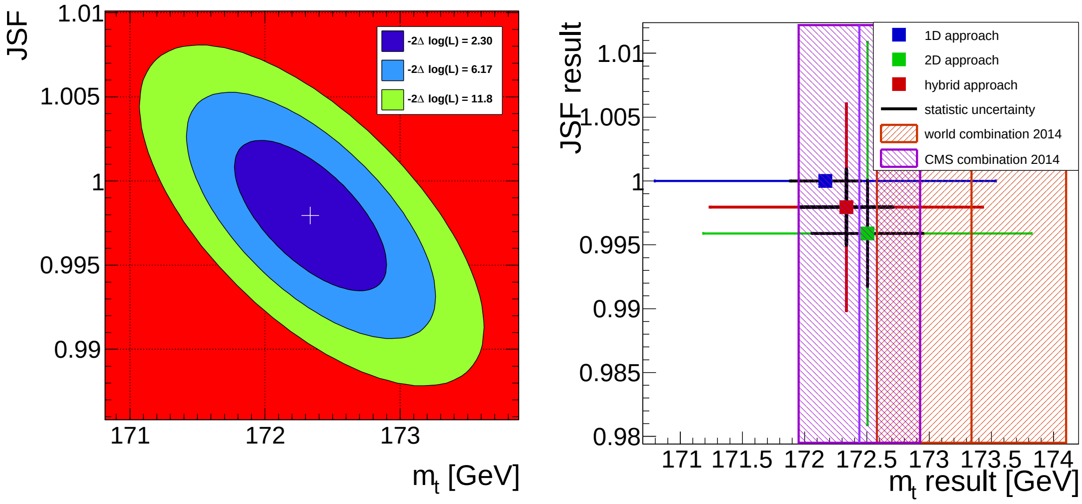

Figure 9.2: The hybrid likelihood ($-2\Delta\log(\mathscr{L})$) (left). The results of this thesis and the world combination of the top quark mass (right).

for pp final states and validated for other observables.

9.2 Comparison to other measurements

9.2.1 World combination

The combination of the top quark mass results of different analyses from LHC and Tevatron experiments in March 2014 provided a top quark mass of $m_t = 173.34 \pm 0.27 \pm 0.71\,\mathrm{GeV}$ [22]. Combination of CMS analysis results in different channels, and the combination of different Tevatron analysis, can be found in figure 9.3. The biggest difference between single analysis results can be seen between the CMS ($m_t = 172.35 \pm 0.51\,\mathrm{GeV}$) and DØ ($m_t = 174.98 \pm 0.76\,\mathrm{GeV}$) analysis in the lepton+jets channel.
In the right part of figure 9.2 the results of all approaches in this thesis are displayed in comparison to the world combination and the CMS Run 1 combination. They are compatible with each other within the uncertainty but compared to the world combination with a trend to lower masses in this analysis. This analysis and the CMS combination agree extremely well.

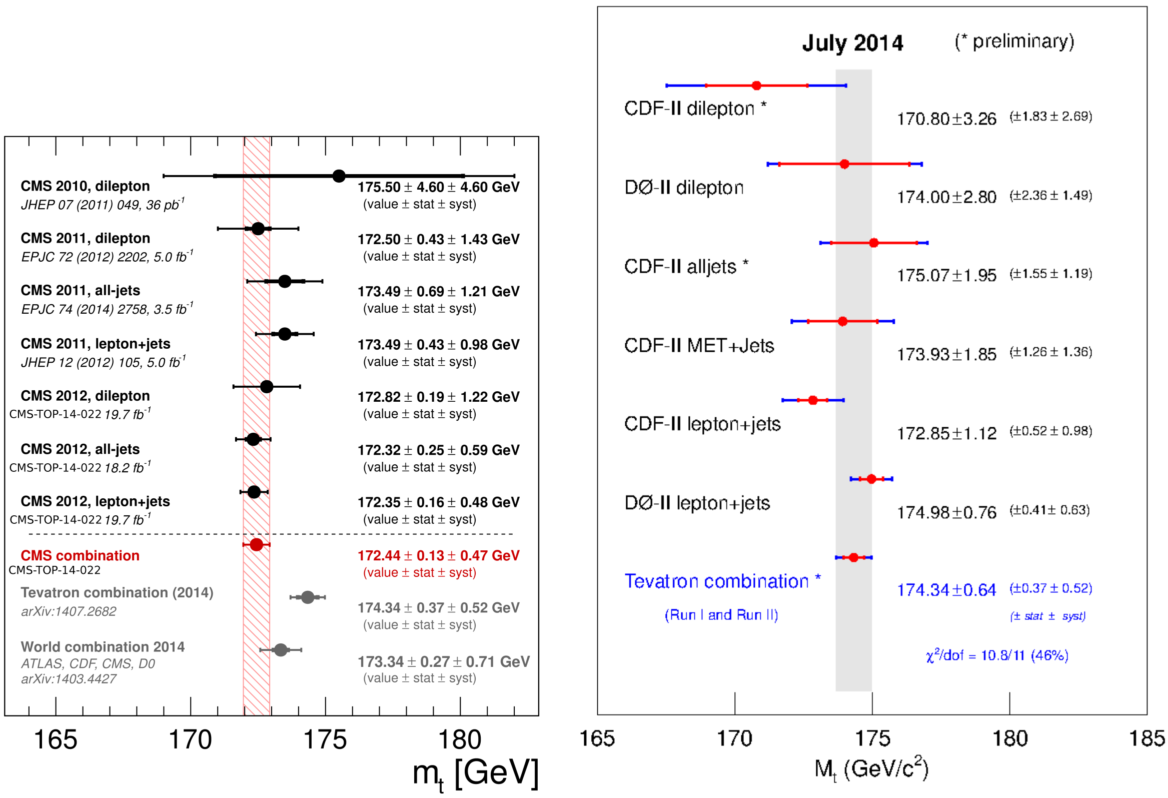

Figure 9.3: The top quark mass combination of the CMS experiment, state of September 2015 [75], (left) and of the Tevatron experiments, state of July 2014 [98] (right).

9.2.2 Comparison to the $\sqrt{s} = 8$ TeV lepton+jets analysis at CMS

The latest published CMS analysis of the top quark mass in the lepton+jets channel was done with $\sqrt{s} = 8$ TeV data from the LHC Run 1. It was published in 2015 and used the same method that was used in this thesis [23]. Therefore not only the final result, but even some of the steps can be compared.
The main differences between the 8 TeV and this analysis are the center-of-mass energy, at which the data was taken, the luminosity, and the Monte Carlo generators on which the simulated events are based.

Setup For the 8 TeV analysis, 19.7 fb^{-1} integrated luminosity were used, in this analysis 2.2 fb^{-1} were available. The simulated events in the 8 TeV analysis were done using the `MadGraph` generator and `Pythia 6` as showering algorithm. This thesis uses `Powheg-Pythia 8` and only the muon final state is included while in the 8 TeV analysis electron were considered also. The simulated events of the 8 TeV and this analysis are independent from one another.

Selection Further, the selected phase-space is slightly different. The jet reconstruction uses a cone with $R < 0.5$ in the Run 1 analysis but $R < 0.4$ in this run. Selected muons are now required to have a transverse momentum of at least 25 GeV compared to the 33 GeV cut in the 8 TeV analysis.
The b-Tag algorithm that was used in this thesis is a newer version of the `CSV` algorithm used in the previous analysis.
The $t\bar{t}$ signal fraction in simulation in the Run 1 analysis is 56.6% in the preselection, 92.6% in the baseline selection, and 96.3% in the final selection compared to 61.4% in the preselection, 90.9% in the baseline selection, and 95.9% in the final selection in this analysis. The fractions for the 8 TeV analysis are for combined electron and muon data. The higher fraction in the preselection step in this analysis is due to the removal of events with overlapping signal lepton jets in the pre- and not the baseline selection.
The fraction of events with correct permutation, again for muons and electrons, are 12.8% in the baseline, 41.7% in the final, and 43.8% in the effective (with p_{gof} weight) selection. In this thesis this fraction are a little bit higher with 14.8% in the baseline, 43.8% in the final, and 46.8% in the effective selection. The higher fractions in this analysis can be explained by the better b-tagging and the better reconstruction of muons compared to electrons.

Method The same template method with pseudo-experiments for calibration were used in both analysis. In the Run 1 analysis, nine different $m_{t,\mathrm{gen}}$ values were used for template creation and method calibration. In this thesis five different $m_{t,\mathrm{gen}}$ values are used. Both analysis use five different JSF points for the creation of the templates, but the 8 TeV analysis only uses three for the method calibration while this thesis uses all five. In the calibration, the background samples were included in the Run 1 analysis, in this theses they were not. Muon and electron template fits and calibration were done separately.
Due to the higher available statistic, the method calibration for $\sqrt{s} = 8\,\mathrm{TeV}$ were more exact, resulting in an uncertainty on the top quark mass of 0.04 GeV, compared to 0.07 GeV in this thesis.
In this thesis about 3% different pull width were observed for different JSF values. This was not visible in the Run 1 analysis. This is not understood yet. Both analysis predicted the statistical uncertainty correct by using the mean pull width.

Uncertainties The statistical uncertainties in this thesis are approximately twice as high as as the uncertainties in the 8 TeV analysis. This is a very good result, if it is taken into account, that only one of the two available final states in the lepton+jets channel is used, and only about a tenth of luminosity is available.
The systematic uncertainty on the final result was 0.49 GeV in the Run 1 analysis and is 1.02 GeV in this analysis. If the problematic samples, see section 8.2.3, and the alternative ME generators are not taken into account and the corresponding uncertainties are taken from Run 1, this improves to 0.63 GeV. In this case the main sources of the bigger uncertainty are the uncorrelated JEC, and the non-$t\bar{t}$ background. The difference between the ME-generators that stem from comparing the LO matrix element of `madgraphMLM` to the NLO matrix element in `Powheg` should be included in the uncertainty of the Run 1 analysis.

Result The result of the 8 TeV analysis is very close to the top quark mass that is observed in this thesis. The results of the 2D, 1D and hybrid approach are compared in figure 9.4 and, within their uncertainties, they are all compatible with each other.

9.3 Outlook

At the time this thesis is submitted, an analysis of the top quark mass with $\sqrt{s} = 13\,\text{TeV}$ events from 2016 is ongoing. It it using a newer version of the `CMSSW` program and other simulated samples. It will include more data and the electron final state. Therefore it is expected to decrease the statistical uncertainty drastically.
The problematic tuning in the simulated samples for the soft QCD and Q^2 uncertainty will be corrected. The difference between the samples with different ME-generators can hopefully be addressed if studied more closely. Therefore an improvement of the systematic uncertainty is expected.
To improve the precision of the measured top quark mass even further, it will be essential to understand the jet energy and be able to decrease the uncertainty on its correction. If that can be achieved, the uncertainty on the measurement of the top quark mass will come even closer to a regime, were it is not limited by the analysis of the experiment, but by its relation to theory parameters.

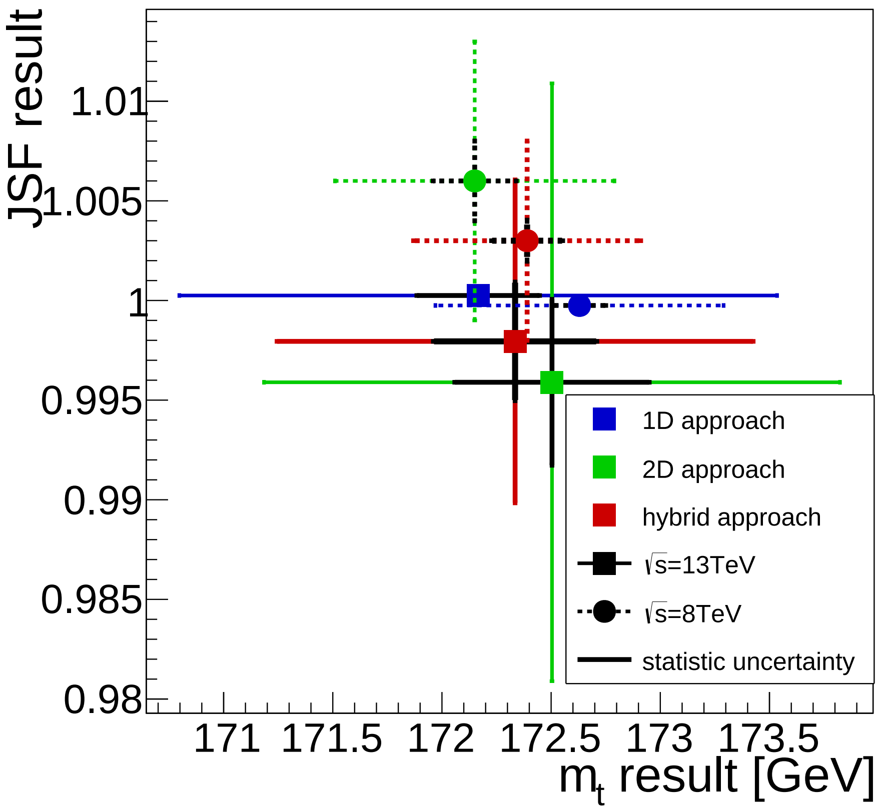

Figure 9.4: The results of this thesis compared to the results of the $\sqrt{s} = 8\,\text{TeV}$ analysis.

10 Summary

In this thesis, the mass of the top quark was measured in data of pp-collisions at a center-of-mass energy of $\sqrt{s} = 13\,\text{TeV}$ at the LHC collected in 2015. The integrated luminosity $2.2\,\text{fb}^{-1}$ data as well as the theoretical description (`Powheg-Pythia` Monte-Carlo event simulations) are new in comparison to previous top quark mass measurements.
The final state of choice was the muon+jets final state of the $\text{t}\bar{\text{t}}$ decay. In this channel, a very clean $\text{t}\bar{\text{t}}$-signal sample could be achieved by utilizing a sophisticated event reconstruction, various kinematic selections, and a kinematic fit of the decay products to a $\text{t}\bar{\text{t}}$ hypotheses.
The hybrid method, that was used for the measurement, lead to a cancellation of some systematic uncertainties. It combines the in-situ measurement of the top quark mass and the jet scale factor from the kinematic fit with the reconstructed W-boson mass, with the jet scale factor from γ/Z+jet jet energy corrections. The measurements were done by building templates for the different generator masses and jet energy scale factors in simulated samples.
The main source of uncertainty on the result are the jet energy uncertainties. An analysis of this uncertainties shows, that improvements on the jet energy calibration, additional simulation samples for systematic uncertainties, and a larger event sample will improve this initial result.
The result is $m_t^{\text{hyb}} = 172.34 \pm 0.37$ (stat+JSF) $\pm\, 1.02$ (syst) GeV. This confirms the result of the top quark mass analysis at CMS with $\sqrt{s} = 8\,\text{TeV}$ and is within uncertainty compatible with the world average of the top quark mass. The discrepancy of the CMS result with the results from the DØ experiment in the lepton+jets channel could not be solved.
Even with the high precision of 0.6% in the result of this analysis, it does not compete with the 0.3% precision of the most precise single measurement, using the same method but final calibrations and a lower luminosity at $\sqrt{s} = 8\,\text{TeV}$ by CMS, of the top quark mass. Nonetheless it indicates that an analysis of the 2016 LHC data could achieve this and showed, that the advantages of the used approach are still valid for the new collision data, theoretical descriptions, and software versions.
This measurement is also presented in CMS Physics Analysis Summary AN-16-278.

Bibliography

[1] B. P. Abbott and et al. Observation of gravitational waves from a binary black hole merger. *Phys. Rev. Lett.*, 116:061102, Feb 2016.

[2] K. A. Olive et al. Review of Particle Physics. *Chin. Phys.*, C38:090001, 2014.

[3] CERN. `http://www.stfc.ac.uk/research/particle-physics-and-particle-astrophysics/peter-higgs-a-truly-british-scientist/why-is-the-higgs-discovery-so-significant/`.

[4] G. L. Fogli, E. Lisi, A. Marrone, D. Montanino, A. Palazzo, and A. M. Rotunno. Global analysis of neutrino masses, mixings and phases: entering the era of leptonic CP violation searches. *Phys. Rev.*, D86:013012, 2012.

[5] J. Beringer et al. 2012 review of particle physics - gauge and higgs bosons. *PR*, 2012.

[6] S. Schael et al. Precision electroweak measurements on the Z resonance. *Phys. Rept.*, 427:257–454, 2006.

[7] F. Abe et al. Observation of top quark production in $\bar{p}p$ collisions. *Phys.Rev.Lett.*, 74:2626–2631, 1995.

[8] The CDF Collaboration. Observation of top quark production in pp-collisions. *Phys. Rev. Lett.*, 1995.

[9] Scott S. Snyder. Measurement of the top quark mass at d0. Technical report, 1995.

[10] A. Quadt. Top quark physics at hadron colliders. *The European Physical Journal C - Particles and Fields*, 48(3):835–1000, 2006. 10.1140/epjc/s2006-02631-6.

[11] CMS Collaboration. http://www.desy.de/e409/e116959/e119238/media/2967/top-plot.jpg.

[12] A measurement of the inclusive tbart production cross section in proton-proton collisions at sqrts=13 TeV using events with one isolated charged lepton and at least one jet. Technical Report CMS-PAS-TOP-16-006, CERN, Geneva, 2016.

[13] S. Heinemeyer, W. Hollik, G. Weiglein, and L. Zeune. Implications of lhc search results on the w boson mass prediction in the mssm. *Journal of High Energy Physics*, 2013(12):1–31, 2013.

[14] S. Alekhin, A. Djouadi, and S. Moch. The top quark and higgs boson masses and the stability of the electroweak vacuum. *Physics Letters B*, 716(1):214 – 219, 2012.

[15] M. Baak, J. Cúth, J. Haller, A. Hoecker, R. Kogler, K. Mönig, M. Schott, and J. Stelzer. The global electroweak fit at NNLO and prospects for the LHC and ILC. *Eur. Phys. J.*, C74:3046, 2014.

[16] Stephen P. Martin. A Supersymmetry primer. 1997. [Adv. Ser. Direct. High Energy Phys.18,1(1998)].

[17] The CMS Collaboration. Measurement of the top-antitop mass difference in pp collisions at sqrt s=8 TeV. 2016.

[18] M. Beneke and Vladimir M. Braun. Heavy quark effective theory beyond perturbation theory: Renormalons, the pole mass and the residual mass term. *Nucl. Phys.*, B426:301–343, 1994.

[19] Sven-Olaf Moch. Precision determination of the top-quark mass. volume 2014, page 054, Trieste, Apr 2014. 12th DESY Workshop on Elementary Particle Physics: Loops and Legs in Quantum Field Theory, Weimar (Germany), 27 Apr 2014 - 2 May 2014, SISSA.

[20] Peter Marquard, Alexander V. Smirnov, Vladimir A. Smirnov, and Matthias Steinhauser. Four-loop relation between the $\overline{\text{MS}}$ and on-shell quark mass. In *Proceedings, 12th International Symposium on Radiative Corrections (Radcor 2015) and LoopFest XIV (Radiative*

Corrections for the LHC and Future Colliders): Los Angeles, CA, USA, June 15-19, 2015, 2016.

[21] Fred Jegerlehner, Mikhail Yu. Kalmykov, and Bernd A. Kniehl. Self-consistence of the Standard Model via the renormalization group analysis. *J. Phys. Conf. Ser.*, 608(1):012074, 2015.

[22] First combination of Tevatron and LHC measurements of the top-quark mass. 2014.

[23] Markus Seidel. *Precise measurement of the top-quark mass at the CMS experiment using the ideogram method.* PhD thesis, U. Hamburg, Dept. Phys., Hamburg, 2015.

[24] Mathias Butenschoen, Bahman Dehnadi, Andre H. Hoang, Vicent Mateu, Moritz Preisser, and Iain W. Stewart. Top Quark Mass Calibration for Monte Carlo Event Generators. 2016.

[25] Iain W. Stewart, Frank J. Tackmann, and Wouter J. Waalewijn. N-Jettiness: An Inclusive Event Shape to Veto Jets. *Phys. Rev. Lett.*, 105:092002, 2010.

[26] CERN collaboration. *Fifty years of the CERN Proton Synchrotron: Volume 1*. CERN, Geneva, 2011.

[27] CMS. Cms luminosity 2015. `https://twiki.cern.ch/twiki/bin/view/CMSPublic/LumiPublicResults#2015_Proton_Proton_13_TeV_Collis`.

[28] Lefèvre. Lhc preaccelerator chain. `www.stfc.ac.uk/research/particle-physics-and-particle-astrophysics/large-hadron-collider/cern-accelerator-complex/`.

[29] CERN. Lhc basics. `https://press.cern/backgrounders/lhc-season-2-facts-figures`.

[30] Oliver Sim Brüning, Paul Collier, P Lebrun, Stephen Myers, Ranko Ostojic, John Poole, and Paul Proudlock. *LHC Design Report*. CERN, Geneva, 2004.

[31] CMS Collaboration. *CMS Physics: Technical Design Report Volume 1: Detector Perfor-*

mance and Software. Technical Design Report CMS. CERN, Geneva, 2006. There is an error on cover due to a technical problem for some items.

[32] CMS Collaboration. *CMS Physics: Technical Design Report Volume 2: Physics Performance*. Technical Design Report CMS. CERN, Geneva, 2006.

[33] CMS Collaboration. Cms 3-d imgage for inclusion in presasntations - white bachground. `https://cms-docdb.cern.ch/cgi-bin/DocDB/ShowDocument?docid=2716`.

[34] CMS Collaboration. Cms slice. `http://commons.wikimedia.org/wiki/File:CMS_Slice.gif`.

[35] Torbjorn Sjostrand, Stephen Mrenna, and Peter Z. Skands. Pythia 6.4 physics and manual. *JHEP*, 0605:026, 2006.

[36] Torbjorn Sjostrand, Stephen Mrenna, and Peter Z. Skands. A Brief Introduction to PYTHIA 8.1. *Comput. Phys. Commun.*, 178:852–867, 2008.

[37] Andy Buckley, Jonathan Butterworth, Stefan Gieseke, David Grellscheid, Stefan Hoche, et al. General-purpose event generators for lhc physics. *Phys.Rept.*, 504:145–233, 2011.

[38] A. M. Cooper-Sarkar. PDF Fits at HERA. *PoS*, EPS-HEP2011:320, 2011.

[39] A. D. Martin, W. J. Stirling, R. S. Thorne, and G. Watt. Parton distributions for the LHC. *Eur. Phys. J.*, C63:189–285, 2009.

[40] Simone Alioli, Paolo Nason, Carlo Oleari, and Emanuele Re. A general framework for implementing NLO calculations in shower Monte Carlo programs: the POWHEG BOX. *JHEP*, 06:043, 2010.

[41] T. D. Lee and M. Nauenberg. Degenerate Systems and Mass Singularities. *Physical Review*, 133:B1549–B1562, March 1964.

[42] John C. Collins. Sudakov form-factors. *Adv. Ser. Direct. High Energy Phys.*, 5:573–614, 1989.

[43] Bo Andersson, G. Gustafson, G. Ingelman, and T. Sjostrand. Parton Fragmentation and String Dynamics. *Phys. Rept.*, 97:31–145, 1983.

[44] Comparison of Monte Carlo generator predictions for bottom and charm hadrons in the decays of top quarks and the fragmentation of high pT jets. Technical Report ATL-PHYS-PUB-2014-008, CERN, Geneva, Jun 2014.

[45] Serguei Chatrchyan et al. Description and performance of track and primary-vertex reconstruction with the CMS tracker. *JINST*, 9(10):P10009, 2014.

[46] Particle-Flow Event Reconstruction in CMS and Performance for Jets, Taus, and MET. Technical Report CMS-PAS-PFT-09-001, CERN, 2009. Geneva, Apr 2009.

[47] Serguei Chatrchyan et al. Performance of CMS muon reconstruction in pp collision events at $\sqrt{s} = 7$ TeV. *JINST*, 7:P10002, 2012.

[48] Performance of electron reconstruction and selection with the cms detector in proton-proton collisions at$\sqrt{}$ s = 8 tev. *Journal of Instrumentation*, 10(06):P06005, 2015.

[49] Matteo Cacciari, Gavin P. Salam, and Gregory Soyez. The Anti-k(t) jet clustering algorithm. *JHEP*, 0804:063, 2008.

[50] Maryam Zeinali. Measurement of the Jet Energy Scale in the CMS experiment with the First LHC Proton Collisions.

[51] S. Eno, D. Ferencek, I. Iashvili, and M. Zielinski. Offset Energy Correction for Cone Jets. `http://cms.cern.ch/iCMS/jsp/db_notes/noteInfo.jsp?cmsnoteid=CMS%20AN-2009/035`, May 2009.

[52] Jet energy scale and resolution performances with 13TeV data. Jun 2016.

[53] Performance of b tagging at sqrt(s)=8 TeV in multijet, ttbar and boosted topology events. Technical Report CMS-PAS-BTV-13-001, CERN, Geneva, 2013.

[54] Performance of b-Tagging Algorithms in Proton Collisions at 13 TeV using the 2016 Data. Jul 2016.

[55] Identification of b quark jets at the CMS Experiment in the LHC Run 2. Technical Report CMS-PAS-BTV-15-001, CERN, Geneva, 2016.

[56] Vardan Khachatryan et al. Performance of the CMS missing transverse momentum reconstruction in pp data at $\sqrt{s} = 8$ TeV. *JINST*, 10(02):P02006, 2015.

[57] Torbjörn Sjöstrand, Stefan Ask, Jesper R. Christiansen, Richard Corke, Nishita Desai, Philip Ilten, Stephen Mrenna, Stefan Prestel, Christine O. Rasmussen, and Peter Z. Skands. An Introduction to PYTHIA 8.2. *Comput. Phys. Commun.*, 191:159–177, 2015.

[58] Underlying Event Tunes and Double Parton Scattering. Technical Report CMS-PAS-GEN-14-001, CERN, Geneva, 2014.

[59] P. Skands, S. Carrazza, and J. Rojo. Tuning pythia 8.1: the monash 2013 tune. *The European Physical Journal C*, 74(8):1–39, 2014.

[60] S. Agostinelli et al. GEANT4 – a simulation toolkit. *Nucl. Instrum. Meth. A*, 506:250, 2003.

[61] Michał Czakon, Paul Fiedler, and Alexander Mitov. Total Top-Quark Pair-Production Cross Section at Hadron Colliders Through $O(\alpha\frac{4}{S})$. *Phys. Rev. Lett.*, 110:252004, 2013.

[62] Nikolaos Kidonakis. Next-to-next-to-leading soft-gluon corrections for the top quark cross section and transverse momentum distribution. *Phys. Rev. D*, 82:114030, 2010.

[63] Nikolaos Kidonakis. Differential and total cross sections for top pair and single top production. In *Proceedings, 20th International Workshop on Deep-Inelastic Scattering and Related Subjects (DIS 2012)*, pages 831–834, 2012. [,831(2012)].

[64] Kirill Melnikov and Frank Petriello. Electroweak gauge boson production at hadron colliders through $O(\alpha_s^2)$. *Phys. Rev. D*, 74:114017, 2006.

[65] John M. Campbell and R. K. Ellis. MCFM for the Tevatron and the LHC. *Nucl. Phys. Proc. Suppl.*, 205-206:10, 2010.

[66] John M. Campbell, J. W. Huston, and W. J. Stirling. Hard Interactions of Quarks and Gluons: A Primer for LHC Physics. *Rept. Prog. Phys.*, 70:89, 2007.

[67] Michal Czakon and Alexander Mitov. Top++: A Program for the Calculation of the Top-Pair Cross-Section at Hadron Colliders. *Comput. Phys. Commun.*, 185:2930, 2014.

[68] J. Ohnemus. Order $\alpha^{-}s$ calculations of hadronic $W^{\pm}\gamma$ and $Z\gamma$ production. *Phys. Rev.*, D47:940–955, 1993.

[69] U. Baur, Tao Han, and J. Ohnemus. QCD corrections to hadronic $W\gamma$ production with nonstandard $WW\gamma$ couplings. *Phys. Rev.*, D48:5140–5161, 1993.

[70] Serguei Chatrchyan et al. Determination of jet energy calibration and transverse momentum resolution in CMS. *JINST*, 6:P11002, 2011.

[71] Gaël L. Perrin and Luca Perrozzi. Update on Muon reRECO Scale-Factors, 2016.

[72] B. et al. Abbott. Direct measurement of the top quark mass at d0. *Phys.Rev.*, D58:052001, 1998.

[73] CMS Collaboration. Measurement of the top-quark mass in $t\bar{t}$ events with lepton+jets final states in pp collisions at $\sqrt{s}$=7 tev. *J. High Energy Phys.*, 12(arXiv:1209.2319. CMS-TOP-11-015. CERN-PH-EP-2012-250):105. 33 p, Sep 2012.

[74] Markus Seidel. *Precise measurement of the top-quark mass at the CMS experiment using the ideogram method*. PhD thesis, U. Hamburg, Dept. Phys., Hamburg, 2015.

[75] Vardan Khachatryan et al. Measurement of the top quark mass using proton-proton data at $\sqrt{(s)}$ = 7 and 8 TeV. *Phys. Rev.*, D93(7):072004, 2016.

[76] J. Beringer et al. (Particle Data Group). Review of Particle Physics. *Phys. Rev. D*, 86:010001, 2012.

[77] J. Abdallah et al. Measurement of the mass and width of the W boson in $e^{+}e^{-}$ collisions at $\sqrt{s}$ = 161 – 209 GeV. *Eur. Phys. J. C*, 55:1, 2008.

[78] V. M. Abazov et al. Measurement of the top quark mass in the lepton + jets channel using the ideogram method. *Phys. Rev. D*, 75:092001, 2007.

[79] T. Aaltonen et al. Measurement of the top-quark mass in all-hadronic decays in $p\bar{p}$ collisions at CDF II. *Phys. Rev. Lett.*, 98:142001, 2007.

[80] Serguei Chatrchyan et al. Measurement of the top-quark mass in all-jets $t\bar{t}$ events in pp collisions at $\sqrt{s}$=7 TeV. *Eur.Phys.J.*, C74:2758, 2014.

[81] Serguei Chatrchyan et al. The performance of the CMS muon detector in proton-proton collisions at sqrt(s) = 7 TeV at the LHC. *JINST*, 8:P11002, 2013.

[82] Performance of Missing Transverse Momentum Reconstruction Algorithms in Proton-Proton Collisions at p s = 8 TeV with the CMS Detector. 2012.

[83] Henning Kirschenmann. Jet performance in CMS. Technical Report CMS-CR-2013-325, CERN, Geneva, Oct 2013.

[84] Measurement of the inclusive and differential tt production cross sections in lepton + jets final states at 13 TeV. Technical Report CMS-PAS-TOP-16-008, CERN, Geneva, 2016.

[85] A. Heister et al. Study of the fragmentation of b quarks into B mesons at the Z peak. *Phys. Lett. B*, 512:30–48, 2001.

[86] J. Abdallah et al. A study of the b-quark fragmentation function with the DELPHI detector at LEP I and an averaged distribution obtained at the Z Pole. *Eur. Phys. J. C*, 71:1557, 2011.

[87] Richard D. Ball et al. Parton distributions for the LHC Run II. *JHEP*, 04:040, 2015.

[88] Hung-Liang Lai, Marco Guzzi, Joey Huston, Zhao Li, Pavel M. Nadolsky, et al. New parton distributions for collider physics. *Phys. Rev. D*, 82:074024, 2010.

[89] Johan Alwall, Michel Herquet, Fabio Maltoni, Olivier Mattelaer, and Tim Stelzer. MadGraph 5 : Going Beyond. *JHEP*, 06:128, 2011.

[90] Valentin Hirschi, Rikkert Frederix, Stefano Frixione, Maria Vittoria Garzelli, Fabio Maltoni, and Roberto Pittau. Automation of one-loop QCD corrections. *JHEP*, 05:044, 2011.

[91] Rikkert Frederix and Stefano Frixione. Merging meets matching in MC@NLO. *JHEP*, 12:061, 2012.

[92] Serguei Chatrchyan et al. Measurement of differential top-quark pair production cross sections in pp colisions at $\sqrt{s} = 7$ TeV. *Eur. Phys. J. C*, 73:2339, 2013.

[93] Measurement of differential top-quark pair production cross sections in the lepton+jets channel in pp collisions at 8 TeV. Technical Report CMS-PAS-TOP-12-027, CERN, Geneva, 2013.

[94] Measurement of the differential ttbar cross section in the dilepton channel at 8 TeV. Technical Report CMS-PAS-TOP-12-028, CERN, Geneva, 2013.

[95] Serguei Chatrchyan et al. Measurement of the underlying event activity at the LHC with $\sqrt{s} = 7$ TeV and comparison with $\sqrt{s} = 0.9$ TeV. *JHEP*, 09:109, 2011.

[96] Peter Zeiler Skands. Tuning Monte Carlo generators: The Perugia tunes. *Phys. Rev. D*, 82:074018, 2010.

[97] Peter Z. Skands and Daniel Wicke. Non-perturbative QCD effects and the top mass at the Tevatron. *Eur. Phys. J. C*, 52:133, 2007.

[98] Tevatron Electroweak Working Group. Combination of CDF and D0 results on the mass of the top quark using up to 9.7 fb^{-1} at the Tevatron. 2014.

Erklärung

Hiermit bestätige ich, dass die vorliegende Arbeit von mir selbst verfasst wurde und ich keine anderen als die angegebenen Hilfsmittel - insbesondere keine im Quellenverzeichnis nicht benannten Internet-Quellen - benutzt habe und die Arbeit von mir nicht in einem anderen Prüfverfahren eingereicht wurde. Die eingereichte schriftliche Fassung entspricht der auf dem elektronischen Speichermedium. Ich bin damit einverstanden, dass diese Masterarbeit veröffentlicht wird.

Hamburg, October 11, 2016

Unterschrift